UNIVERSITY OF MARYLAND

Department of Physics
Space Physics Group

Measurements of H^+, He^{2+}, and He^+ in Corotating Interaction Regions at 1 AU

by

Kancham Chotoo

Dissertation submitted to the Faculty of the Graduate School
of The University of Maryland in partial fulfillment
of the requirements for the degree of
Doctor of Philosophy
1998

College Park, Maryland 20742

ABSTRACT

Title of Dissertation: MEASUREMENTS OF H^+, HE^{2+}, AND HE^+ IN COROTATING INTERACTION REGIONS AT 1 AU.

Kancham Chotoo, Doctor of Philosophy, 1998

Dissertation directed by: George Gloeckler, Professor
Department of Physics, University of Maryland

Nathan A. Schwadron, Assistant Research Scientist
Thomas H. Zurbuchen, Assistant Research Scientist
Department of AOSS, University of Michigan

Using the Supra-Thermal Ion Composition Spectrometer (STICS) from the SMS experiment on the WIND spacecraft, measurements of H^+, He^{2+}, and He^+ were made during two corotating interacting regions (CIRs) at 1 AU. The unique energy range of STICS (6 - 198 keV/e) allowed simultaneous observation of the pre- and post-accelerated ions. These observations gave important clues about the source population, injection, acceleration mechanism, and ion transport in CIRs.

The abundance of He^{2+} relative to H^+ in the velocity range 2.5 - 6.0 times the solar wind velocity, V_{SW}, (5 - 90 keV/amu) was between 0.11 - 0.18, which is more than double the solar wind values. However, the same ratio was observed in the suprathermal tail above 1.4 V_{SW} in the spacecraft frame or above ~0.4 V_{SW} in the solar wind frame. This suggests that the H^+ and He^{2+} ions are injected equally into the CIR acceleration process from the suprathermal tail of the solar wind.

At 1 AU the H^+ and He^{2+} ions are primarily from the solar wind, but the He^+ ions are interstellar pickup ions. The He^+/He^{2+} ratio at 1 AU was ~0.15 for the same velocity range as above. However, this ratio was greater than 1.0 at 4.5 AU as measured previously (Gloeckler et al., 1994). This shows that the relative contribution of the pickup He^+ ions to the seed population increases with radial distance away from the Sun.

By combining data from three separate sensors on WIND (SMS-MASS, SMS-STICS, and EPACT-STEP), the extended helium distribution was presented for solar wind ions (~1 keV/amu) through energetic particles up to ~1 MeV/amu. The distribution covered 14 orders of magnitude in phase space density. This is the first time such an extended helium distribution is being reported at any radial distance. Using the Fisk and Lee (1980) model to fit the data between ~10 - 1000 keV/amu, the energetic particles were found to originate from 1.0 - 1.2 AU and not from beyond 2 AU, as is conventially believed.

Anisotropy measurements were made using STICS for both the H^+ and He^{2+} ions in the solar wind frame, and the results were compared to those made by EPACT-STEP. For both time intervals, the anisotropy directions showed significant deviations away from the average magnetic field direction in agreement with the STEP observations of Dwyer et al. (1997).

MEASUREMENTS OF H^+, HE^{2+}, AND HE^+ IN COROTATING INTERACTION REGIONS AT 1 AU

by

Kancham Chotoo

Dissertation submitted to the Faculty of the Graduate School of the
University of Maryland, College Park in partial fulfillment
of the requirements for the degree of
Doctor of Philosophy
1998

Advisory Committee:

Professor George Gloeckler, Chair
Assistant Research Scientist Nathan A. Schwadron
Professor Douglas C. Hamilton
Professor Glenn M. Mason
Research Professor Michael A. Coplan

DEDICATION

To my parents, to my wife, and to my son

ACKNOWLEDGMENTS

I would like to thank my advisor, Dr. George Gloeckler (SMS Principal Investigator), who created the opportunity for me to work on STICS. I would especially like to thank my co-advisors, Nathan Schwadron and Thomas Zurbuchen, for the boost of encouragement and for the guidance that I needed to finish my dissertation. I would also like to thank Len Fisk for his vote of confidence in me. I would like to thank Toni Galvin for giving me the opportunity to do research in the Space Physics group. I would also like to thank her for her support and guidance during my first few years with the group, especially during the Ph.D. qualifying exam. An extra special "Thank you" goes out to Chris Cohen for her technical expertise in Space Physics and her moral support.

I would like to thank all the members of my dissertation committee for reviewing my work and evaluating this dissertation. I thank Keith Ogilvie, John Steinberg, and Al Lazarus for the SWE data, Adam Szabo and Ron Lepping for the MFI data, and Tycho von Rosenvinge and Glenn Mason for the EPACT data.

I would like to thank John Cain and Steve Christon for encouraging me to stick with the program. I really appreciated Joe Dwyer's help in understanding the Compton-Getting transformation, and providing me with STEP data. I would like to thank Jane Hessing for all her help and encouraging words over the years.

I appreciated the chance to work with the following people: Jeff Miller for his computer expertise; Doug Hamilton for evaluating my work over the years and giving me useful comments; Joe Mazur, Glenn Mason, and Mihir Desai for their insight on CIRs; Steve Christon for discussions on CIRs and kappa functions; Mike Collier for the MASS routines, and for his help with the kappa paper, my first published paper; my office-mate, George Ho, for his help with the MASS data and discussions on Space Phyiscs; Ed Tums for his help with the Pulser Calibrations and for his assistance in fixing the problem with STICS right after launch; Steve Brown and

Claude Smith at the GSFC accelerator facility; John Cain, Bob Cates and Wayne Shanks for their expertise during the calibration at GSFC; Bob Cates for the technical drawings and for his useful discussions in understanding the calibration results; Bob Lundgren (Project Engineer) for the experience I received in sending commands to the instrument during spacecraft integration and after launch; Peter Bedini for the calibration (GSE) software; Urs Schwab, Rob Sheldon and Roland Bodmer during the Bern calibration; Scott Lasley for his help during the GSFC and Bern calibrations, and during the Pulser testing at Maryland, and for his Mac expertise; Paul Wilson, and David Griff who gave me a first hand demonstration of the STICS entrance aperture and deflection system; John Paquette for the SMS software; Larry Bleau for being my computer guru; Pat Ipavich, Joann Simms, Cassie Jones, Aileen Desroisier, Sheryl James, Lily Paputski for their help in filling out paper work; Jen Williams for always being so bubbly and cheerful.

This research was funded by NASA through contract NAS5-30370.

TABLE OF CONTENTS

List of Tables viii

List of Figures x

Chapter 1: Introduction 1

1.1 Motivation 1

1.2 Corotating Interaction Regions (CIRs) 3

1.3 Previous Work 10

1.4 Thesis Overview 25

Chapter 2: Instrumentation 28

2.1 The WIND Mission 28

2.2 SMS 29

2.3 The Supra-Thermal Ion Composition Spectrometer 34

2.3.1 Principle of Operation 34

2.3.2 Angular Apertures 40

2.4 Telemetry 43

2.4.1 Housekeeping Data 43

2.4.2 Direct Sensor Rates 43

2.4.3 Science Rates 44

2.4.4 PHA Words 44

2.5 Summary 48

Chapter 3: Data Analysis 49

3.1 Data Extraction 49

3.2 Instrument Response Function 52

3.2.1 Duty Cycle and Deadtime Corrections 52

3.2.2 Basic Rate Normalization 54

3.2.3 Box Efficiency 54

3.2.4 Geometric Factor 57

3.2.5 TOF Telescope Efficiencies 58

3.2.6 Energy Passband ($\Delta E/Q$) 59

3.3 Binning the Data 61

3.4 Differential Flux and Distribution Function 61

3.5 Summary 64

Chapter 4: Composition and Spectra 65

4.1 Introduction 65

4.2 The Fisk and Lee Model 67

4.3 Other Instruments Used 69

4.4 Event Selection 70

4.5 Observations 81

4.5.1 April Event Spectra 88

4.5.2 May Event Spectra 92

4.6 Analysis 96

4.6.1 Comparison between model and observations 96

4.6.2 CIR 1 and 2 Source Distributions 97

4.6.3 Accelerated Ion Intensities 98

4.7 Discussion 102

4.8 Summary 106

Chapter 5: Anisotropy Measurements 108

5.1 Introduction 108

5.2 Example of Apparent Off-field Streaming 110

5.3 Compton-Getting Transformation 111

5.3.1 Analysis Check 115

5.4 CIR Anisotropies 118

5.5 Discussion 129

5.6 Summary 131

Chapter 6: Conclusions 132

Appendix A: Calibration Data Analysis 136

A.1 Calibration 136

A.2 Calibration Results 139

A.2.1 Rate Linearity Tests 139

A.2.2 Angular Response 140

A.2.3 Energy Passband ΔE/Q 145

A.2.4 Start and Stop TOF efficiencies 148

A.2.5 Geometric Factor 164

A.2.6 Sphere Efficiency 166

A.3 Pulser Calibrations 167

A.3.1 Energy Pulser Tests 167

A.3.2 Threshold Tests 176

A.3.3 Time Pulser Tests 178

A.4 Inflight Cross Calibration 181

A.4.1 STEP Comparison 181

A.4.2 MASS Comparison 183

A.4.3 Correction to Geometric Factor 184

A.5 Summary of Calibration Results 186

References 188

LIST OF TABLES

1.1 CIR abundances relative to oxygen 13

1.2 SEP, Photospheric, and slow solar wind abundances 14

2.1 Summary of the different instruments on WIND 33

2.2 Default DPU Matrix Rate definitions in M-M/Q space 46

2.3 Truth table for combined START and Range in PHA words 47

3.1 Accumulation deadtime correction factors 53

3.2 Box definition and efficiency for H^+, He^+, and H^{2+} 55

3.3 Geometric factors determined from calibrations 58

3.4 Energy-per-charge and passband for each voltage step 62

3.5 Instrument response function parameters 64

4.1 CIR boundaries for the two different events 76

4.2 H^+ core plasma parameters and magnetic field data during CIRs 84

4.3 He^{2+} core plasma parameters from kappa fits during CIR times 85

4.4 Spectral indices for H^+, He^{2+}, and He^+ during CIR times 93

4.5 Relative abundances H^{2+}/H^+ and He^+/He^{2+} during CIR times 93

5.1 Polar and azimuthal acceptance angles for each telescope 112

5.2 STICS H^+ and He^{2+} anisotropy results for CIR 1 and 2 119

A.1 E/Q resolution for all calibrated ions 147

A.2 Hydrogen TOF telescope smoothed efficiency values 158

A.3 Helium TOF telescope smoothed efficiency values 159

A.4 C, N, O and Ne TOF telescope smoothed efficiency values 160

A.5 Argon TOF telescope smoothed efficiency values 161

A.6 Krypton TOF telescope smoothed efficiency values 162

A.7 Iron TOF telescope smoothed efficiency values 163

A.8 Energy pulser results for SSD1 done November 1993 170

A.9 Energy pulser results for SSD2 done November 1993 171
A.10 Energy pulser results for SSD3 done November 1993 172
A.11 Energy pulser results for SSD1 done July 1992 173
A.12 Energy pulser results for SSD2 done July 1992 174
A.13 Energy pulser results for SSD3 done July 1992 175
A.14 Energy thresholds for the different solid state detectors 176
A.15 Telescope 1 time pulser results done November 1993 179
A.16 Telescope 2 time pulser results done November 1993 179
A.17 Telescope 3 time pulser results done November 1993 180
A.18 Time periods for STICS and STEP comparisons 182
A.19 Time periods for STICS and MASS comparisons 183
A.20 Shift Factor results from MASS and STEP 185
A.21 Revised geometric factors from STEP and MASS comparisons 185
A.22 Summary of calibration results 186

LIST OF FIGURES

1.1 Sketch of magnetic field lines from the Sun 4
1.2 Diagram of a corotating interaction region 6
1.3 Schematic of two CIRs showing plasma parameters at 1AU 7
1.4 Time profiles of energetic protons in CIRs at 2.8 and 4.7 AU 9
1.5 Anisotropy measurements from ISEE-3 EPAS 19
1.6 Sketch of tilted interaction regions 20
1.7 Distribution functions for H^+, He^{2+}, and He^+ at 4.5 AU 21
2.1 The WIND trajectory 31
2.2 The WIND spacecraft and its sensors 32
2.3 A block diagram of STICS electronics 35
2.4 A cross-sectional view of the STICS sensor 36
2.5 STICS look directions 39
2.6 Location of physical blockages on the carbon foil 41
2.7 A cross-sectional view of the entrance aperture 42
2.8 Raw PHA data plotted in M-M/Q space 45
3.1 M-M/Q plot showing new helium boxes 56
3.2 Smoothed H and He TOF efficiency 60
4.1 Spacecraft trajectory for first seven months in 1995 71
4.2 SWE H^+ solar wind speeds from 12/29/94-4/15/95 72
4.3 SWE H^+ solar wind speeds from 4/16/95-8/1/95 73
4.4 Coronal hole maps 74
4.5 SWE and MFI key parameter data for CIR 1 77
4.6 SWE and MFI key parameter data for CIR 2 78
4.7 EPACT key parameter data for CIR 1 79

4.8 EPACT key parameter data for CIR 2 80
4.9 STICS omni-directional ratios for CIR 1 82
4.10 STICS omni-directional ratios for CIR 2 83
4.11 Maxwellian and Kappa fits to solar wind He^{2+} 86
4.12 STICS H^+, He^{2+}, and He^+ spectra for CIR 1 90
4.13 Extended He^{2+} distribution from 1-1000 keV/amu for CIR 1 91
4.14 STICS H^+, He^{2+}, and He^+ spectra for CIR 2 94
4.15 Extended He^{2+} distribution from 1-1000 keV/amu for CIR 2 95
4.16 Model fit to STICS and STEP data for both CIRs 99
4.17 He^{2+}/H^+ ratio for core distribution and suprathermal tail 100
4.18 STICS H^+ and He^{2+} plotted together for both CIRs 101
4.19 Normalized flux of interstellar ions as a function of distance 105
5.1 Angular distribution of upstream ion event in solar wind frame H^+ 116
5.2 Angular distribution of upstream ion event in solar wind frame He^{2+} 117
5.3 STICS omni-directional fluxes for CIR 1 120
5.4 STICS omni-directional fluxes for CIR 2 121
5.5 H^+ anisotropy in solar wind frame for CIR 1 122
5.6 He^{2+} anisotropy in solar wind frame for CIR 1 123
5.7 H^+ anisotropy in solar wind frame for CIR 2 124
5.8 He^{2+} anisotropy in solar wind frame for CIR 2 125
5.9 STICS and STEP proton and helium anisotropies for CIR 1 126
5.10 STICS and STEP proton and helium anisotropies for CIR 2 127
5.16 STEP proton anisotropy at different energies for CIR 2 128
A.1 A cross-sectional view of STICS inside the Bern vacuum chamber 138
A.2 Rate linearity test using He^+ at 49.35 keV for telescope 2 140

A.3 Beta Scans done at energies 9.7-10.4 keV using H^+ at Bern 141
A.4 The entrance aperture of STICS shown in angular space 142
A.5 Alpha scan using He^+ with ß=0 143
A.6 Alpha scan using H^+ with energy wobbled 144
A.7 E/Q scan of DVS 15 using O^+ for telescope 2 at Bern 146
A.8 Hydrogen TOF telescope efficiencies 149
A.9 Helium TOF telescope efficiencies 150
A.10 Carbon TOF telescope efficiencies 151
A.11 Nitrogen TOF telescope efficiencies 152
A.12 Oxygen TOF telescope efficiencies 153
A.13 Neon TOF telescope efficiencies 154
A.14 Argon TOF telescope efficiencies 155
A.15 Krypton TOF telescope efficiencies 156
A.16 Smoothed efficiency curves for H, He, C, N, O, Ne, Ar, and Kr 157
A.17 Parallel beam geometric factor for telescope 2 165
A.18 Diagram of set-up for the energy pulser test 168
A.19 Linear relation between energy and energy channel number 169
A.20 Normalized SSD2 rate plotted against pulser energy 177
A.21 Set-up used for time pulser tests 178
A.22 STICS and STEP Helium spectra 182
A.23 STICS and MASS Helium spectra 184

CHAPTER 1: INTRODUCTION

1.1 Motivation

Since before the discovery of the solar wind, it has been known that ions can be accelerated to enormous energies in the cosmos. The most energetic ions, called cosmic rays, enter our tiny volume of the cosmos from beyond the heliosphere, and even beyond the galaxy. Our understanding of the processes which underly their acceleration is not yet fully understood. To a large extent the grasp we now have on the acceleration processes involved are derived from a close coupling between *in situ* observation and theory for ion acceleration in the heliosphere.

The study of ion acceleration in the heliosphere is ultimately tied to the so-called anomalous component of cosmic rays. The anomalous component is observed between ~1 and 30 MeV/nucleon for hydrogen, helium, carbon, oxygen, nitrogen and neon (Hovestadt et al., 1973; McDonald et al., 1974) and is dominantly formed from interstellar neutrals, which penetrate the heliosphere (Fisk et al., 1974) become ionized in the solar wind, and are ultimately accelerated at the termination shock of the solar wind (Jokipii, 1986). One useful feature of the anomalous component is that it gives human beings a way of studying of shock acceleration; namely we can observe the minor ions in the solar wind prior to their acceleration and subsequently observe them as energetic particles. Differences in composition between the pre- and post-accelerated populations and relative intensities of the populations are but a few examples of the observational diagnostics, which may be used to characterize and understand the acceleration process.

As often occurs in physics, the more a given physical phenomenon is probed, the more evident it becomes that the initial understanding of the phenomenon is either incomplete or simply wrong. This is certainly the case for the anomalous component. That step between initial ionization of the interstellar neutrals and the final acceleration to anomalous component energies is a comlpex problem. To what extent is pre-

acceleration in the heliosphere required? To what extent must cross-field diffusion at the termination shock be applied? To what extent does statistical acceleration as opposed to diffusive acceleration play a role? These are but a few of the questions in our current understanding of this important and apparently ubiquitous process in the cosmos.

The discovery that the anomalous component is formed from a seed population of interstellar pickup ions provides a dramatic confirmation of the prevalence of ion acceleration within plasmas and an important case of ion acceleration available for our continued study. However, from an observational perspective it has one important drawback: the acceleration occurs at the termination shock, which has not yet been directly observed (it's position is thought to be near 85 AU) and potentially involves many occurrences of pre-acceleration and direct acceleration. In other words, it is difficult to study the micro-physics behind the acceleration on these very large spatial scales with *in situ* spacecraft.

This brings us to consideration of shocks in the heliosphere which are more easily observed by spacecraft. The corotating interaction region (or CIR) is one common form of heliospheric shock and results from the interaction of fast and slow solar wind streams, occurring quite often at low latitudes near solar minimum. By studying ion acceleration in these regions, we gain a better and perhaps more complete understanding of the micro-physics involved in shock acceleration. It is also very likely that acceleration within CIRs is a necessary preconditioning of ions for subsequent acceleration at the termination shock.

This thesis is devoted to the continued study of ion acceleration within CIRs. The work is unique due to its exploitation of a unique instrument, STICS, on the WIND satellite. In the thesis we first develop the tools necessary to analyze data from STICS and subsequently apply the tools to the analysis of ion acceleration within CIRs near 1 AU. The conclusions we obtain from this analysis both confirm existing models and

provide new clues regarding the micro-physics behind ion acceleration within CIRs. Many of the observational results represent a first look at the acceleration in the unique energy range of STICS at 1 AU and motivate careful examination in the framework of an evolving theoretical understanding of CIRs.

In this chapter, we first give a description of a corotating interaction region (CIR), and how it is identified (Section 1.1). We also give a brief description of the conventional model of acceleration by the shocks bounding a CIR (Fisk and Lee, 1980). Section 1.2 gives an overview of the major studies done on CIRs over the past thirty years with emphasis on observations. The general layout of the dissertation is given in Section 1.3.

1.2 Corotating Interaction Region (CIR)

In general, hot ionized gases emanate from the Sun in alternating streams of high and low speed solar wind at low heliographic latitudes, especially during the declining phase of the 11-year solar activity cycle. The high-speed streams (>600 km/s or 1.3 million miles/hour) typically originate from coronal holes (Krieger et al., 1973; Nolte et al., 1976). Coronal holes appear as dark regions on X-ray images and are areas on the Sun where the magnetic field is open so that the plasma can stream away from the sun easily. The density and temperature in coronal holes are lower than those in surrounding areas. On the other hand, regions of closed magnetic field lines, such as coronal helmet streamers, are able to hold dense plasmas (Figure 1.1). Coronal helmet streamers are believed to be a source of the slow (~350 km/s) solar wind (Feldman et al., 1981).

The solar wind travels radially outwards from the Sun and carries the "frozen-in" magnetic field. As the Sun rotates, the flows with different speeds are radially aligned at low latitudes causing the high-speed solar wind to eventually overtake and collide with the lower-speed wind. The collision between the fast and slow wind results in

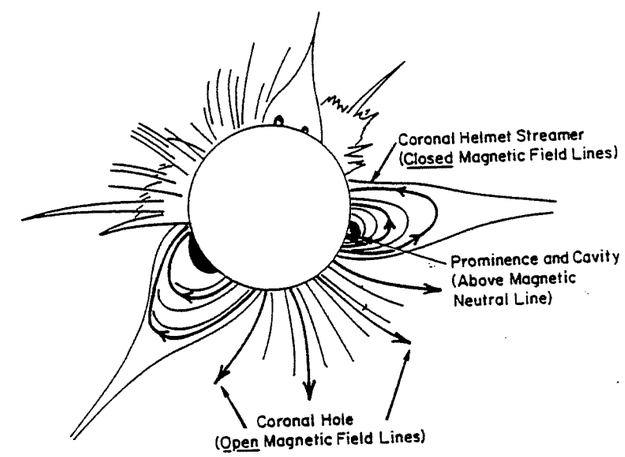

Figure 1.1. Sketch of magnetic field lines on the Sun (Hundhausen, 1995).

the compression of plasma in the interaction region. The streams and field patterns corotate with the Sun and is commonly known as the corotating interaction region, or CIR (Gosling et al., 1995).

Figure 1.2 is a schematic drawing of a CIR as viewed from the frame corotating with the Sun (Fisk and Lee, 1980). In this frame, the CIR is stationary in time because the fast wind steadily streams out of the Sun lasting several solar rotations (1 solar rotation = 27 days, as viewed from the Earth). Due to the excess pressure in the CIR, the CIR expands into the ambient solar wind causing the leading and trailing edges to be bounded by forward and reverse propagating waves, respectively. The forward wave propagates into the solar wind ahead accelerating the slow wind, while the reverse wave propagates back into the high-speed stream decelerating the fast wind. If the CIR expansion speed becomes greater than the magnetosonic sound speed (the speed at which information is transmitted through the solar wind plasma), then the bounding waves may steepen into forward and reverse shocks. The shocks typically form beyond ~2.5 AU (Hundhausen and Gosling, 1976) since the magnetosonic sound speed decreases with distance away from the Sun.

The typical solar wind plasma signatures for a CIR at 1 AU are shown in Figure 1.3 (Richardson et al., 1993; Belcher and Davis, 1971). Here again the frame of reference is corotating with the Sun. In this frame the structure in the upper half of the figure is stationary, while the spacecraft moves clockwise through the CIRs along the dashed arc. Region S represents the unperturbed slow wind; region S' indicates the compressed, accelerated slow wind; region F' represents the compressed, decelerated fast wind, and region F is the fast wind followed by another slow stream. Regions S' and F' together form the corotating interaction region. The spacecraft's observations are plotted against time in the bottom half of Figure 1.3 for the different regions. The start of the CIR (S-S' boundary) coincides with an increase in magnetic field intensity, plasma temperature and density. The end of the CIR (F'-F boundary) corresponds to a

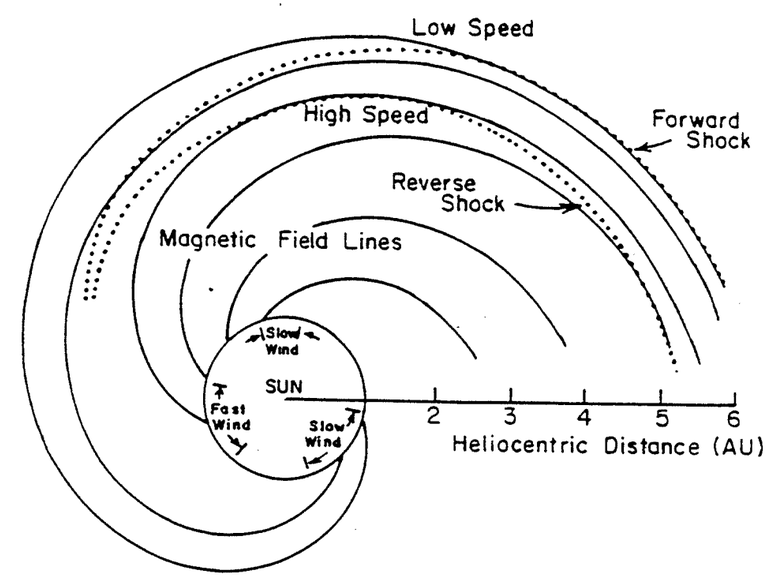

Figure 1.2. Diagram of a corotating interaction region as viewed from the frame corotating with the Sun (Fisk and Lee, 1980).

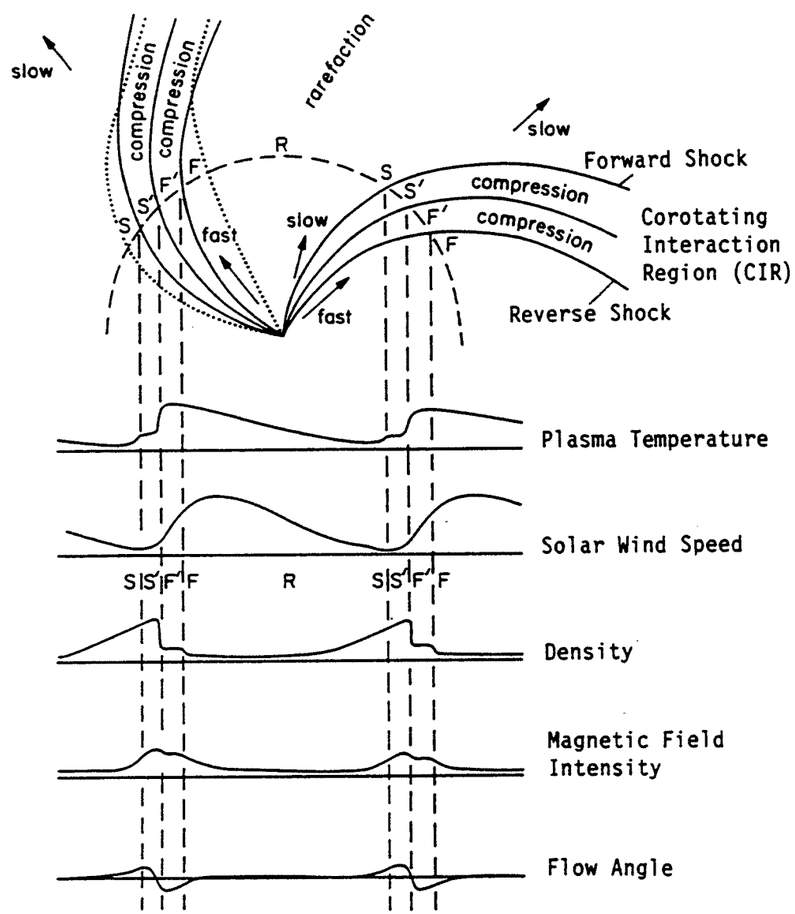

Figure 1.3. Schematic of two high-speed streams corotating with the Sun showing typical changes in the solar wind parameters at 1 AU: S, ambient slow solar wind; S', compressed, accelerated slow solar wind; F', compressed, decelerated, fast solar wind; F, unperturbed fast solar wind. The S' and F' regions, separated by the stream interface, form the corotating interaction region (CIR) which is bounded by forward and reverse shocks in the outer heliosphere. Magnetic field lines (dotted lines) in the S and F regions at 1 AU link to the forward and reverse shocks, respectively (Richardson et al., 1993; Belcher and Davis, 1971).

drop in these three quantities. As the CIR passes, the solar wind speed increases during the event. The solar wind flow is predominantly from the east of the Sun in region S' and from the west of the Sun in region F'. The "stream interface" (S'-F' boundary) separates the slow and fast streams. In some cases, this interface is a tangential discontinuity, across which one finds most of the shear between the two streams (Belcher and Davis, 1971), and in other cases it is probably evolving into a tangential discontinuity. The stream interface is identified by an abrupt drop in density and a sharp rise in temperature (Burlaga, 1974), and a change in the azimuthal plasma flow angle relative to the radial direction.

In the distant heliosphere (which we define as the region between 2 - 10 AU), the forward and reverse shocks are well developed. The shocks can be identified by a sharp increase in solar wind speed along with a sudden increase in magnetic field intensity (Figure 1.4). Shocks are sites where particles can gain substantial energy. The particles are energized by being compressed between the shock front and the magnetic irregularities in the solar wind upstream from the shock, or by being compressed between upstream irregularities and those downstream from the shock (Fisk and Lee, 1980). Particles with energies as low as 5 keV (Palmer and Gosling, 1976) can be accelerated to the MeV range (1 electron volt, eV = 1.6×10^{-19} Joule). As shown in Figure 1.4, the MeV proton intensity typically peaks at the shocks and decreases substantially in the middle of the CIR at distances greater than 2 AU (Barnes and Simpson, 1976; Pesses et al., 1978).

In studying the energy spectrum of particles, the differential flux, dJ/d(E/m), is plotted against energy-per-mass, E/m, or the velocity distribution function, f(v), is plotted against velocity, v. For shock accelerated particles, the energy spectrum is found to be a power law, i.e., $f(v) = Av^{-\gamma}$, in the region close to the shock, as observed in CIRs (Barnes and Simpson, 1976; Pesses et al., 1978). Since the shock pair generally forms beyond ~2 AU, the energetic particles observed in CIRs at 1 AU

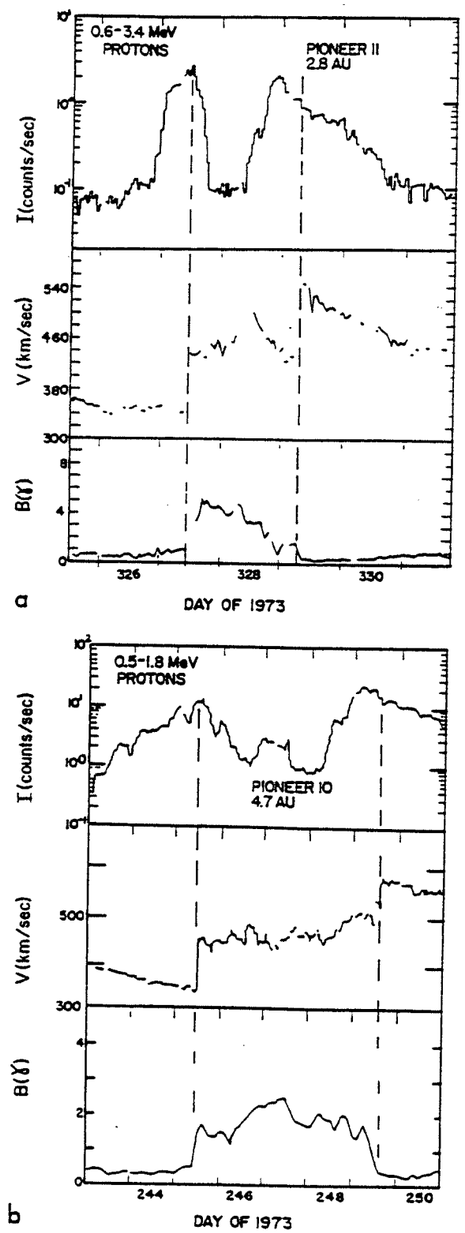

Figure 1.4. Time profiles of shock-associated energetic protons in CIR events observed near (a) 2.8 AU and (b) 4.7 AU from the Sun (Palmer and Gosling, 1978; adapted from Pesses et al. (1978) and Barnes and Simpson (1976).

are accelerated in the distant heliosphere and propagate back towards the Earth along magnetic field lines. The particles also lose energy because of the adiabatic deceleration in the expanding solar wind as they move sunward. This results in the spectrum becoming exponential, $f(v) = Ae^{-v/v_o}$, with the characteristic velocity, v_o, observed to be the same for all ions in the solar wind frame (Gloeckler et al., 1979; Fisk and Lee, 1980).

To summarize, a CIR is a region in space where fast solar wind collide with and overtake slow solar wind, and it typically lasts more than 1 solar rotation. The increased turbulence and pressure causes the region to expand creating forward and reverse shocks at the leading and trailing edges, respectively, beyond ~2 AU. Ions are accelerated at these shocks from the keV range to the MeV range, then move along the magnetic field lines. The CIR can be identified by its solar wind plasma and magnetic field signatures, and also by the associated accelerated ion population.

1.3 Previous Work

In 1963, the cosmic-ray experiment on the Explorer XIV spacecraft detected protons in the 3-20 MeV range recurring at the solar rotation period over several rotations at 1 AU (Bryant et al., 1965). Similar observations were also made by the cosmic-ray experiment on IMP-1 in late 1963 and early 1964 (Fan et al., 1965). These observations were different from those of solar energetic particle (SEP) events because there was no velocity dispersion among the various MeV energy levels. That is, particles of all observed energies were detected simultaneously rather than those with higher energies (faster) being observed first. Also, SEP events are discrete and do not corotate with the Sun, and they are typically associated with solar flares and type-IV radio bursts extending from the microwave to decameter region (Bryant et al., 1965). The energy spectra in corotating events are steep enough at high energies that the ions are rarely detected above 20 MeV (McDonald et al., 1975). The corotating ion

enhancements were associated with high speed solar wind streams (McDonald and Desai, 1971).

At first, the corotating MeV ions were thought to have originated from areas on the Sun called "M" regions (now called coronal holes). The idea was that particles were accelerated and stored on closed field lines above moderately active M regions. As the Sun rotates, these particles would leak out of the trapping region at the base of the field lines then diffuse out into interplanetary space and convect with the solar wind (McDonald and Desai, 1971). The particles would have to remain in the trapping region for at least one solar rotation.

McDonald et al. (1976) showed that the intensity of the corotating events increased with radial distance indicating that the phenomenon is interplanetary rather than solar. Using virtually identical detectors with energy range 1.2-2.1 MeV on the IMP-7 and Pioneer-11 spacecrafts, McDonald et al. studied corotating events simultaneously at 1 AU and up to 4 AU from 1973-1974. To their surprise, they found that the intensity of the corotating ions detected by Pioneer-11 in the outer heliosphere (2-4 AU) was larger by a factor of 10-20 than those measured at 1 AU by IMP-7.

In support of interplanetary acceleration, Marshall and Stone (1977) showed sunward streaming of the MeV ions in the solar wind frame at 1 AU. Using data from the Electron/Isotope Spectrometer on IMP-7, they examined the anisotropy of the protons in the energy range 1.3 - 2.3 MeV transforming the flux from the spacecraft frame of reference to the solar wind frame. They found that even though the mean observed streaming is away from the Sun in the spacecraft frame, the particles stream towards the Sun in the solar wind frame. This indicated that these MeV particles were being accelerated in interplanetary space as opposed to coming from the Sun.

Van Hollebeke et al. (1978) examined the radial variation of corotating energetic particle streams both in the inner and outer heliosphere using data from five different

spacecrafts for time periods between 1973 - 1976. Proton measurements of 0.9 - 2.2 MeV were made from Helios 1 and 2 between 0.3 and 1 AU, from IMP-7 at 1 AU, from Pioneer 11 at 3.8 AU, and from Pioneer 10 between 9 and 10 AU. The particle intensity increased as the ions traveled from 0.3 to 1 AU with a positive gradient of 350% per AU. The gradient was variable between 1 AU and 3 - 5 AU with an average value of 100% per AU. Observations at ~4 AU compared to those at 9 AU indicated a negative gradient which varied from -40% per AU to -100% per AU. Similar results were also reported by Kunow et al. (1977) and Christon and Simpson (1979).

With convincing evidence for corotating events being an interplanetary phenomenon as opposed to a solar one, the focus shifted to the nature of this interplanetary acceleration process and the initial source of energetic particles or seed population. The composition and energy spectra of the accelerated ions can give important clues to answering these questions.

The first composition measurements in corotating events were reported by McGuire et al. (1977). They found that the abundance of carbon and helium relative to oxygen was significantly greater in corotating streams than in flare-associated events in the energy range 3 - 20 MeV per nucleon at 1 AU using IMP-8 data (as shown in Tables 1.2 and 1.3). The C/O ratio, approximately equal to 1 (Scholer et al., 1979a; Gloeckler et al., 1979) is also greater than that observed in the solar wind (von Steiger et al, 1997). In a follow-up paper covering the period 1972 - 1976, McGuire et al. (1978) showed that the H/He ratio (22 ± 5) between 1.5 - 8.8 MeV per nucleon was essentially identical to the value (21 ± 3) obtained by Bame et al. (1975, 1977) in high speed solar wind streams. Christon and Simpson (1979) found similar results in the energy range 0.5 - 1.8 MeV per nucleon and that the H/He ratio was relatively constant between 0.46 - 2.2 AU. Scholer et al. (1979a) and Gloeckler et al. (1979) calculated the H/He ratio to be between 11 - 15 in the energy range 0.54 - 1.0 MeV per nucleon using the ultralow-energy telescope (ULET) sensor on IMP-8. In all cases the H/He

ratio was at least 2 times smaller in corotating events during solar minimum conditions than in SEP events.

The first reported composition measurements well beyond the orbit of Earth around 4 AU were made using instruments on Voyagers 1 and 2 for the energy range 0.7 - 1.2 MeV per nucleon (Hamilton et al., 1979). The He/H ratio is similar to that measured at 1 AU, but the C/O ratio is less, around 0.68. All previously mentioned work on corotating events were made near solar minimum when these events are long-lived, more intense and more prevalent. However these observations were made during the approach to solar maximum in 1978 when SEP events were more frequent.

Table 1.1. CIR abundances relative to oxygen in slow (<600 km/s) and fast (>600 km/s) solar wind streams at 1.9-2.8 MeV/amu for the period 1978-1986 at 1 AU (Richardson et al., 1993).

	V_{sw} < 600 km/s	V_{sw} > 600 km/s	SMCE*
H	2300 ± 200	2500 ± 100	2700 ± 200
^{4}He	54 ± 23	130 ± 35	160 ± 50
C	0.62 ± 0.06	0.89 ± 0.05	0.89 ± 0.10
N	0.15 ± 0.02	0.15 ± 0.01	0.14 ± 0.01
O	1.0	1.0	1.0
Ne	0.15 ± 0.02	0.17 ± 0.02	0.20 ± 0.04
Mg	0.19 ± 0.03	0.14 ± 0.01	0.13 ± 0.03
Si	0.09 ± 0.02	0.11 ± 0.01	0.08 ± 0.02
S	0.06 ± 0.02	0.05 ± 0.01	0.06 ± 0.01
Fe	0.14 ± 0.02	0.099 ± 0.01	0.096 ± 0.05
H/^{4}He	43 ± 18	19 ± 5	17 ± 7

* Solar minimum corotating events: Gloeckler et al. (1979), Scholer et al. (1980), McGuire et al. (1978), Christon and Simpson (1979), and von Rosenvinge and McGuire (1985).

Table 1.2. SEP, photospheric, and slow (<600 km/s) and fast (>600 km/s) solar wind core plasma abundances relative to oxygen.

	SEP*	Slow Solar Wind†	Fast Solar Wind†	Photosphere§
H	1170 ± 89#	1890 ± 600	1590 ± 500	1175
^{4}He	55 ± 3	93 ± 31	83 ± 25	114
C	0.48 ± 0.02	0.72 ± 0.10	0.70 ± 0.10	0.43
N	0.13 ± 0.01	0.129 ± 0.008	0.145 ± 0.011	0.13
O	1.0	1.0	1.0	1.0
Ne	0.15 ± 0.01	0.17 ± 0.02	0.136 ± 0.011	0.14
Mg	0.21 ± 0.01	0.16 ± 0.03	0.083 ± 0.02	0.044
Si	0.15 ± 0.01	0.19 ± 0.04	0.054 ± 0.009	0.041
S	0.035 ± 0.004	0.05 ± 0.02	0.022 ± 0.008	0.019
Fe	0.16 ± 0.02	0.12 ± 0.03	0.057 ± 0.007	0.055
H/^{4}He	67 ± 10	25 ± 8	21 ± 2	10

* Cane et al. (1991)
† von Steiger et al. (1997)
# Reames et al. (1994)
§ Anders and Grevesse (1989) with uncertainties of ±9%.

The spectra of the ions accelerated in corotating events at 1 AU are exponential in character. By plotting the ion distribution function against velocity, Gloeckler et al. (1979) found that a simple exponential fit the data best for all observed species, H, He, C, O, and Fe. The *e*-folding speed of the distribution was found to be the same for all ions over a wide energy range, from ~0.15 to 8 MeV per nucleon. Van Hollebeke et al. (1979) found that the differential intensity spectrum for protons and helium ions was exponential in velocity and that the *e*-folding velocity was the same for the two species.

Mewaldt et al. (1979) found that for a large number of events the differential intensity was exponential in velocity, but with significantly different *e*-folding velocities for protons and helium ions. The *e*-folding velocity was also observed to be essentially independent of radial distance (Van Hollebeke et al., 1979).

The corotating MeV enhancements were linked to corotating interaction regions (CIRs) by Barnes and Simpson (1976). Beyond ~2.5 AU the leading and trailing edges of the CIRs were observed to be bounded by forward-reverse shock pairs (Smith and Wolfe, 1976, 1977; Hundhausen and Gosling, 1976). The corotating MeV ion flux increases changed in character between 1 and 4 AU. At 1 AU the energetic proton stream enhancements displayed single peaks. In the outer heliosphere, these proton streams developed into double-peak structures, and the peaks occurred essentially at the forward-reverse shock pair bounding the CIR with a depleted region in between (Barnes and Simpson, 1976; Pesses et al., 1978). The time integrated flux at the reverse shock was usually greater than that at the forward shock, and the He/H ratio was found to be at least five times less at the forward shock than at the reverse shock (Barnes and Simpson, 1976). The spectra are steeper at the forward shock than at the reverse shock (Barnes and Simpson, 1976; Pesses et al., 1978).

It was apparent that shocks played an important role in the acceleration mechanism of CIRs. Palmer and Gosling (1978) were the first to apply shock acceleration theory to CIRs, where the particles are energized via the Fermi model (Fermi, 1949; Axford, 1977; Blandford and Ostriker, 1978). However, they were not able to account for many of the observations. Fisk and Lee (1980) improved upon this model by adding adiabatic deceleration, which is important because CIRs span several AU. In this model, particles are accelerated at the forward and reverse shocks by being compressed between the shock front and magnetic irregularities in the solar wind upstream from the shocks, or by being compressed between upstream irregularities and those downstream from the shocks. The particles also suffer adiabatic

deceleration in the expanding solar wind. It was assumed that the energized particles moved only along, and not across, the magnetic field lines.

Another type of shock acceleration process is referred to as the "**V x B**" mechanism or shock drift acceleration (Sonnerup, 1969; Chen and Armstrong, 1975; Pesses et al., 1979; Decker, 1981; Pesses, 1982). In this mechanism, the particles are accelerated during a single shock encounter and gain energy by drifting in the inhomogeneous magnetic field at the shock front in a direction parallel to the **V** x **B** electric field, where **V** is the plasma bulk velocity and **B** is the magnetic field. In the Fermi mechanism, the acceleration requires multiple shock encounters due to elastic scattering in magnetic irregularities upstream and downstream of the shock. However, Lee and Fisk (1982) explained that these two mechanisms are essentially the same, and that the distinction arose from the theoretical views to the two limiting cases of one shock encounter versus many encounters.

Chen and Armstrong (1975) found that shock acceleration is most effective for particles with velocities between 10 - 100 times that of the shock front relative to the upstream solar wind speed. For CIRs, this velocity range is typically 1000 - 15000 km/s corresponding to 5 keV to 1 MeV protons (Palmer and Gosling, 1978). This meant that the particles were not being accelerated directly out the solar wind, but possibly from its suprathermal tail, as suggested earlier (McDonald et al., 1976). Scholer et al. (1980) observed that the intensity of the 1.5 MeV protons increased monotonically with the solar wind temperature, thereby concluding that the thermal solar wind ions can be a source of ions accelerated in CIRs.

The Fisk and Lee model (1980) was able to account for almost all the observations mentioned previously. The observed exponential character of the spectra (Gloeckler et al., 1979; Van Hollebeke et al., 1979), the independence of the *e*-folding velocity with radial distance (Van Hollebeke et al., 1979), the observed radial gradients in intensity (Kunow et al., 1977; Van Hollebeke et al., 1978; Christon and

Simpson, 1979), the observed differences in the intensity and spectra at the forward and reverse shocks (Barnes and Simpson, 1976; Pesses et al., 1978), and the independence of spectral shape with species (Gloeckler et al., 19 79) are all accounted for in the model.

Using data from the Energetic Proton Anisotropy Spectrometer on the ISEE-3 spacecraft, ions in the ambient slow wind (S) and ambient fast wind (F) CIR regions with energies between 35 - 1000 keV were shown to stream towards the Sun, whereas those in the compressed fast wind (F') region with energies between 35 - 91 keV streamed away from the Sun, as shown in Figure 1.5 (Richardson and Zwickl, 1984; Richardson, 1985). Upon further analysis of this data set, Richardson (1985) determined that solar wind ions can be statistically accelerated to energies up to ~ 300 keV via a second order Fermi process by scattering from Alfvén waves, and that the acceleration conditions favors the F' region. These statistically accelerated ions can then be the source population for shock acceleration in the distant heliosphere, where the ions are further accelerated to MeV energies.

A comprehensive survey of 64 CIR events was performed using ion data with energy above 1 MeV/amu from the ISEE-3, IMP-8, and Helios-1 spacecrafts covering the period 1978 - 1986 during pre-solar maximum to near solar minimum conditions at 1 AU (Richardson et al., 1993). The ion intensities in these events were not correlated with the solar cycle indicating that CIR events are not accelerated out of a background low energy SEP source population. These authors found that the ion abundances were correlated with the solar wind speed (see Table 1.1). They also showed that the ion abundances in CIRs are ordered relative to photospheric abundances by first ionization potential (FIP), similar to observations by Reames et al. (1991). In the FIP effect, abundances of elements in the corona with FIP less than ~10 eV (Ca, Mg, Fe, and Si) are about 4 times greater than those with higher FIPs (S, C, O, N, Ne, and He) in

relation to photospheric abundances (Meyer 1985a, b; Vauclair and Meyer, 1985; von Steiger and Geiss, 1989).

The out-of-ecliptic Ulysses Mission literally added a new dimension to the study of CIRs. As the spacecraft traveled to higher and higher heliographic latitude in the southern hemisphere, Gosling et al. (1993) observed the forward shocks propagating to lower latitudes and the reverse shocks to higher latitudes with increasing heliocentric distance. These observations agreed with the predictions of a three-dimensional model (Pizzo, 1991, 1994) of corotating solar wind flows that originate in a tilted dipole geometry back at the Sun (see Figure 1.6).

Using data in the energy range 0.6 - 60 keV/e from the Solar Wind Ion Composition Spectrometer (SWICS) on Ulysses at 4.5 AU, Gloeckler et al. (1994) were the first to show that interstellar pickup H^+ and He^+ ions are accelerated in CIRs. Pickup ions are generated from interstellar neutral particles that enter our solar system by the motion of the Sun relative to the interstellar medium (see review by Axford (1972)). The particles are ionized by photo-ionization and charge exchange, and then forced to gyrate about the interplanetary magnetic field. The pickup ion distribution is typically flat from 0 - 2 V_{SW} (the solar wind speed) with a sharp cut off at 2 V_{SW} in the ambient solar wind (Möbius et al., 1985; Gloeckler et al., 1993). Due to the increased densities in CIRs, the flux of the pickup ions is enhanced because of the increased charge exchange of neutrals with the solar wind. Gloeckler et al. (1994) found that the accelerated pickup He^+ abundance is greater than the solar wind He^{2+} abundance beyond 2 V_{SW} as measured in the S' CIR region at 4.5 AU (see Figure 1.7), suggesting that the pickup ions are the more dominant seed population in the distant heliosphere.

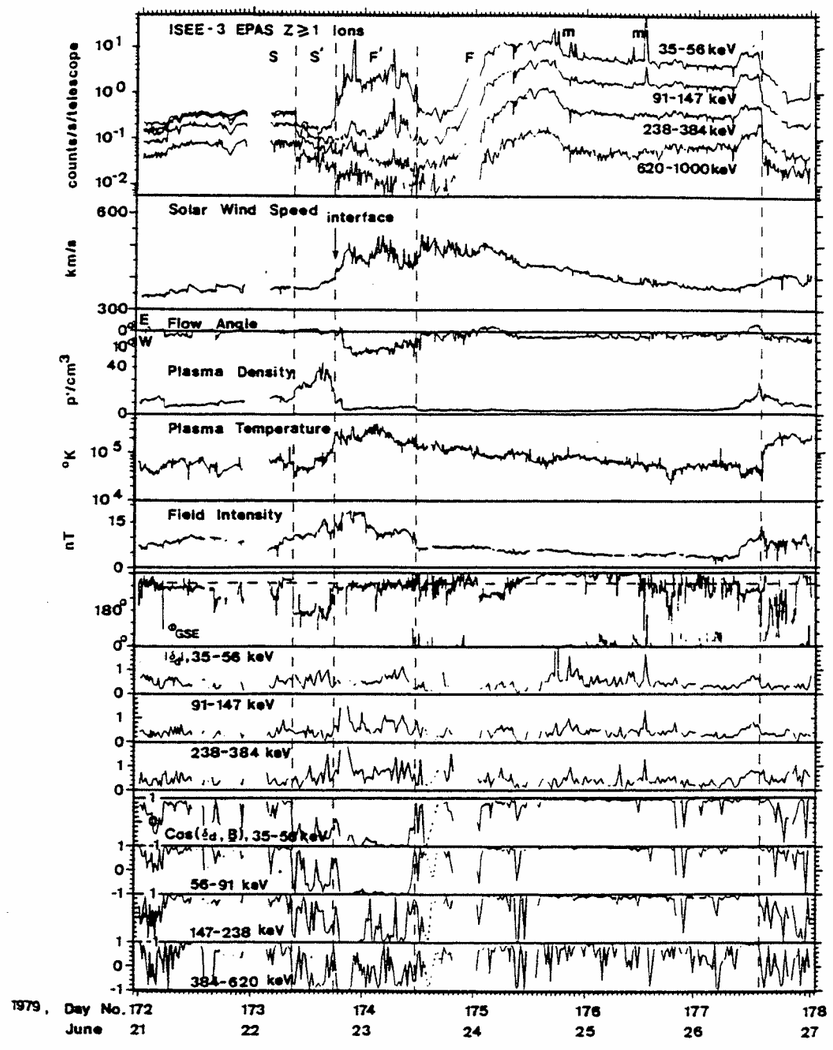

Figure 1.5. ISEE-3 EPAS, solar wind plasma, and magnetic field data for 21-26 June 1979. The magnitude of the anisotropy, $|\delta_d|$, and the cosine of the angle between the anisotropy and the magnetic field, $\cos(\delta_d,B)$, are plotted for various EPAS energy channels. The ion enhancements between 35-91 keV in the compressed fast stream plasma (F' region) shows antisunward field-aligned streaming as $\cos(\delta_d,B) \approx -1$ (Richardson and Zwickl, 1984).

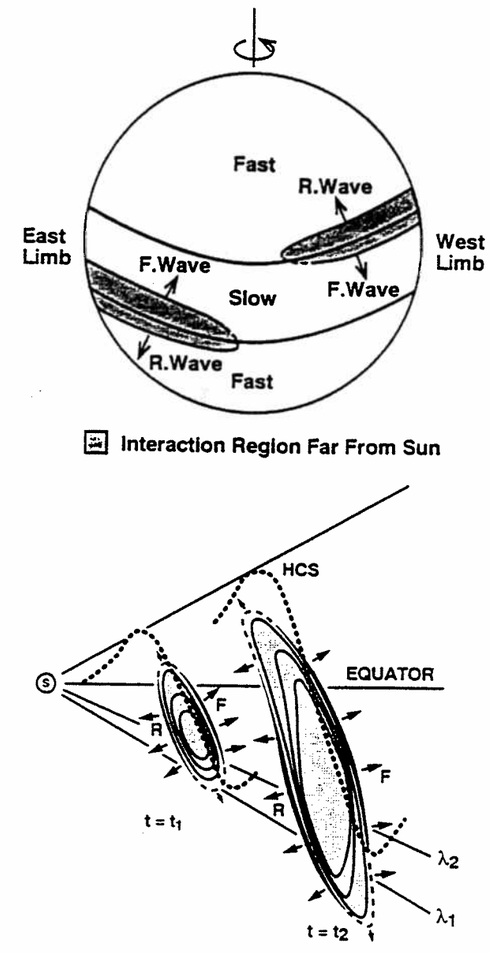

Figure 1.6. (Top) A sketch illustrating the origin of tilted interaction regions in interplanetary space in terms of a tilted-dipole geometry back at the Sun. (Bottom) Snapshots of the southern interaction region at two different times (t_1 and t_2) in an arbitrary meridional plane. Note that the interaction region is tilted in the same sense as is the heliospheric current sheet, HCS (dotted line). The solid line surrounding the interaction region marks the forward (F) and reverse (R) shocks (Gosling et al., 1993).

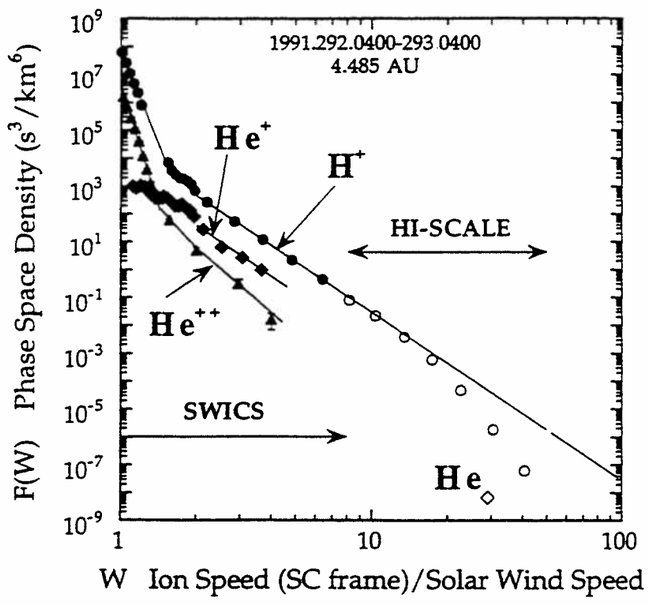

Figure 1.7. Velocity distribution functions of H^+ (solid circles), He^+ (solid triangles), and He^{++} (solid diamonds) in the spacecraft frame. Data below W ~ 8 (0.6 to 60 keV/e) are obtained with SWICS, while those above W ~ 8 (open circles for ions, mostly protons, and open diamond for He) are measured with the HI-SCALE instrument. Interstellar pickup H^+ appears as a bump on the spectrum below W = 2. The accelerated solar wind H^+ and He^{++} ($1.1 < W < 1.5$) have steep power law spectra with respective indices of ~ -22 and ~ -30. Accelerated pickup H^+ and He^+ (W > 2) have identical spectral shapes that are less steep than that of accelerated solar wind He^{++} above W ~ 1.5, which is a power law of index ~ -8 (Gloeckler et al., 1994).

Gloeckler et al. (1994) also suggested a two step acceleration process where the pickup ions are first pumped up to suprathermal energies by some statistical mechanism, then shock acceleration further increases the energy to the MeV range. Schwadron et al. (1996) determined that the pickup ions can be statistically accelerated via transit-time damping as this model accounted for the observed distribution functions. In the transit-time damping model (Fisk, 1976), low-energy particles are continually accelerated in transit from the Sun by interacting with the propagating fluctuations in the magnitude of the interplanetary magnetic field (e.g., magnetosonic waves).

The observations from the energetic particle experiments on Ulysses (HI-SCALE, EPAC and COSPIN) at high heliographic latitude (Simnett et al., 1994, 1995; Sanderson et al 1994) were similar to previous in-ecliptic measurements in CIRs (Barnes and Simpson, 1976). That is, the peak in the MeV ion intensity was greater at the reverse shock than at the forward shock, and the H/He ratio increased around the forward shock and decreased towards the reverse shock. However, the peak H/He value at either shock at high latitudes was less than the in-ecliptic values, and the intensity of the energetic particles increased up to latitude 20°S then decreased (Simnett et al., 1994, 1995). The intensity of the 1 MeV protons was observed to be independent of the shock normal at all latitudes and well correlated with the shock strength between 29° - 41° (Desai et al., 1997). The He, C, and O abundances are enhanced with latitude (Simnett et al., 1994; Fränz et al., 1995; Maclennan and Lanzerotti, 1995).

In the CIR shock acceleration model (Palmer and Gosling, 1978; Fisk and Lee, 1980) particles are energized by the shocks then move parallel to the magnetic field lines away from the shocks. The observed depletion of MeV ions between the peaks at the forward and reverse shocks is accounted for by the parallel motion of the ions away from the shocks (Barnes and Simpson, 1976; Pesses et al., 1978). Numerical

computations by Pizzo (1989) and Hu (1993) calculated the depleted region to be 12-17 hours on either side of the stream interface in the distant heliosphere. However, Ulysses measurements near 5 AU between 20 - 30 degrees south latitude and Pioneers 10 and 11 in-ecliptic observations between 4 - 6 AU found that the energetic ions associated with the reverse shock extended all the way to the stream interface, which is not magnetically connected to either shock (Intriligator et al., 1995; Intriligator and Siscoe, 1994; Tsurutani et al., 1982). The overabundance of MeV ions close to the stream interface was explained using cross-field diffusion in which the particles move across the magnetic field lines to enter this region (Intriligator and Siscoe, 1995; Tsurutani et al., 1982).

With the launch of the WIND spacecraft in November 1994 during solar minimum conditions, the spacecraft encountered many intense CIRs during the first nine months of its mission. The high-sensitivity energetic particle experiment (EPACT) measured a single corotating event continuously for about 17 days at 1 AU (Reames et al., 1997b). Mason et al. (1997) found that the abundances of C and Ne relative to O at 150 keV/nucleon increased with solar wind speed. The spectra of the heavy ions continued to rise at low energies displaying a power law distribution and did not roll over as expected from the Fisk and Lee model (1980), which yields an exponential (Mason et al., 1997; Reames et al., 1997b).

Using data from the EPACT-STEP sensor along with the solar wind plasma data (SWE) and the magnetometer data (MFI) from WIND, Dwyer et al. (1997) transformed the 0.02 - 1.20 MeV/nucleon He data to the solar wind frame and examined the anisotropy direction of particles relative to the azimuthal magnetic field direction for three different CIRs. They found that although the particles generally streamed towards the Sun in the solar wind frame, the particle anisotropy did not line-up with the magnetic field, and concluded that there was significant transport perpendicular to the field, in agreement with conclusions of previous authors

(Intriligator and Siscoe, 1994, 1995; Intriligator et al, 1995; Tsurutani et al., 1982). However, this result is not accounted for in the conventional CIR model, which expects particles to move primarily along the magnetic field lines (Fisk and Lee, 1980).

All in all, the generally accepted CIR model of Fisk and Lee (1980) was able to account for most of the observations available at that time (McDonald et al, 1976; Barnes and Simpson, 1976; Pesses et al., 1978; Van Hollebeke et al., 1978; Gloeckler et al 1979; Christon and Simpson, 1979). Since the time the model was developed, the *in situ* measurements using better instrumentation with higher sensitivity and lower energy thresholds have greatly improved our understanding of CIRs and may require modifications to the model. The source population should include both solar wind ions and pickup ions with the relative contribution of each varying with distance away from the Sun (Gloeckler et al., 1994). The acceleration process may involve a two-step scenario where the seed ions are first statistically accelerated up to a few 100 keV in energy, then shock accelerated to MeV energies (Richardson 1985; Schwadron et al, 1997). After the particles are energized, recent studies suggest that there may be significant motion across and not just parallel to the magnetic field lines (Intriligator and Siscoe, 1994, 1995; Intriligator et al., 1995; Dwyer et al., 1997). There have been significant advances in our understanding of CIRs over the past thirty years, but more research needs to be done in order to fully understand this phenomenon. The source population, acceleration mechanism, and transport mechanism are still being debated.

1.4 Thesis Overview

The work in this thesis is devoted to gaining a better understanding of ion propagation and acceleration within CIRs. Based on the existing knowledge of ion acceleration and transport within CIRs we review a number of the basic questions of CIR acceleration which remain partially unanswered:

1) Which ion populations are most readily accelerated? Evidence has shown that higher temperature solar wind ions are more readily injected into the acceleration process. However the complementary role of the more energetic pickup ions is not yet fully understood.

2) How are these ion populations accelerated? Clear evidence has been obtained that both statistical and shock acceleration mechanisms play important roles but a definitive model has not yet emerged. Cross-field diffusion may play an important role in shock acceleration, but tighter observational constraints for cross-field diffusion are necessary.

3) Where are the ions accelerated? In the context of observations near 1 AU, where CIRs are not yet fully formed, conventional wisdom indicates that the acceleration occurs radially beyond the point of observation. Is this consistent with the distributions and streaming observed for the various ion populations.

The main conclusions in this work are organized about these three central questions.

The Supra-Thermal Ion Composition Spectrometer (STICS) is ideally suited to address these topics. The energy range (6 - 200 keV/e) of STICS allows us to examine the spectra of both the source population and accelerated ion population at the same time. Since STICS can measure the charge state of an ion, it can distinguish between solar wind He^{2+} and pickup He^{+} providing the opportunity to study the importance of pickup ions versus solar wind ions as the source population of CIR accelerated ions at 1 AU. The ions' directional information can be used to determine the anisotropy in the solar wind frame examining whether or not the accelerated particles move across the

magnetic field lines. It must be emphasized here that the ability to discriminate between solar wind hydrogen and helium, H^{+}, He^{2+}, and pickup helium, He^{+}, the ability to recover full distribution functions at 1 AU in this unique energy range, and the ability to recover fine sector information is unique to the STICS instrument. Many of the spectra described in this thesis have never before been examined near 1 AU.

The thesis is roughly divided into two parts. The first part, Chapters 2 and 3, develop the tools necessary to provide a physically meaningful description of the data. The second part, Chapters 4 and 5, describe two specific applications of these tools to shed light on the questions described above. A more detailed outline follows.

In Chapter 2, a brief overview of the WIND mission is given, followed by a description of how STICS works. The different types of STICS data (telemetry) transmitted back to the Earth are also described in this chapter. Chapter 3 explains how the ion information (charge, mass, direction,...) is extracted from the telemetry data. The corrections (instrument response function) made to the number of counts to convert it to physically meaningful quantities (differential flux or distribution function) are also explained in Chapter 3.

Chapter 4 deals with the composition and spectra of H^{+}, He^{2+}, and He^{+} as measured by STICS. An extended helium spectrum, mainly He^{2+}, is presented by combining STICS data with those of SMS-MASS at solar wind energies and those of EPACT-STEP at higher energies up to 1 MeV. In some sense this extended distribution function represents an observational overview of helium acceleration in CIRs from the seed population to strongly accelerated ions. The extended distribution also represents a cross-calibration for three sets of independent WIND instruments. As a full theoretical model emerges, this spectrum, or its like, must be explained. The relative abundances of He^{+} (pickup ions), He^{2+}, and H^{+} are also examined in detail, providing important insights regarding the injection of seed populations into the acceleration process. Through comparison of the relative abundance of He^{+}/He^{2+}

observed by the WIND spacecraft at 1 AU to that observed by Ulysses at 4.5 AU (Gloeckler et al., 1994), the injection process is further constrained. Finally in Chapter 4, detailed comparisons are performed between observed distributions and those predicted by Fisk and Lee (1980). The comparisons allow constraints of many of the parameters of acceleration and propagation and ultimately suggest a reasonable interpretation of the observations.

In general, Chapter 4 provides important clues from the distributions observed by the STICS instrument regarding which ion populations are most readily accelerated, and where they are most readily accelerated. The details of the acceleration process although not explicitly illuminated are in principle strongly constrained by the extended helium distributions reported.

In Chapter 5, the sector information of the STICS instrument is exploited in order to derive anisotropies for H^+ and He^{2+}. Our results are then compared to those of EPACT-STEP reported by Dwyer et al. (1997) for higher energy ions. In general the observations reported in this chapter suggest that either there is significant, perhaps even excessive, cross-field diffusion. We will also suggest an alternative viewpoint in which small scale fluctuations in a field-aligned anisotropy conspire to yield an anomalous cross-field streaming.

The major results of this dissertation are summarized in Chapter 6.

CHAPTER 2: INSTRUMENTATION

This Chapter contains a description of the instrument used in this study. The chapter is introduced with a brief overview of the WIND mission followed by a summary of the Solar Wind, Mass, and Suprathermal Ion Composition (SMS) investigation on WIND. The main instrument used in this work is the suprathermal SMS sensor (STICS). The way STICS works and its angular resolution are discussed in Section 2.3. The STICS data transmitted from the spacecraft to the Earth are reviewed in Section 2.4.

2.1 The WIND Mission

The WIND spacecraft was sucessfully launched on November 1, 1994. It is the first of two missions in the Global Geospace Science (GGS) initiative, the other being POLAR (launched February 24, 1996). The main focus of GGS is to greatly improve the understanding of the flow of energy, mass, and momentum in the solar-terrestrial environment with particular emphasis on the near-Earth region (Acuna et al., 1995). While WIND is mainly concentrating on the region upstream of the Earth's magnetosphere and bow shock, POLAR is focusing on the Earth's magnetosphere with a 2 x 9 Earth radii (R_e) polar orbit.

The GGS program is part of the US contribution to the International Solar Terrestrial Physics (ISTP) program. ISTP is a joint effort by the United States, Europe, Russia, and Japan to understand the physics of the behavior of the solar-terrestrial system in order to predict how the Earth's atmosphere will respond to changes in the solar wind. The Japanese Institute of Space and Astronautical Science (ISAS) launched GEOTAIL, which has been collecting data in the Earth's geomagnetic tail since 1992. The SOHO and CLUSTER Programs are the European Space Agency's (ESA) contribution to the ISTP effort. SOHO was successfully launched in December 1995, but CLUSTER was destroyed during its launch in June 1996.

CLUSTER is now being rebuilt by the ESA. The InterCosmos Agency (IKI) of the former USSR and Eastern European countries contributed its INTERBALL set of four spacecrafts (Whipple and Lancaster, 1995). INTERBALL-TAIL was launched on August 3, 1995 and INTERBALL-AURORA, on August 29, 1996.

The WIND mission was designed to measure the properties of the solar wind before it reaches the Earth. The initial orbit consisted of a series of lunar swingbys causing the spacecraft to move quickly in and out of the Earth's magnetosphere (Figure 2.1). This allows WIND to study the Earth's bow shock, magnetosheath, magnetosphere, and the corresponding boundary layers. WIND spent several months in 1995 and 1997 in a halo orbit around the Lagrangian point (L1) between the Earth and the Sun, about 240 Earth radii (1 R_e = 6380 km) from the Earth, where it continuously monitored the solar wind. There are eight instruments on the spacecraft which consists of twenty-four separate sensors. These state-of-the-art instruments are optimized for measuring waves, fields, and particle distributions of space plasmas. Table 2.1 gives a summary of these instruments. The spacecraft itself is cylindrical in shape with a diameter of 2.4 m and a height of 1.8 m and spins at a rate of ~20 rpm (Harten and Clark, 1995), see Figure 2.2. Throughout the entire mission the spin axis will be normal to the ecliptic plane with the spacecraft +z axis (Figure 2.2) pointing in the -z Geocentric Solar Ecliptic (GSE) direction.

2.2 The Solar Wind, Mass, and Suprathermal Ion Composition Experiment (SMS)

The Solar Wind, Mass and Suprathermal Ion Composition (SMS) investigation is making major contributions to the global objectives of ISTP. It is designed to measure, under all conceivable solar wind flow conditions, (1) the elemental and isotopic composition of solar wind ions, and (2) the differential energy spectra, abundances and charge states of all dominant species from H to Fe with energies

between 0.5 to 230 keV/e (Gloeckler et al., 1995). This experiment consists of three separate sensors: the Solar Wind Ion Composition Spectrometer (SWICS), the high-resolution MASS spectrometer (MASS), and the Supra-Thermal Ion Composition Spectrometer (STICS), serviced by a common data processing unit (DPU).

SWICS uses electrostatic deflection followed by a time-of-flight (TOF) and energy measurement. After particles pass through the SWICS deflection system, they are accelerated in order to increase the energy of the solar wind ions above the 30 keV threshold of the low-noise solid-state detector in the time-of-flight system. SWICS was designed to measure the abundances of about forty different ions in the solar wind and to give their speed and kinetic temperature.

MASS uses electrostatic deflection followed by a time-of-flight measurement but does not require an energy measurement. The MASS sensor is the first instrument flown that can routinely measure the isotopes of the solar wind elements heavier than helium because of its high-mass resolution ($M/\Delta M > 100$). MASS is characterizing in detail the matter entering the magnetosphere by measuring the elemental and isotopic composition of the solar wind.

STICS also uses electrostatic deflection followed by a time-of-flight (TOF) and energy measurement, but has no post acceleration. STICS characterizes the interplanetary suprathermal ion populations by measuring the three-dimensional distribution functions of H, He, C, O, Si, and Fe for direct comparision with ion populations inside the magnetosphere. STICS is also used for pick-up ion studies.

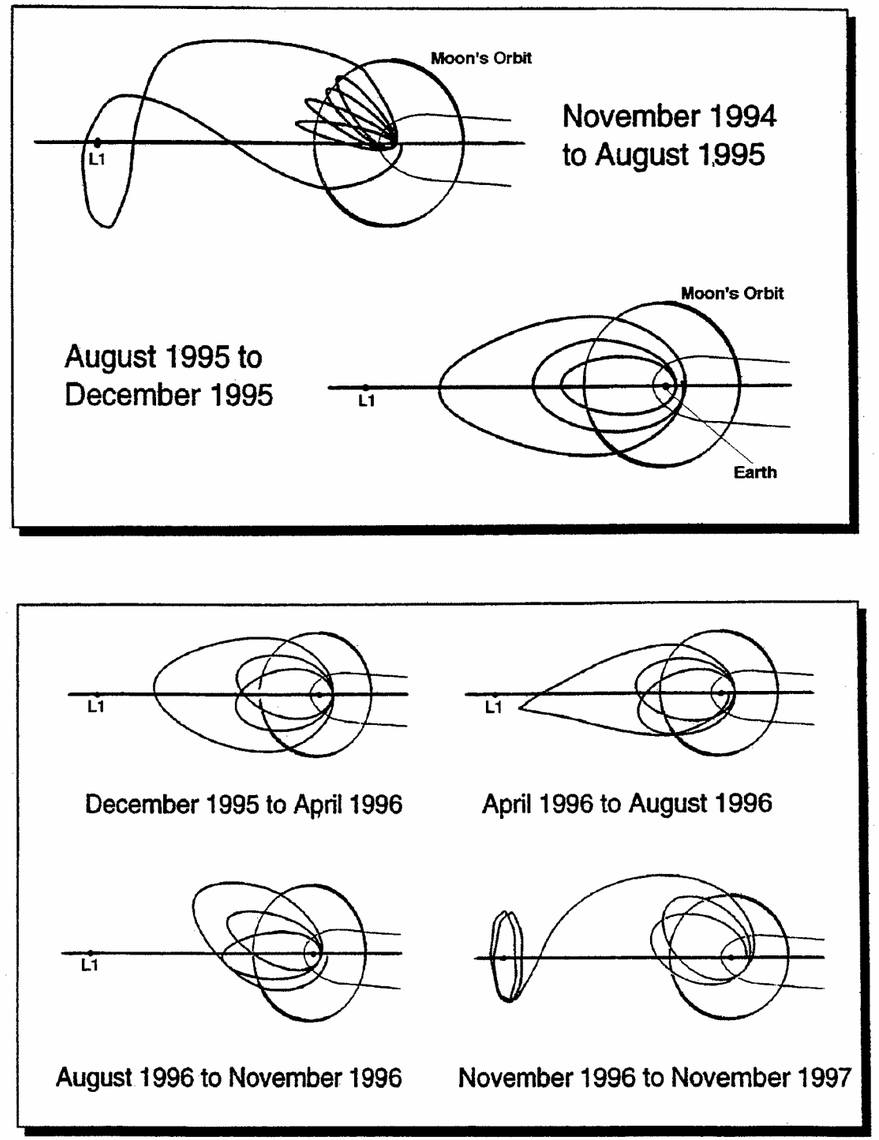

Figure 2.1. The WIND trajectory at different stages during the mission (GSE X-Y projection).

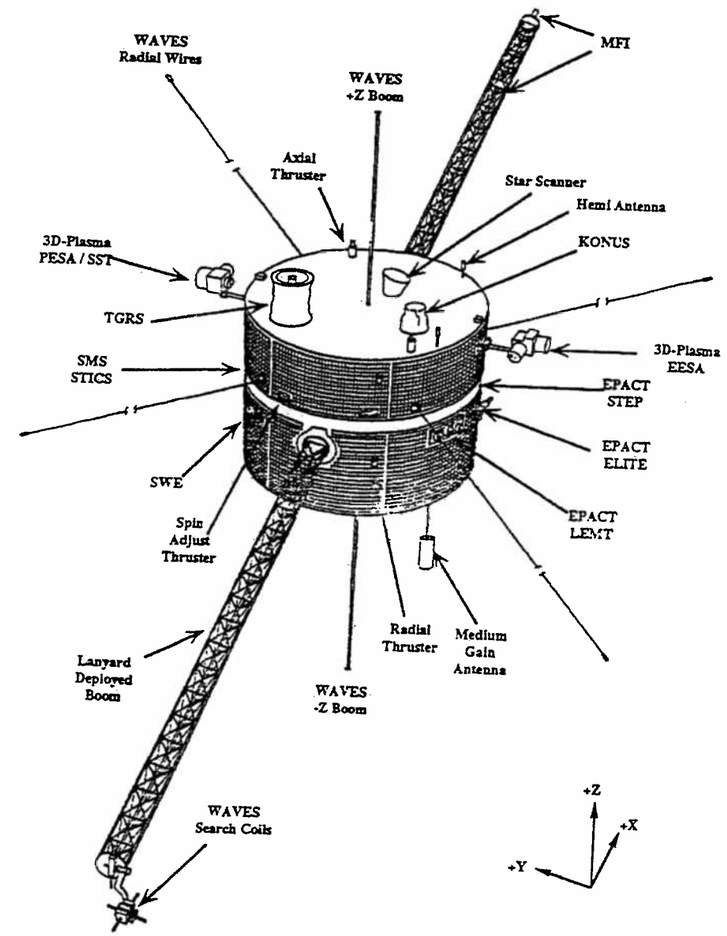

Figure 2.2. The WIND spacecraft and its sensors (Harten and Clark, 1995).

Table 2.1. Summary of the different instruments on the WIND spacecraft, the principal investigator (P.I.) for each instrument, and the P.I.'s institution (Harten and Clark, 1995).

Instrument	Description	Principal Investigator
Magnetic Field Investigation (MFI)	d/c magnetic fields	R. Lepping (NASA/GSFC)
Radio and plasma wave experiment (WAVES)	a/c electric/magnetic fields 8 Hz-16 MHz	J. Bougeret (Obs. de Paris) M. Kaiser (NASA/GSFC)
Solar Wind Experiment (SWE)	Mass, energy, direction of low energy ions and electrons 7 eV - 22 keV	K. Ogilvie (NASA/GSFC)
3-D Plasma (3-DP)	Distribution and energy of ions and electrons in range 3 eV-30 keV and 20 keV-11 MeV (SST)	R. Lin (U.C. Berkeley)
Energetic Particles: Accelertaion, Composition Transport (EPACT)	Mass, energy, direction of ions in range 0.2-500 MeV	T. von Rosenvinge (NASA/GSFC)
Solar wind/Mass Suprathermal ion composition studies (SMS)	Mass, energy with angular resolution of ions in range 0.5-230 keV/e	G. Gloeckler (U. of Maryland)
Transient Gamma-Ray Spectrometer (TGRS)	High spectral resolution gamma-ray detector in range 15 keV to 10 MeV	B. Teegarden (NASA/GSFC)
KONUS (Russian instrument)	High time resolution gamma-ray detector	E. Mazets (IOFFE Institute Russia)

2.3 The Supra-Thermal Ion Composition Spectrometer

STICS can determine the mass, charge state, and mass per charge of the ions, their arrival directions both in and out of the ecliptic plane, and their energy-per-charge (E/Q). STICS uses an electrostatic deflection system to select ions of a given energy-per-charge value followed by a time-of-flight (TOF) measurement of the ions. The total ion energy is then measured with a solid state detector. The combination of these measurements allows the determination of the mass, charge, and energy of the incoming ions. Due to its angular resolution and the large angular acceptance, STICS can therefore determine the full three-dimensional distribution functions of suprathermal ions in the energy range 6.2 - 223.1 keV/e.

Physically, STICS is made up of two units: the STICS sensor and the Analog Electronics (AE) Box (Figure 2.3). The sensor contains the deflection system, three time-of-flight telescopes, high voltage (HV) power supplies for the deflection system, the microchannel plates, and the detector pre-amplifiers. The remainder of the analog electronics, including the shaping amplifiers, discriminators, time-of-flight circuits, analog-to-digital converters (ADC), valid-event logic circuits (for the pulse height), and the low voltage power supply are located in the separate Analog Electronics Box. This separation frees the mechanical and thermal design of these circuits from the constraints imposed by the odd shape of the sensor package. Outputs from the Analog Electronics Box are sent to the SMS Data Processing Unit (DPU) where they are processed then submitted to the spacecraft telemetry (Galvin, 1991).

2.3.1 Principle of Operation

Figure 2.4 shows a simplified cross-sectional view of the STICS sensor. For a more detailed description see Gloeckler et al. (1995). Particles enter the spherical electrostatic deflection system through a simple aperture which includes a light trap. The light trap is important because the TOF section is senstive to ultraviolet radiation.

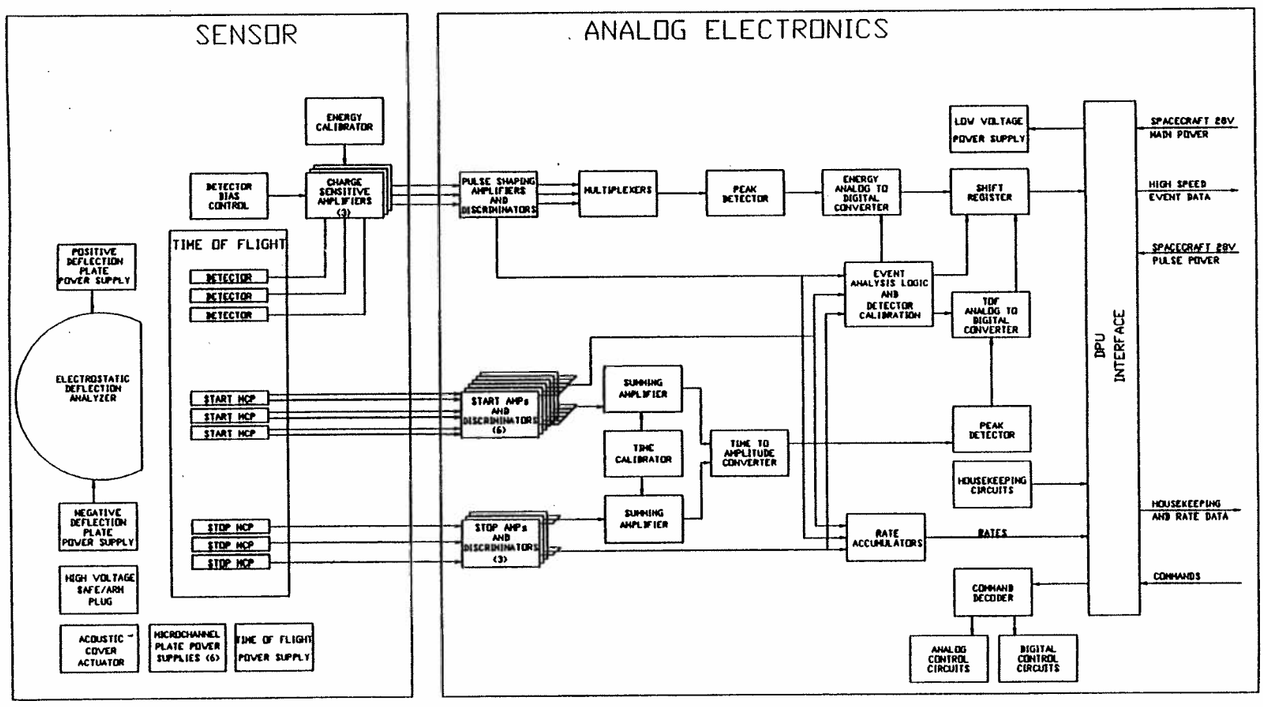

Figure 2.3. A block diagram of the STICS electronics (Gloeckler et al., 1995).

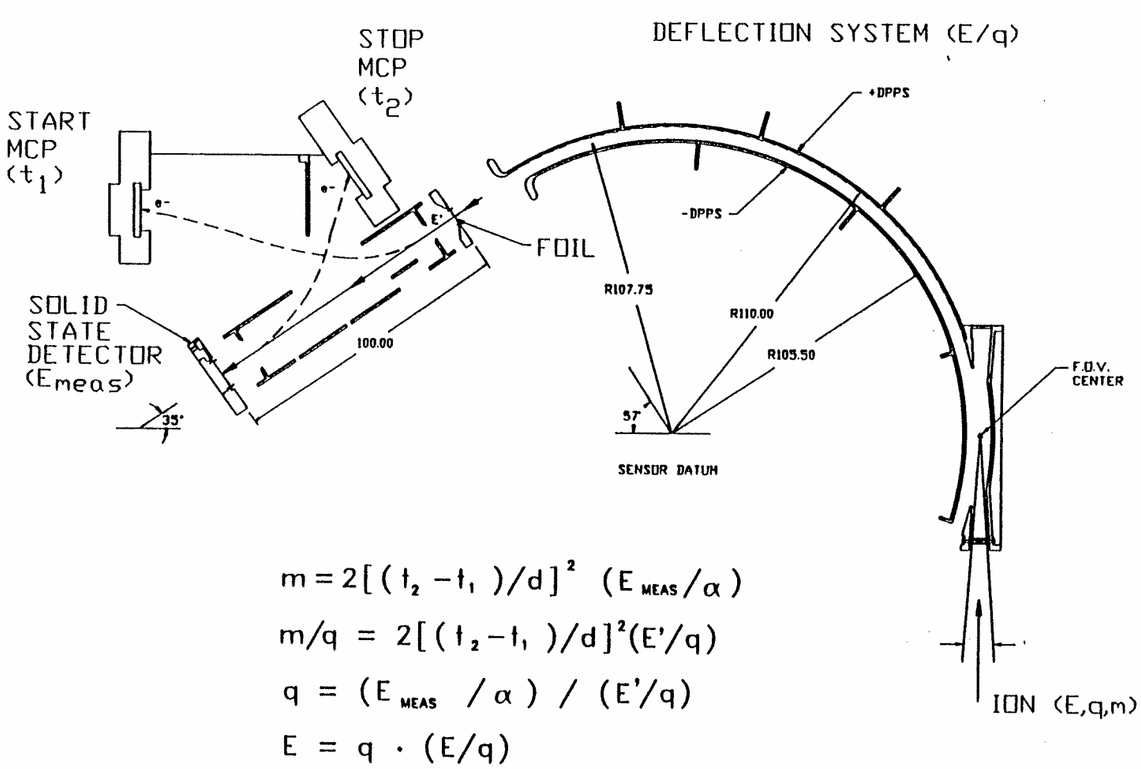

Figure 2.4. A cross-sectional view of the STICS sensor showing its principles of operation. Length measurements are given in millimeters, and angle measurements in degrees.

Only those ions with a specific E/Q determined by the voltage U on the analyzer make it through to the time-of-flight system. A pair of high voltage power supplies step the voltage on the deflection plates once every spin or every two spins depending on the telemetry rate. Thirty-two deflection voltage steps (DVS 0 - 31) are logarithmically spaced to take the plates from a minimum of ±260 volts to a maximum deflection voltage of ±10 kilovolts in order to cover the entire E/Q range of the sensor (6.2-223.1 keV/e). Since STICS became fully operational on December 21, 1994, DVS 2-31 were used for the first sixteen days. From January 6, 1995, onwards, DVS 0-30 (excluding DVS 26) have been used.

After passing through the deflection system, the particles strike a thin (~2μg/cm^2) carbon foil at the entrance of the TOF telescope. As the particles pass through the foil, they knock off secondary electrons, but the particles themselves continue on through the TOF chamber relatively undisturbed. The secondary electrons are detected by the front secondary electron detector assembly (SEDA), which consists of a Start microchannel plate (MCP), two discrete front anodes, and a system of accelerating gaps and deflection electrodes for accelerating and guiding the electrons onto the MCP. This generates a START signal for the TOF analysis. Each front MCP has two anodes, which give additional information on the angle of the ions entering the instrument.

When the particles reach the end of the telescope, they strike a solid-state detector knocking out secondary electrons. These electrons are detected by the rear SEDA creating the STOP signal. If the energy of the particle is greater than the threshold of the solid-state detector, an energy measurement is also obtained.

The TOF system consists of three identical telescopes stacked vertically in the STICS sensor. The middle telescope (2) measures particles in the ecliptic plane within ±26.5°. Telescope 1 looks above the ecliptic from 26.5° to 79.5°, and telescope 3 scans below the ecliptic from -26.5° to -79.5°.

If both a START and a STOP signal (double coincidence) are generated, the time, t, for the particle to travel a known distance (d = 10 cm) can be determined. For triple coincidence must be three signals, the START, STOP, and energy measured (E_{meas}) by the solid-state detector. Along with the E/Q from the deflection system we can calculate the mass (M), ionic charge state (Q), and the incident energy (E) of each ion using the following equations:

$$
\begin{aligned}
M &= 2(t/d)^2(E_{meas}/\gamma) \\
M/Q &= 2(t/d)^2(E'/Q) \qquad (2.1) \\
Q &= (E_{meas}/\gamma)/(E'/Q) \\
E &= Q \bullet (E/Q)
\end{aligned}
$$

E'/Q takes into account the small energy loss of the ions passing through the thin carbon foil, and γ is a number less than one that takes into account the pulse height defect in the solid-state detectors. If the energy of the incident particle is not large enough to trigger the SSD and only t is measured, then only M/Q can be determined, and the mass is colloquially called "mass zero" events. If both E_{meas} and t are obtained, then the mass and M/Q can be calculated.

Besides composition measurements, the particle's direction can be determined. The six discrete Start anodes (two each per Start MCP) provide the polar entrance angle of the incident particle. The polar angle of +79.5° to -79.5° out of the ecliptic is divided into six equal sectors, and each START anode represents one of these polar sectors, nominally 26°. The anodes are labeled from top to bottom: anodes 1 and 2 are in telescope 1, anodes 3 and 4 in telescope 2, and anodes 5 and 6 in telescope 3 (Figure 2.5a). For the azimuthal angle, the DPU uses information from the sector/spin clock of the spacecraft. The spacecraft spin axis is perpendicular to the eclipitic plane, and one complete spin is divided up into sixteen 22.5° azimuthal sectors labelled 0-15. The direction of the sun is typically in azimuthal sector 9 (Figure 2.5b).

(2.5a)

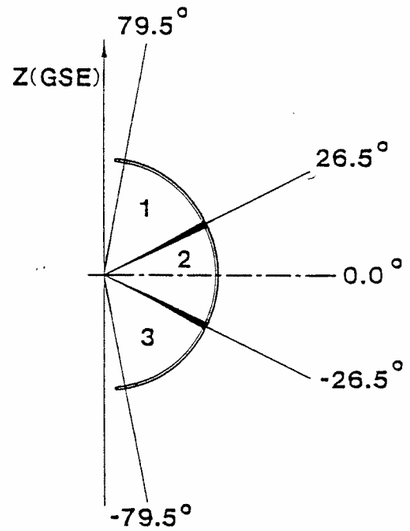

(2.5b)

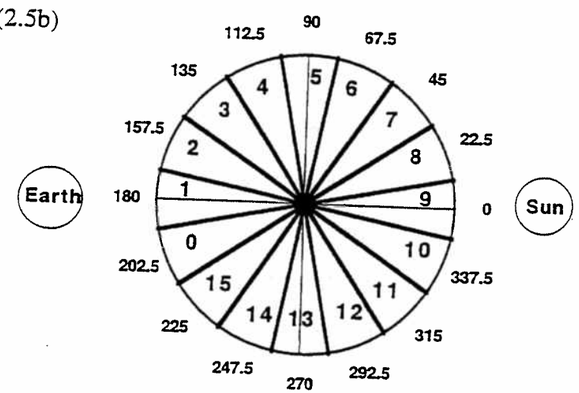

Figure 2.5. (a) STICS polar *look* directions for TOF telescopes 1, 2, and 3. (b) STICS *look* direction in the ecliptic plane consists of sixteen azimuthal sectors (0-15). The view from the north looking downwards shows the spacecraft spinning clockwise. The look angle for the center of each sector is indicated in degrees. Solar wind ions are typically detected in sector 9 of telescope 2.

2.3.2 Angular Apertures

Polar (α) Direction: The nominal polar acceptance angle is 159 ($\pm 79.5°$ from the ecliptic plane). However, certain angular ranges were blocked due to mechanical considerations in assembling the instrument (Figure 2.6). Because the carbon foil used in the time-of-flight chamber is very thin, it had to be mounted in four sections for each telescope leading to three blocked angular ranges per telescope. The effective polar acceptance angle, $\Delta\alpha$, for the entrance aperture of each telescope is about 44.44° with telescope 1, 2, and 3 looking above, in, and below the ecliptic, respectively.

Azimuthal (ß) Direction: Figure 2.7 shows a cross-sectional view of the entrance aperture. Only the particles entering from +2.6° to -2.2° of the center line are focused to the center field of view (FOV) where they are then channeled into the deflection system.

The effective area of the physical opening, through which particles can be detected, has an azimuthal acceptance angle, $\Delta ß = 4.8°$ and radius, $r = 3.594$ cm. Therefore, the area of the entrance aperture, A_e, for each telescope is as follows:

$$A_e = r^2 \Delta\alpha \Delta ß$$

$$A_{e1} = A_{e2} = A_{e3} = 0.84 \text{ cm}^2 \qquad (2.2)$$

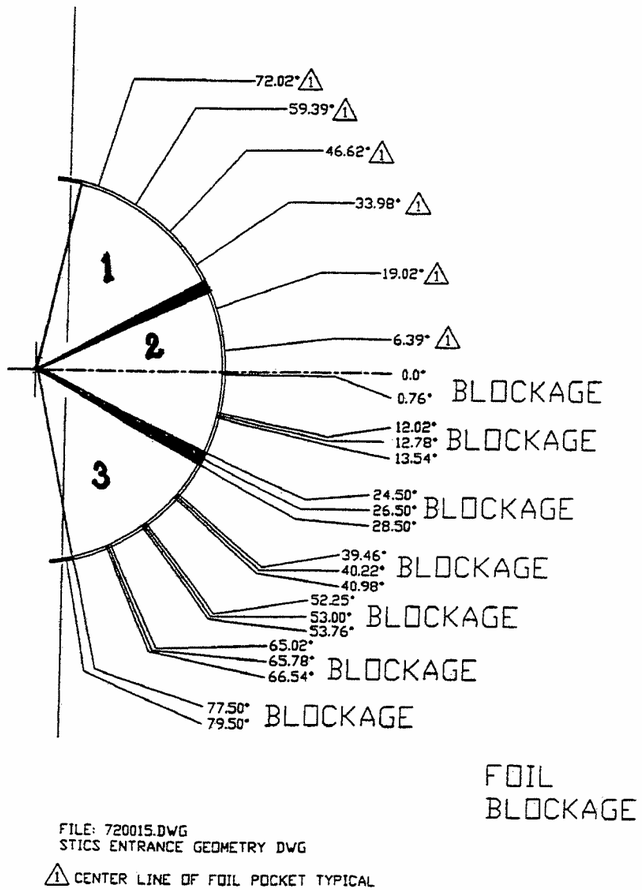

Figure 2.6. Physical blockages result in a reduced polar acceptance angle for telescopes 1, 2 and 3.

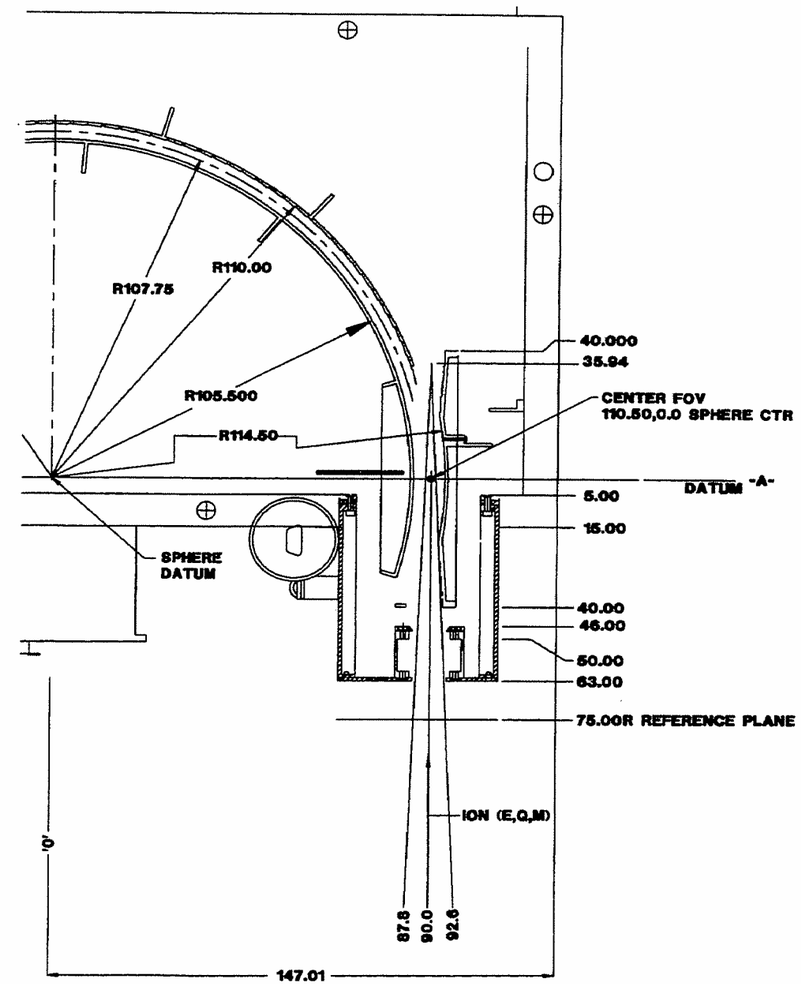

Figure 2.7. A cross-sectional view of the entrance aperture showing the azimuthal acceptance angle.

2.4 Telemetry

The spacecraft transmits data back to Earth at two different telemetry rates: high bit rate (HBR) and low bit rate (LBR). In high bit rate the STICS telemetry allocation is 720 bits per second and in low bit rate, 360 bits per second . When WIND is in the near Earth region, the telemetry is sent at high bit rate. As the spacecraft moves away from Earth in interplanetary space, the data are transmitted at low bit rate. The telemetry received from the spacecraft consists of Housekeeping (HK) Data, Direct Sensor Rates, Science Rates, and Pulse Height Analyzed (PHA) Words. In high bit rate, the STICS deflection voltage is held constant for one spin (~3 secs) and in low bit rate, for two spins (~6 secs) . All STICS counting rates are given in terms of counts at each voltage step. A detailed description of the STICS telemetry can be found in the DPU document (Gerlach and Wiewesiek, 1994).

2.4.1 Housekeeping Data

This data basically contains information on the operating status of the instrument. For example, the ON/OFF status of the power supplies, the deflection voltage step number, the SSD threshold levels, the MCP levels, compression codes, trigger modes, etc., are all part of the housekeeping data. The current and voltage of all power supplies can also be found in the HK data.

2.4.2 Direct Sensor Rates

These rates are read from the different counters in the time-of-flight section for each telescope, e.g., the front SEDA rates (FSR's), the rear SEDA rates (RSR's), the solid-state detector rates (SSD's), the double coincidence rates (DCR's), the triple coincidence rates (TCR's), etc. The FSR is the most sensitive rate, and it is our best indicator for when a particle event has occurred.

2.4.3 Science Rates

The M-M/Q space is divided-up into three different regions, Range 0, 1 and 2. The Basic Rates (BR0, BR1 and BR2) count the total number of particles in each Range (R0, R1 and R2, respectively). Within these regions there are pre-defined boxes (see Figure 2.8) representing charge states of different elements, e.g., H^+, He^+, He^{2+}, O^+, O^{6+}, O^{7+}, Fe^{8+}, Fe^{9+}, Fe^{10+}, etc. The He^{2+} rate is the High-resolution Matrix Rate (HMR) which contains full directional information (6 polar sectors x 16 equatorial sectors). The medium-resolution Sectored Matrix Rate (SMR) contains only partial directional information (3 polar x 8 equatorial sectors). The H^+ rate is the SMR. There are twenty Omnidirectional Matrix Rates (OMR0-19) which are accumulated over all polar and equatorial sectors and contain no directional information. Table 2.2 gives a list of all the science rates along with their boundaries in M-M/Q space as currently defined in the DPU. The H^+, He^+, and He^{2+} rates all include both triple coincidence and double coincidence data ("mass zero (mz)" events), whereas OMR1-19 contain only triple coincidence data. The rate boundaries are changeable by command.

2.4.4 PHA Words

The analog electronics generates an Event Word for every detected particle and sends it to the DPU. The Event Word contains the measured time-of-flight, measured energy and detector/telescope identification. All Event Words are classified by the DPU for placement into Basic Rate bins and possible placement into other Science Rate bins. In addition, a limited number of Event Words are selected by the DPU for formatting into the STICS PHA Words. Each PHA word consists of the STOP MCP identification, START and Range identification, the measured energy channel number, azimuthal sector number, SSD number, and time-of-flight channel number. The

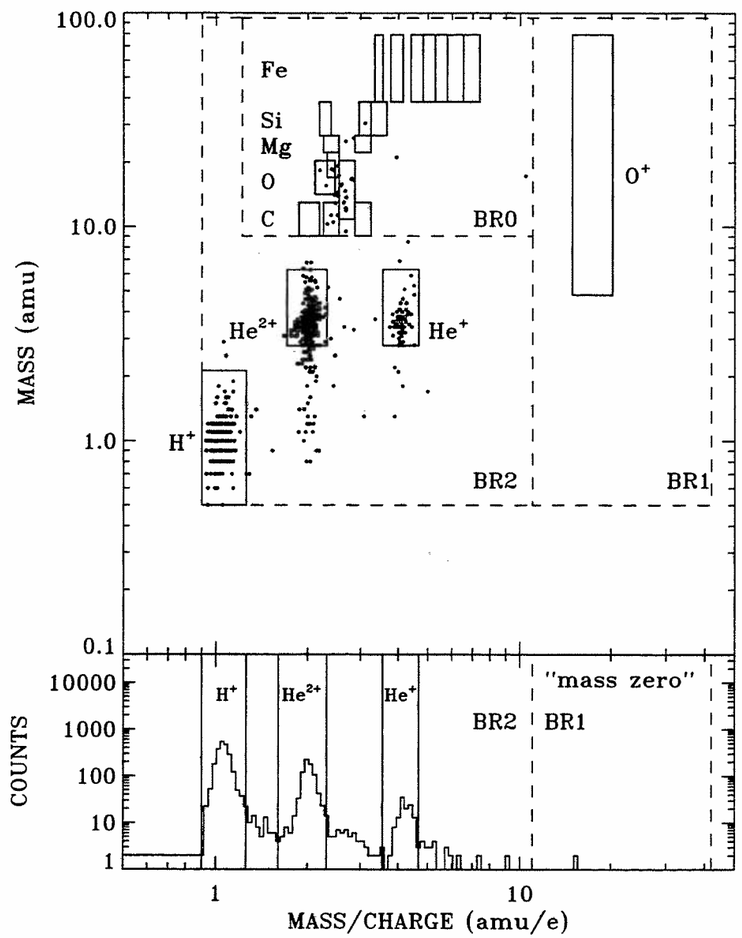

Figure 2.8. Raw PHA data plotted in M-M/Q space for April 7, 1995 15:00-20:00 UT from the out-of-ecliptic telescopes (1 and 3) when WIND was in interplanetary space ~223 R_e upstream of the Earth. The Basic Rate and Matrix Rate boundaries are shown. The horizontal "stripes" in the H^+ box appears because the mass values are rounded-off to 1 decimal place. The size of the boxes give an indication of the allowable spread in the data.

Table 2.2 Default Matrix Rate definitions in M-M/Q space as defined in the DPU.

Rate Designation	Species	Mass Range (amu)	M/Q range (amu/e)
HMR	$^*He^{2+}$	2.79-6.30	1.71-2.32
		mz†	1.61-2.32
SMR	H^+	mz† - 2.13	0.90-1.26
OMR0	$^*He^+$	2.79-6.30, mz	3.55-4.67
OMR1	C^{6+}	9.04-12.99	1.87-2.18
OMR2	C^{5+}	9.04-12.99	2.25-2.54
OMR3	C^{4+}	9.04-12.99	2.87-3.24
OMR4	O^{7+}	14.21-20.41	2.11-2.46
OMR5	O^{6+}	10.83-20.41	2.54-2.87
OMR6	O^+	4.80-79.30	14.89-20.20
OMR7	Ne^{8+}	17.03-22.34	2.32-2.54
OMR8	Mg^{10+}	22.34-26.77	2.25-2.54
OMR9	Mg^{8+}	22.34-26.77	2.87-3.24
OMR10	Si^{12+}	26.77-38.44	2.18-2.39
OMR11	Si^{9+}	26.77-38.44	2.96-3.24
OMR12	Si^{8+}	26.77-38.44	3.24-3.66
OMR13	Fe^{16+}	38.45-79.28	3.34-3.55
OMR14	Fe^{14+}	38.45-79.28	3.77-4.14
OMR15	Fe^{12+}	38.45-79.28	4.40-4.82
OMR16	Fe^{11+}	38.45-79.28	4.82-5.28
OMR17	Fe^{10+}	38.45-79.28	5.28-5.78
OMR18	Fe^{9+}	38.45-79.28	5.78-6.53
OMR19	Fe^{8+}	38.45-79.28	6.53-7.38

*See Table 3.2 for revised helium M and M/Q boundaries in ground-based PHA analysis. †Mass zero (mz) or double coincidence events.

energy and time information given in the PHA word is the same as that in the Event word, except that the energy is compressed to 9 bits in the PHA word.

The Start anodes are used to define the incident polar direction of each particle (see section 2.3.1). There are 10 START states which identify the anode that fired. States 1-6 indicate which single front anode fired. State 7 indicate a simultaneous firing by anodes 1 and 2, state 8 simultaneous firing by anodes 3 and 4, and state 9 simultaneous firing by anodes 5 and 6. State 0 means that no anode fired. The START state and Range of a particle are combined into one number (ID) using the following relation:

$$ID = START*3 + Range \qquad (2.3)$$

where START = 0-9 and Range = 0-2. This gives the following Truth Table (2.3) for ID:

Table 2.3. Truth table for the ID states of the the combined START and Range values stored in the PHA words. States 30 and 31 are undefined.

Range	START 0	1	2	3	4	5	6	7	8	9
0	0	3	6	9	12	15	18	21	24	27
1	1	4	7	10	13	16	19	22	25	28
2	2	5	8	11	14	17	20	23	26	29

Because of the limited telemetry, the DPU cannot send every Event Word down as a PHA word. Hence the Event Words are prioritized and a limited number that meet pre-defined criteria are incorporated into the telemetry. STICS is allotted 22 PHA words for the duration of each voltage step (one spin in high bit rate, and two spins in low bit rate). If there are 22 particles or fewer detected during one voltage step, then all the corresponding PHA words are transmitted by the DPU to the spacecraft

telemetry. In this case unused STICS PHA slots are assigned to SWICS or MASS, otherwise the slots are filled with zeros. If there are more than 22 particles detected during one voltage step, then an attempt is made to sample all azimuthal directions and all ranges with Range 0 having highest priority and Range 2, lowest. There are 8 PHA slots for Range 0, and 7 each for Ranges 1 and 2. Any spare slots in any Range are allotted according to range priority.

2.5 Summary

The STICS instrument uses electrostatic deflection, followed by a time-of-flight measurement, and an energy measurement with a solid state detector to determine the mass, mass-per-charge, and energy of ions from H - Fe in the energy-per-charge range of 6.2 - 223.1 keV/e. In flight, the electrostatic deflection voltage is stepped in 30 logarithmically spaced steps covering 6.2-198.8 keV/e. The arrival directions of the ions can also be obtained. There are six polar sectors covering ±79.5° relative to the ecliptic plane, and sixteen azimuthal sectors covering 360°.

The STICS telemetry consists of Housekeeping Data, Direct Sensor Rates, Science Rates, and Pulse Height Analyzed (PHA) Words. The Housekeeping Data contain information on the operating status of the instrument, and the Direct Sensor Rates are read from the different counters in the time-of-flight section. Each Science Rate gives the number of counts falling within a specified range of mass and mass-per-charge values representing a given ion (H^+, He^{2+}, He^+, O^{6+}, etc.) or range of ions. All STICS counting rates are given in terms of counts per deflection voltage step. The PHA words contain the measured energy, measured flight time, and directional information for each detected ion. STICS is allotted 22 PHA words per voltage step.

CHAPTER 3: DATA ANALYSIS

In this chapter, the algorithms used in extracting the mass and mass-per-charge information from the STICS science telemetry data are first given in Section 3.1. The number of measured counts for a given ion at a given energy-per-charge channel can be converted to differential flux or distribution function using the instrument response function in order to get an energy spectrum or velocity distribution, respectively. The different factors that make-up the instrument response function are explained in Section 3.2. The method used to bin the data and the equations used to calculate the differential flux and distribution function are discussed in Section 3.3 and 3.4. A summary of the information is presented in the last section.

3.1 Data Extraction

The STICS data basically consists of Matrix Rates and pulse height analyzed (PHA) data for each deflection voltage step (DVS) or equivalently each energy-per-charge (E/Q) channel, (see section 2.4). Only two of the Matrix Rates (H^+ and He^{2+}) contain directional information, whereas the rates for the other ions are averaged over all directions by the data processing unit (DPU). The Matrix Rate for each ion keeps track of all the counts detected by STICS that fall into pre-defined boxes in M-M/Q space. On the other hand, the PHA data have full information for each detected particle: the energy channel number, the time-of-flight channel number, both azimuthal and polar directions. However, the number of PHA words may be less than the number of detected particles. Because of the limited telemetry, STICS is only allowed 22 PHA words per DVS. When the number of particles exceeds 22 for any DVS, the data are normalized by the Basic Rates to take this into account (see Section 3.2.2).

The PHA data is preferred over the Matrix Rates when studying STICS data in-depth because they contain all the information for each particle, and they are less

susceptible to being corrupted during transmission from the spacecraft to the Earth (telemetry hits). With the PHA data, the ion identification is not limited to the pre-defined Matrix Rate M-M/Q boxes as defined in the DPU. New box definitions may be created and old ones redefined to classify ions as needed. More thorough checks can be made on the PHA data to ensure that they are not corrupted.

Each STICS PHA word is stored in 4 bytes (32 bits) of telemetry. The time-of-flight channel number, the solid-state detector (SSD) identification, the azimuthal sector, the compressed energy channel number, the Start anode identification and Range combined into ID (see equation 2.3 and Table 2.2), and the Stop MCP identification. The Start anode and Range information can be separated using the following equation:

$$\text{START} = \text{ID}/3 \qquad \{\text{integer division}\}$$

$$\text{Range} = \text{ID} - 3*\text{START} \tag{3.1}$$

The time-of-flight channel number, T_{ch}, is converted to time, τ, in nanosecond (ns) using the following relation as determined from pulser calibrations (see Appendix A.3):

$$\tau\,\{\text{ns}\} = [T_{ch} - 44]/2.372530695 \tag{3.2}$$

The compressed energy channel number, E_c, is first decompressed to E_d using

$$\begin{aligned} E_d &= E_c && \text{for } E_c < 256 \\ E_d &= 2E_c - 256 && \text{for } 256 \le E_c < 384 \\ E_d &= 4E_c - 1024 && \text{for } 384 \le E_c < 1024 \end{aligned} \tag{3.3}$$

Then E_d is converted to the measured energy, E_{meas}, in units of kiloelectronvolts (keV) using the following equation:

$$E_{meas}\,\{\text{keV}\} = [E_d + 6]/0.37654782 \tag{3.4}$$

The energy-per-charge can be determined using:

$$E/Q\,\{\text{keV/e}\} = 6.190722 * (1.1225857)^{DVS} \tag{3.5}$$

The mass-per-charge and mass are calculated using the following algorithms

$$M/Q\,\{\text{amu/e}\} = 1.9159\text{E-}05 * [E/Q - C_1] * \tau^2 \tag{3.6}$$

where $C_1 = 1.5$ for $M/Q < 11$ and $C_1 = 2.5$ for $M/Q \geq 11$, and

$$\ln(M) = A_1 + A_2*X + A_3*Y + A_4*XY + A_5*X^2 + A_6*Y^3 \quad (3.7)$$

where $A_1 = 2.69575$, $A_2 = -0.843766$, $A_3 = -2.38009$, $A_4 = 0.385641$, $A_5 = 0.0513127$, $A_6 = 0.0690096$, $X = \ln(E_{meas})$, and $Y = \ln(\tau)$. If $E_{meas} < E_{min} = 21$ keV, then $M = 0$, commonly called "mass zero" events since the M/Q can still be determined from the time of flight.

The M-M/Q space is subdivided into 58 mass bins (N_m) and 126 mass-per-charge bins (N_q) that are logarithmically spaced between the minimum and maximum values. The boundaries of the N_m bins are defined by the following relations:

Mass Range {amu} = 0.5 - 95.0

N_m Range = 1 - 58

$k_m = (95.0/0.5)^{1/58}$

$$M \{\text{lower bound of } N_m \text{ in amu}\} = 0.5 * k_m^{(N_m - 1)} \quad (3.8)$$

For the "mass zero" events, $N_m = 0$. Similarly, the boundaries of the N_q bins are defined as follows:

Mass/Charge Range {amu/e} = 0.9 - 42.0

N_q Range = 1 - 126

$k_q = (42.0/0.9)^{1/126}$

$$M/Q \{\text{lower bound of } N_q \text{ in amu/e}\} = 0.9 * k_q^{(N_q - 1)} \quad (3.9)$$

Classifying the ions into these small N_m-N_q bins is extremely useful when studying charge states. For example, for ^{56}Fe ions at energy 78 keV, charge state 9+ will enter during DVS 3, whereas charge state 10+ will enter during DVS 2.

3.2 Instrument Response Function

After identifying the element and its charge state from the PHA data, further analysis may involve calculating the distribution function, f(v), over a given time period. In order to do so, the instrument response function must be applied to the accumulated raw counts. The instrument response functions includes the Duty Cycle and Deadtime Correction, the Basic Rate Normalization to the PHA data, the Box Efficiency in M-M/Q space, Geometric Factor, the time-of-flight telescopes efficiencies, and the Energy Passbands.

3.2.1 Duty Cycle and Deadtime Corrections

Duty Cycle (or Accumulation Deadtime): Nominally, the spacecraft spin rate is one rotation every 3 seconds. Since each spin is divided into sixteen azimuthal sectors, the accumulation time for each sector is 187.5 ms. At the beginning of each of sectors 1-15, there is a deadtime in the DPU of 12 ms during which no STICS data are accumulated. This time is allotted to the DPU for various functions, including reading the different counters and classifying the data for each sector. The deadtime for sector 0 is 100 ms in order to avoid accumulating data while the deflection voltage step is changing at the beginning of this sector, a transition which takes about 50 ms. Even when the deflection voltage step is held constant for two consecutive spins (during low bit rate), sector 0 maintains the 100 ms deadtime for convenience in the DPU programming. The overall deadtime is 0.28 sec for each spin. The deadtime correction is a factor (Table 3.1) by which the accumulated counts for a given sector are multiplied in order to compensate for the time the instrument is not collecting data. For example, the correction factor for sector 0 is given by 187.5/(187.5 - 100) = 2.143.

Table 3.1. Accumulation deadtime corrections factors.

	Deadtime Correction
Sector 0	2.143
Sector 1,...,15	1.068
Entire Spin	1.103

Electronic Deadtime Correction: The Electronic Deadtime can be at two levels: sensor electronics and DPU classification. At the sensor level, the MCP can saturate if the incident flux is too high. A cloud of electrons from more than one particle hits the MCP, but the MCP cannot tell that the cloud came from several particles, so it counts it as "one" event. The time signal uses "fast electronics", but there is an "analysis window (~409 ns)", and if another particle comes in during that window, it will not get measured for a PHA event. The energy pulse height measurement is slowed-up by the analysis time (~20 μs) of the current in the SSD. If another particle enters while the energy from the first is being measured, it may not be detected as a separate event. These effects occur at the sensor level and would affect the Direct Sensor Rates.

At the DPU level, the PHA event words are classified by the DPU using fast look-up table techniques to establish a relation between the energy and time-of-flight. When the incident flux of particles becomes too great, not all the particles are processed. The DPU look-up time is not relevant to the Direct Sensor Rates, only to the Science Rates (Basic Rates and Matrix Rates). Therefore, the Science Rates begin to saturate before the Direct Sensor Rates. When a counting rate (Direct Sensor or Science rate) begins to saturate, there is no longer a linear relation between the incident flux and the rate (see Section A.2). For the first three years of the WIND mission, the particle intensities encountered both in the magnetosphere and in interplanetary were not large enough to make the electronic deadtime significant.

3.2.2 Basic Rate Normalization

As previously discussed (section 2.4.4), not all the PHA Words may have been transmitted because of the limited telemetry. To get around this problem, the Basic Rates are used for normalization. There are three Basic Rates (BR0, BR1, and BR2) that count the total number of particles in each of the respective Ranges (Range 0, 1, and 2). For STICS, each Basic Rate is sectored into eight bins. Bin 1 counts all the particles accumulated in azimuthal sectors 0 and 1 for all three telescopes combined, bin 2 counts all the particles accumulated in azimuthal sectors 2 and 3 for all three telescopes combined, bin 3 counts all the particles in azimuthal sectors 4 and 5 for all three telescopes, etc. The Range of each particle is contained in the PHA word. All the PHA words for a given spin can be grouped according to their assigned Ranges into PHA0, PHA1, and PHA2 over the same sectors and all telescopes combined as the corresponding Basic Rate sectored bin. Each PHA group is a selected subset of the events counted by the Basic Rates. The Basic Rate Normalization is performed by multiplying the number of measured counts in a given sector by the corresponding weighting factor $[BRi_{norm} = BRi/PHAi]_{sector}$ where i = 0, 1, or 2.

When the spacecraft is in interplanetary space upstream of the Earth's bow shock, the number of particles detected by the instrument is typically less than 22 for each DVS. However, in the near Earth region (magnetosheath and magnetosphere), the number is usually greater than 22 making the Basic Rate normalization of the PHA data more important in that region.

3.2.3 Box Efficiency

Sometimes all the counts for a given ion may not fall into its pre-defined box in M-M/Q space (see Figure 3.1). Or, boxes that are close together, e.g., the Fe charge state bins, may have counts spilling over into neighboring boxes. The Box Efficiency must be determined and used to correct for the number of measured counts. The ions

examined in this dissertation are H^+, He^{2+}, and He^+. Upon examining flight data, about 8% of the H^+ raw counts fall outside its box causing its efficiency to be ~92%.

The He^+ and He^{2+} boxes were increased because the original ones missed about 10% of the counts. The original He boxes, which are still used by the DPU, do a good job in that they are centered on the two peaks, and the bulk of the counts for both the "mass zero" and triple coincidence events are obtained. However, they clearly do not contain all the He triple coincidence events, as can be seen from the M-M/Q plot (Figure 3.1). The new He boxes, shown as dashed lines drawn around the old ones, are about 98% efficient.

When the solar wind speed rises above 600 km/s during high speed streams, the tails of the solar wind ion spectra are measured by the lower energy-per-charge steps mainly as "mass zero" events in telescope 2 (middle). The mass-per-charge range of the He^{2+} box is reduced for DVS 0-8 to decrease the number of heavy ions spilling into this box (see Table 3.2 and Figure 3.1). The fraction of energy lost by the ions in passing through the carbon foil at the entrance of the time-of-flight is greater for the lower energy ions resulting in lower mass and mass-per-charge resolution. This means that the box efficiency for the lower energy ions would be slightly less.

Table 3.2. Box definition and efficiency for H^+, He^+ and He^{2+}.

Ion	Mass Range (amu)	Mass/Charge Range (amu/e)	Box Efficiency
H^+	mz-2.13	0.90-1.26	0.90 for DVS < 15 0.99 for DVS ≥ 15
He^+	1.77-6.89#, mz	3.55-4.67	0.98
He^{+2}	1.77-6.89# mz	1.71-2.32 1.61-2.32 (1.61-2.11)*	0.98

*Only used for events measured by telescope 2 DVS 0-8 during high-speed streams.
#Values different from those used by the on board DPU given in Table 2.3.

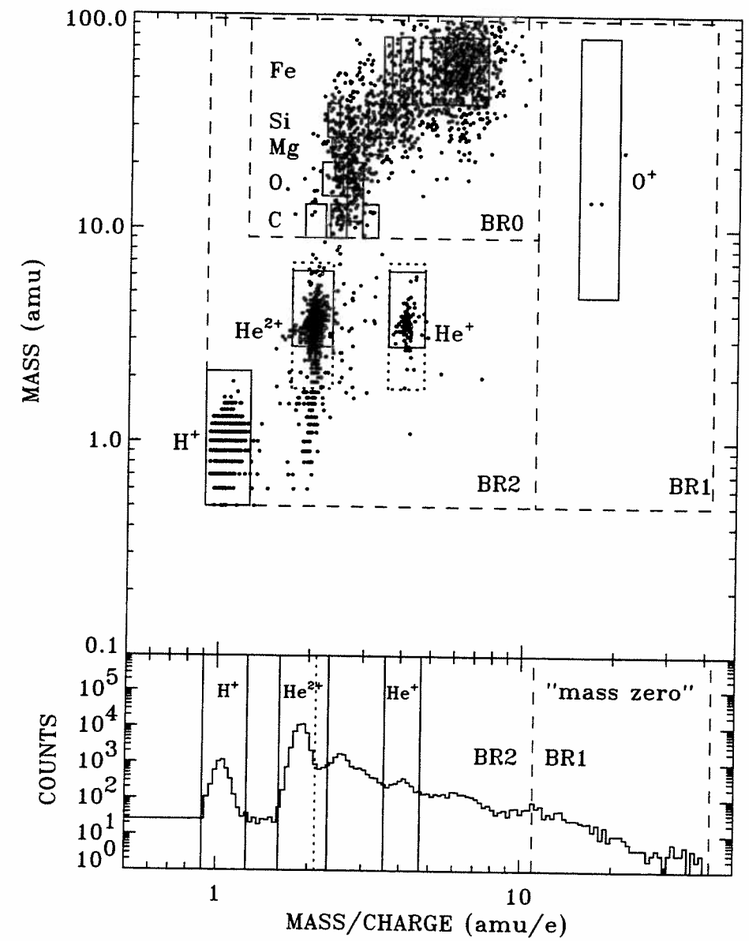

Figure 3.1. A plot of the M-M/Q PHA data is shown for the period May 30, 1995, 10:00 - 22:30 UT during a CIR event. The new triple coincidence He^+ and He^{2+} boxes are indicated by dashed lines around the old boxes. The dashed lines in the "mass zero" He^{2+} box shows the reduced box used for DVS 0-8 when measuring solar wind ions with telescope 2.

3.2.4 Geometric Factor

The Geometric Factor relates the instrument's counting rate to the flux of the incident radiation and is solely dependent on the dimensions of the aperture and the sensitive area of the detector system. Consider the case of an ideal telescope, whose efficiency for detecting particles is 100%, measuring an isotropic particle distribution with absolute intensity I (units of counts sec^{-1} cm^{-2} sr^{-1}). The counting rate, C with units of counts sec^{-1}, is given by

$$C = \int_{\Omega}\int_{A} (\cos\theta * dA)\, d\Omega\, I$$

Since I is isotropic, then

$$C = Ig$$

and

$$g = \int_{\Omega}\int_{A} (\cos\theta * dA)\, d\Omega \qquad (3.10)$$

where g is the isotropic Geometric Factor, θ is the angle between the incident radiation and the normal to the element of area dA, $d\Omega$ is the element of solid angle, and A represents the domain of dA (Gloeckler, 1970). If the area, A, of the detection surface is normal to the incident flux, then equation (3.10) becomes

$$g = A^{*}\Delta\Omega \qquad (3.11)$$

where $\Delta\Omega$ is the effective solid angle subtended by the aperture.

For a parallel beam of particles incident perpendicular to the aperture (e.g., the solar wind), there is no angular dependence, and in this case the Geometric Factor, G, is simply given by

$$G = A \qquad (3.12)$$

With the STICS sensor, this area is the effective area of the carbon foil, A_C, through which the particles pass.

From the pre-flight calibration data and inflight cross-calibrations (Appendix A.4) with WIND-SMS-MASS at the lower end of the STICS energy range and with WIND-EPACT-STEP at the higher end, the geometric factors for each telescope are as follows:

Table 3.3. Geometric factors determined from pre-flight and inflight calibrations.

Telescope	Parallel Beam Geometric Factor, G_i, {cm^2}	Isotropic Geometric Factor, g_i, {cm^2 sr}
1	0.72 ± 0.18	0.031 ± 0.002
2	0.68 ± 0.18	0.029 ± 0.002
3	0.74 ± 0.18	0.029 ± 0.002

3.2.5 TOF Telescope Efficiencies

As particles travel through the instrument, some get lost in the deflection system, some do not pass through the carbon foil at the entrance of the time-of-flight (TOF) telescope, and some are not detected when the reach the end of the TOF chamber. The TOF telescope efficiencies are given in two parts, the Start (η_1) and Stop (η_2) efficiencies. They are defined as follows:

$$\eta_1 = \frac{FSR}{CFR} = \frac{DCR}{RSR} \qquad (3.13)$$

$$\eta_{2a} = \frac{DCR}{FSR} \qquad \eta_{2b} = \frac{TCR}{FSR} \qquad (3.14)$$

where the Carbon Foil Rate (CFR) is the rate at which the particles pass through the carbon foil, FSR is the Front SEDA Rate (where SEDA stands for secondary electron

detector assembly as explained in Section 2.3.1), RSR is the Rear SEDA Rate, DCR is the Double Coincidence (time signal obtained) Rate, and TCR is the Triple Coincidence (both time and energy measurements made) Rate. There is no direct sensor reading for CFR so the Start efficiency will be determined by DCR/RSR. Since triple coincidence (mass and mass/charge measured) results in more accurate identification of particles, TCR/FSR would be used for the Stop efficiency. But in the case when there is no energy measurement, i.e., only DCR, then the DCR/FSR would be used. The DCR/FSR Stop Efficiencies are used for H^+, He^{2+}, and He^+ because all three ion boxes include the "mass zero" events. Figure 3.2 shows the smoothed TOF efficiencies curves for the calibrated ions (see Appendix A.2.4).

3.2.6 Energy Passband (ΔE/Q)

When the deflection voltage is at a given value, the spherical deflection system will allow only those particles with a specific E/Q value to enter the instrument. However, there is some allowable spread in these E/Q values. From calibration data (see Appendix A.2.3), the average E/Q passband, $\frac{\Delta(E/Q)}{E/Q}$, was found to be 1.9% (FWHM) of the central energy, which is about 2.5 times less than the design goal of 5%.

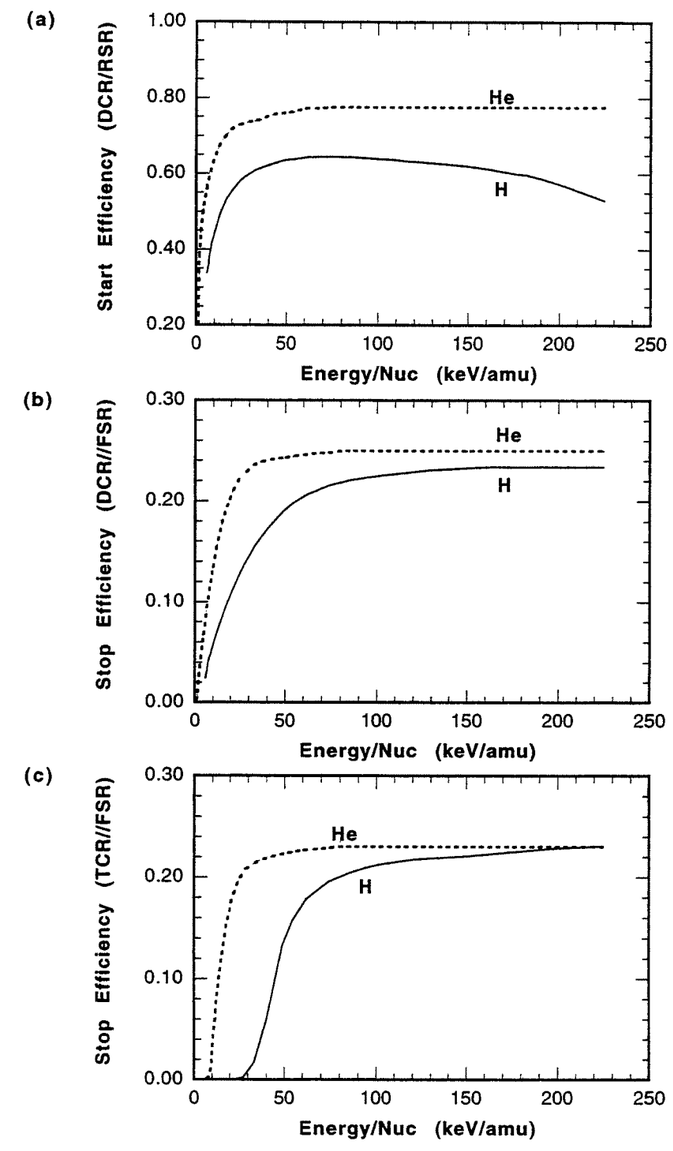

Figure 3.2. Smoothed H and He TOF efficiency curves.

3.3 Binning the Data

The STICS instrument selects ions by energy-per-charge (E/Q) using electrostatic deflection. There are 32 deflection voltage steps (DVS 0-31) that are logarithmically spaced from 6.19-223.12 keV/e with a passband of 1.9% (FWHM) of the mean E/Q value (see Table 3.4). Therefore, the data are naturally binned by E/Q. After identifying the mass and charge of the ions, the bins can be converted to E/M using

$$E/M\ \{keV/amu\} = E/Q\ *\ Q/M \tag{3.15}$$

Since the lower end of the STICS E/Q range may include the tail of the solar wind ion spectra, it is sometimes necessary to bin the data by V_{ion}/V_{sw} where V_{ion} is the ion speed and V_{sw} the solar wind bulk speed. The normalized velocity bins are also logarithmically spaced such that there is a one-to-one mapping from E/Q to V_{ion}/V_{sw}. The velocity bin number, VBN, for each ion at each DVS is given by

$$V_{ion}\ \{km/s\} = 437.74\sqrt{E/M} \tag{3.16}$$

$$VBN = \text{integer}\left[\frac{\log_{10}(V_{ion}/V_{sw})}{VBS}\right] \tag{3.17}$$

where VBS = 0.025 is the logarithmic size of the bins.

3.4 Differential Flux and Distribution Function

If *dN* is the number of particles passing through an area element *dA* at location **r** made over the time interval *t* and *t* + *dt* with energy between *E* and *E* + *dE* whose direction of incidence is within the solid angle cone *dΩ*, then the differential flux, *dJ/dE*, is defined by

$$dN = \frac{dJ}{dE} dA\ dE\ d\Omega\ dt \tag{3.18}$$

The distribution function, *f*, is defined as the number of particles, *dN*, in an infinitesimal coordinate-space volume (***r*** to ***r*** + ***dr***) and an infinitesimal velocity-space volume (***v*** to ***v*** + ***dv***) at a time *t*, i.e.,

$$f = \frac{dN}{d^3r\ d^3v} \tag{3.19}$$

Table 3.4. The corresponding energy-per-charge and passband for each deflection voltage step. The E/Q value is obtained from equation 3.5 and the passband (FWHM) is 0.019E/Q.

DVS	E/Q {keV/e}	ΔE/Q {keV/e}
0	6.19	0.12
1	6.95	0.14
2	7.80	0.16
3	8.76	0.18
4	9.83	0.20
5	11.04	0.22
6	12.39	0.25
7	13.91	0.28
8	15.61	0.31
9	17.53	0.35
10	19.68	0.39
11	22.09	0.44
12	24.80	0.50
13	27.84	0.56
14	31.25	0.62
15	35.08	0.70
16	39.38	0.79
17	44.21	0.88
18	49.62	0.99
19	55.71	1.11
20	62.54	1.25
21	70.20	1.40
22	78.81	1.58
23	88.47	1.77
24	99.31	1.99
25	111.49	2.23
26	125.16	2.50
27	140.50	2.81
28	157.72	3.15
29	177.05	3.54
30	198.76	3.98
31	223.12	4.46

From equations 3.18 and 3.19, and using $dv^3 = v^2\, dv\, d\Omega$ and $dr^3 = dt\, A\, v$, it follows that

$$\frac{dJ}{dE} dA\, dE\, d\Omega\, dt = f\, d^3r\, d^3v = f\, v^2\, dv\, d\Omega\; v\, dt\, dA$$

$$\Rightarrow\; f = \frac{m^2}{2E}\frac{dJ}{dE} \qquad (3.20)$$

where we used $E = 0.5mv^2$ and $dE = mvdv$. Equation 3.20 is only true for non-relativistic particles, and is appropriate for the STICS energy range. The differential flux for STICS at any given energy E is

$$\frac{dJ}{dE} = \frac{\text{counts}}{g\, \Delta E\, \eta_1\, \eta_2\, \Delta t}\frac{DC \times BR_{norm}}{Box_{eff}} \qquad (3.21)$$

where g is the geometric factor, ΔE the energy passband, η_1 and η_2 the TOF efficiencies, Δt the accumulation time, DC the deadtime correction factor, BR_{norm} the Basic Rate Normalization, and Box_{eff} the box efficiency. The units of dJ/dE is $[cm^2\ s\ sr\ keV/amu]^{-1}$. With m measured in units of amu and E in keV along with the units of dJ/dE, the units of f can be converted to s^3/km^6 by multiplying the right hand side of equation 3.20 by 1.076, i.e.,

$$f\,\{s^3 / km^6\} = 1.076\, \frac{m^2}{2E}\frac{dJ}{dE} \qquad (3.22)$$

For an omni-directional distribution, the accumulation time, Δt, per spin is ~3.0 s and the and the isotropic geometric factor, g, is used. However, when measuring the uni-directional solar wind distribution, the parallel beam geometric factor, G, is used, and the time per spin when the instrument observes the parallel beam solar wind is given by

$$\Delta t\,\{s\} = \frac{3^o}{360^o} \times \text{Spin Period} \qquad (3.23)$$

where 3° is the effective azimuthal acceptance angle of the instrument (Appendix A.2.2), and the spacecraft spin period is ~3.0 s.

3.5 Summary

The PHA data are preferred over the Matrix Rates because the PHA words contain all the information on the detected particles, and more thorough checks can be made on the PHA data to ensure that the data are valid. The mass and mass-per-charge can be obtained from the measured time and energy channel numbers using equations 3.2 - 3.7. Since STICS uses electrostatic deflection, the incident ions are naturally selected and binned by their energy-per-charge. The energy-per-charge bins can be easily converted to energy-per-nucleon or, equivalently, velocity bins. The differential flux and distribution function of a given ion can be determined by applying the instrument response function (Table 3.5) to the measured counts as seen equations 3.21 and 3.22.

Table 3.5. Summary of instrument response function parameters.

Instrument Response Function	
Accumulation Deadtime: Sector 0 Sector 1,...,15 Entire Spin	Correction Factor 2.143 1.068 1.103
Basic Rate Normalization	$[BRi_{norm} = BRi/PHAi]_{sector}$ Range, i, = 0, 1, or 2.
Box Efficiency	See Table 3.2
Energy-per-charge Passband $\Delta(E/Q)$ [FWHM]	$(0.019 \pm 0.001)E/Q$
Geometrical Factor: Isotropic: $g_{1,2,3}$ Parallel Beam, G_2	 0.031, 0.029, 0.029 ± 0.002 cm^2 sr 0.68 ± 0.18 cm^2
Time-of-flight Efficiencies: Error Limits: Start, η_1 Stop, η_2	See Tables A.2-3 for H, He ±5%; ±15%

CHAPTER 4: COMPOSITION AND SPECTRA

4.1 Introduction

In the last two chapters we described the technical tools necessary to analyze and understand data processes by the STICS instrument. In this Chapter we apply these tools in order to study ion acceleration in CIRs. We have identified two CIRs for study: the first, CIR 1, was encountered in early April of 1995 and showed evidence of a reverse shock; the second, CIR 2, was encountered late in May of the same year and was associated with compressed plasma which had not yet steepened into shocks.

In this Chapter we analyze the distribution functions observed by STICS for H^+, He^{2+}, and He^+ in several regions of the CIR. The seed populations for accelerated H^+ and He^{2+} are the solar wind with He^{2+} constituting ~5% and H^+ constituting essentially the rest. The seed population for accelerated He^+ are interstellar pickup ions. Pickup ions are formed from interstellar neutrals which wonder freely into the heliosphere and become ionized primarily due to photoionization in the case of helium. The pickup distribution is rather unlike the solar wind ion populations since the pickup process itself provides the ions with considerable energy; the ions are introduced into the solar wind with speeds on the order to the solar wind speed in the plasma rest frame. In some sense, pickup ions can be thought of as a hot population with much lower density as compared to the solar wind ions.

We laid out three relevant and partially unanswered questions in the introduction: namely, which species are most readily accelerated; how are the ions accelerated; and where are the ions accelerated. In this Chapter the first and last of these questions will be illuminated.

In particular, the examination of the three ion populations, H^+, He^{2+}, and He^+ provides us with important clues as to which ion populations are most readily accelerated, or equivalently injected into the acceleration process. Ultimately models

must be developed to better understand the preferential ion injection which is reported here.

The question of where the ions are accelerated is particularly relevant for the CIRs being formed near 1 AU. Since the CIRs are not yet fully formed, shock acceleration theory suggests that the acceleration should occur radially beyond our point of observation.

An important observational benchmark is described in this chapter. Namely, we provide an extended distribution function for helium which combines the spectral information from the STICS, MASS, and EPACT-STEP sensors on the WIND spacecraft. The extended spectrum extends from solar wind energies to several MeV, thereby providing a single observation of ion acceleration from the source population to the very accelerated tail over 14 orders of magnitude in the distribution function. This is the first time such an extended spectrum has been presented for helium in CIRs and provides a significant constraint for acceleration theories in CIRs.

4.2 The Fisk and Lee Model

In this section we describe a simple model of CIR acceleration which serves as a basis of comparison for our observational results. The model was derived from diffusion theory and from observations of ions above 500 keV in energy. The STICS energy range is much lower, and diffusion theory does not strictly apply to the STICS lowest energy bins. But the model does serve as a useful guide and considers the fundamental processes involved in shock acceleration.

In the Fisk and Lee model (1980), particles are accelerated at the forward-reverse shock pair bounding the CIR via a Fermi process causing the ions to exhibit a power law spectrum. The acceleration typically occurs beyond the orbit of Earth because the shocks do not usually form before ~2.5 AU (Hundhausen and Gosling, 1976). The energized particles then move mostly along the magnetic field lines back towards the inner heliosphere (Marshall and Stone, 1978; Zwickl and Roelof, 1981; Christon, 1981). As the particles travel towards 1 AU from the distant heliosphere, they suffer adiabatic deceleration causing their spectra to become exponential.

In the frame of reference corotating with the Sun, the equation for the distribution function, f, along a given streamline for nonrelativistic particles is

$$-\frac{1}{3r^2}\frac{\partial}{\partial r}\left(r^2 V\right)v\frac{\partial f}{\partial v} = \frac{1}{r^2}\frac{\partial}{\partial r}\left(r^2\kappa\frac{\partial f}{\partial r}\right) - V\frac{\partial f}{\partial r} \qquad (4.1)$$

where r is heliocentric radial distance, V is the solar wind speed in the inertial frame fixed with respect to the Sun, v is particle velocity, and κ is the diffusion coefficient. The effects of the shock, which represents a discontinuity in f, can be described by means of the following boundary condition for f at the location of the shock, r_s:

$$-\frac{Vv}{3}\frac{\partial f}{\partial v} - \kappa\frac{\partial f}{\partial r} = -\beta\frac{Vv}{3}\frac{\partial f}{\partial v} \qquad \text{at } r = r_s \qquad (4.2)$$

where
$$\beta = \frac{\left(V'^2 + \Omega^2 r_s^2\right)^{1/2}}{\left(V^2 + \Omega^2 r_s^2\right)^{1/2}}\frac{B}{B'} \qquad (4.3)$$

Here Ω is the angular velocity of the Sun, and B is the magnetic field strength upstream of the shock. V' and B' indicate conditions downstream of the shock.

The approximate solution to equation (4.1) in the region upstream from the shock for the case $\kappa = \kappa_o vr$ (κ_o is a constant), which satisfies equation (4.2) and is finite as r goes to zero, is

$$f \sim \left(\frac{r}{r_s}\right)^{2\beta(1-\beta)^{-1}+V(\kappa_o v)^{-1}} v^{-3(1-\beta)^{-1}} \exp\left(-\frac{6\kappa_o\beta}{(1-\beta)^2}\frac{v}{V}\right) \qquad (4.4)$$

With the assumptions that particles propagate downstream from the shock primarily by convection, and that f is continuous across the shock front, the solution for f in the downstream region is

$$f \sim \left(\frac{r}{r_s}\right)^{-2(1-\beta)^{-1}} v^{-3(1-\beta)^{-1}} \exp\left[-\frac{6\kappa_o\beta}{(1-\beta)^2}\frac{v}{V}\left(\frac{r}{r_s}\right)^{2/3}\right] \qquad (4.5)$$

If the corotation speed, Ωr, is small as compared to the particle speed, v, then f is the same in both the corotating frame and the spacecraft frame, to order $(\Omega r/v)^2$. Since the particles move primarily along the field lines,

$$\kappa = \kappa_{\parallel}\cos^2\psi = \frac{v\lambda_{\parallel}}{3}\cos^2\psi = \kappa_o vr$$
$$\Rightarrow \lambda_{\parallel} = \frac{3\kappa_o r}{\cos^2\psi} \qquad (4.6)$$

where ψ is the angle between the mean magnetic field and the radial direction, $\kappa_{\parallel}$ is the parallel component of the diffusion coefficient, and $\lambda_{\parallel}$ is the parallel mean free path (Savopulos et al., 1995).

4.3 Other Sensors Used

In this chapter, we present data from two other instruments in addition to STICS; lower energy data from SMS-MASS and higher energy data from EPACT-STEP. The MASS instrument uses electrostatic deflection followed by a time-of-flight measurement to determine the elemental and isotopic composition of solar wind ions heavier than hydrogen (Gloeckler et al., 1995; Hamilton et al., 1990). The spherical segment electrostatic deflection system makes 60 logarithmically spaced voltage steps covering 0.52 - 9.89 keV/e with an energy-per-charge bandwidth of 4% (FWHM). In the TOF spectrometer, the ions flight times are measured as they traverse a special retarding potential, which causes the particles to undergo harmonic motion. This potential has the unique property that the ion time-of-flight is independent of the ion energy or entering angle and is proportional to the square-root of its mass-per-charge. The ion's charge at this point is the charge after passing through the carbon foil at the entrance of the TOF spectrometer, and it is typically equal to +1. Therefore, the ion time-of-flight is effectively proportional to the square-root of its mass. Since the MASS instrument can measure time-of-flight to an accuracy of better than 1 ns in the typical range from 60 to 400 ns, a very precise measurement of the ion's mass can be obtained ($m/\Delta m \approx 100$). The sensor divides the spacecraft spin azimuth into a 45° sun sector and a 315° non-sun sector. Only sun-sector data were analyzed in this study.

The SupraThermal Energetic Particle (STEP) instrument is one of the sensors in the Energetic Particles: Acceleration, Composition, and Transport (EPACT) investigation on the WIND spacecraft (von Rosenvinge et al., 1995). The STEP instrument uses the time-of-flight technique followed by an energy measurement with a solid state detector to determine the mass of all ions between He - Fe in the energy range from ~80 keV to ~10 MeV. The sensor consists of two large-area (0.4 cm^2 sr) time-of-flight telescopes with the field of view sampling a region up to ~±35° from the ecliptic plane. The spacecraft spin is divided-up into eight azimuthal sectors. The high

sensitivity of STEP allows measurement of much lower fluxes than those made by previous instruments in the same energy range.

4.4 Event Selection

During the first seven months of 1995, the WIND spacecraft encountered several high-speed solar wind streams (>600 km/s) while it was traveling through interplanetary space upstream of the Earth's bow shock. During this time the spacecraft made its initial pass around the L1 Lagrangian point, where the Sun and Earth's gravitational forces cancel (Figure 4.1). Figures 4.2 and 4.3 show the solar wind speed from the Solar Wind Experiment (SWE) on WIND (courtesy K. Ogilvie) from December 29, 1994 to August 1, 1995 plotted in 27-day panels. Three distinct high-speed streams reappear over several solar rotations and evolve with time. The high-speed streams line-up vertically below labels A, B, and C in Figures 4.2 and 4.3. These fast streams can be traced back to the Sun and appear to originate from three separate coronal holes upon examination of the He 10830 Å coronal hole maps (see Figure 4.4) from the National Solar Observatory, Kit Peak, Arizona (Solar Geophysical Data). Coronal holes A and C were formed in the southern hemisphere of the Sun, whereas coronal hole B originated north of the Sun's equator. The fast wind from coronal hole B was not observed by WIND until the hole moved to below 10° latitude in the southern hemisphere around April 24, 1995 (Figure 4.4). Coronal hole C was an equatorward extension of the southern polar hole and was largest towards the end of May 1995 when it spanned more than 70° in solar longitude, as shown in Figure 4.4.

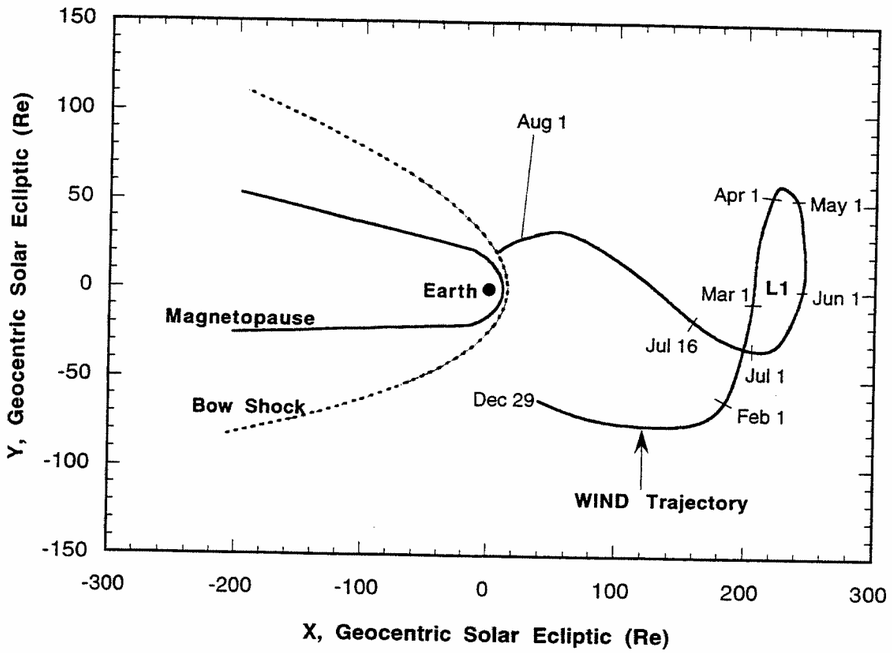

Figure 4.1. The WIND spacecraft trajectory in the x-y Geocentric Solar Ecliptic (GSE) plane from December 29, 1994 (day 363) to August 1, 1995 (day 213). This was the first pass around the L1 Lagrangian point, where the Sun's gravitational force is somewhat larger than the Earth's so the resultant centripetal force causes WIND to orbit the Sun with a 1-year period, thus remaining on the Sun-Earth line.

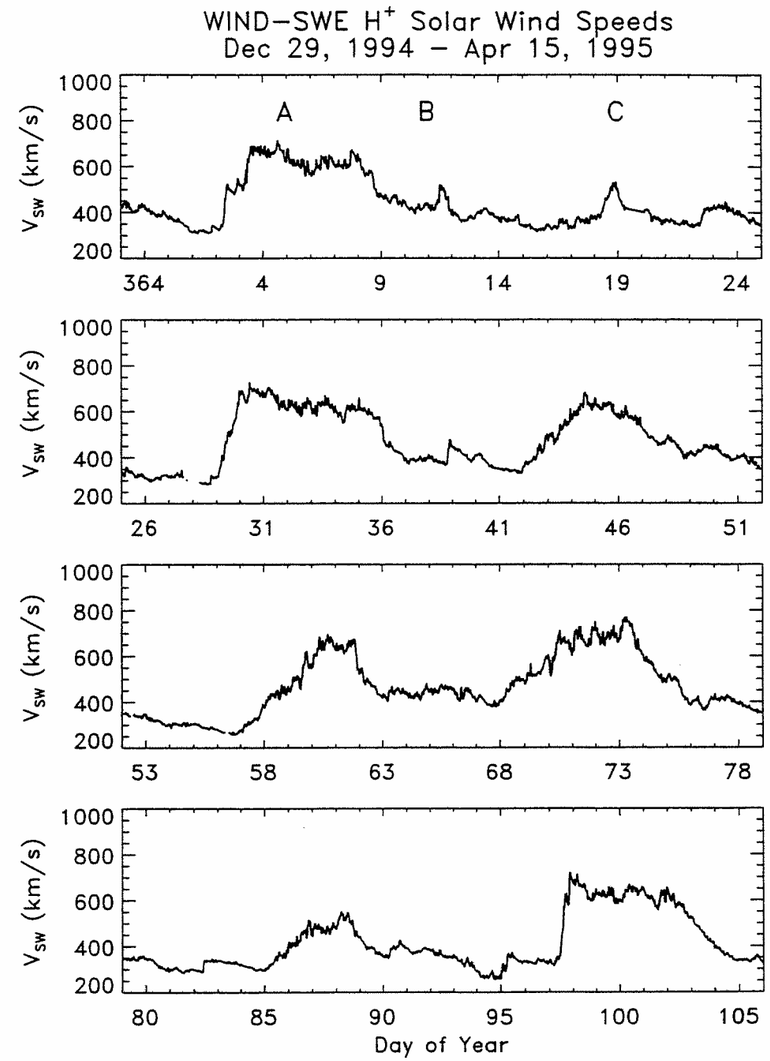

Figure 4.2. The WIND-SWE proton solar wind speeds from Dec 29, 1994 to April 15, 1995 (courtesy K. Ogilvie). The speeds are averaged over 30 minute intervals. Three separate high speed streams line-up vertically below labels A, B, and C.

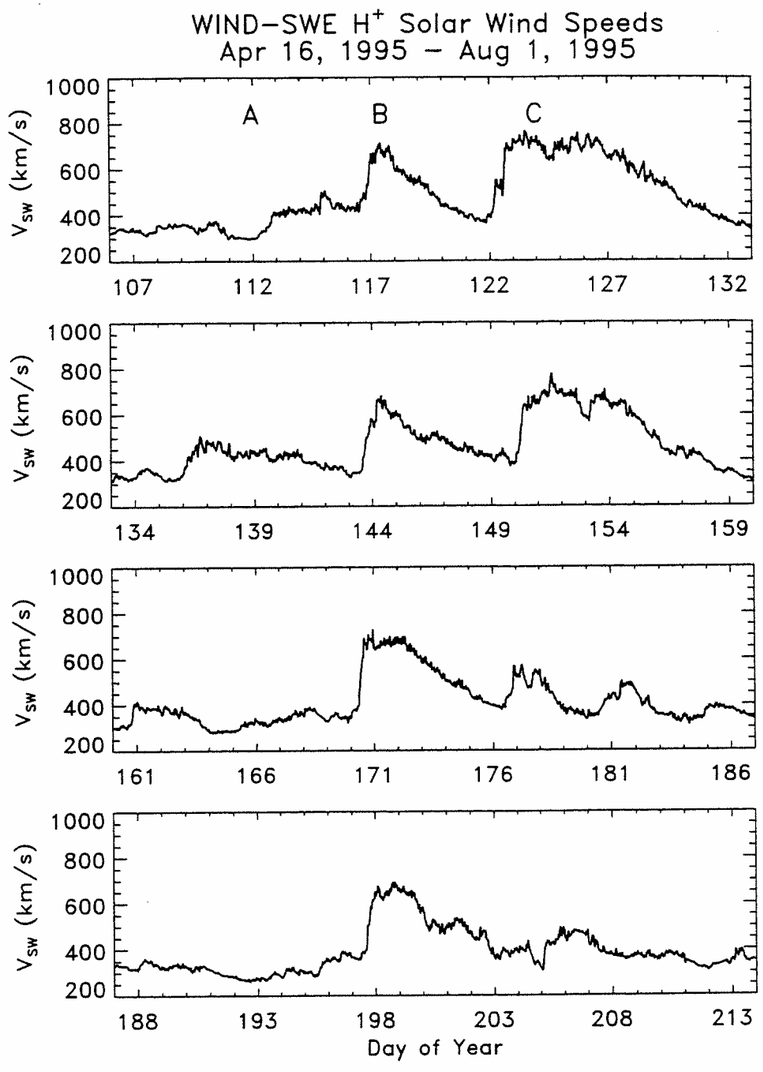

Figure 4.3. The WIND-SWE proton solar wind speeds from April 16 to August 1, 1995 (courtesy K. Ogilvie). The speeds are averaged over 30 minute intervals. Three separate high speed streams line-up vertically below labels A, B, and C.

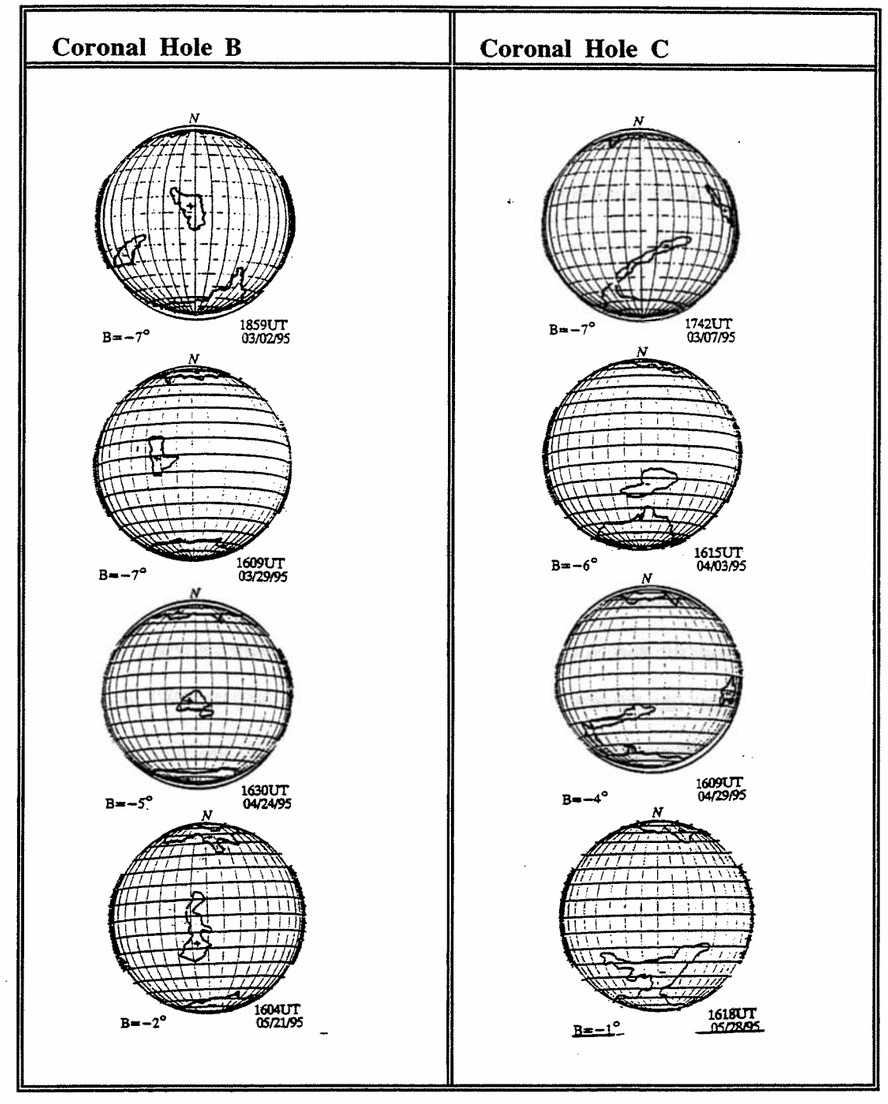

Figure 4.4. Coronal hole maps from the National Solar Observatory, Kitt Peak, Arizona (Solar Geophysical Data) show coronal holes B and C recurring over four solar rotations.

The CIR boundaries were determined using the criteria set forth in Richardson et al. (1993) and in Belcher and Davis (1971). As explained in section 1.2, the beginning of the CIR (S-S' boundary) is identified by an increase in the magnetic field intensity, and in the core plasma density and temperature. Similarly, the end of the CIR (F'-F boundary) coincides with a decrease in these parameters, as shown in Figure 1.3. The stream interface (S'-F' boundary), that separates the slow wind from the fast wind, is characterized by a sharp drop in density, a sharp rise in temperature (or thermal speed), and a small increase in bulk speed (Burlaga, 1974; Gosling et al, 1978), also by a transition from East to West in the plasma flow direction (Belcher and Davis, 1971).

The first CIR chosen for our study occurred between April 6 - 7, 1995, and the second one occurred two solar rotations later between May 29 - 31, 1995. These two events were chosen because they had the best statistics. Both CIRs were driven by fast wind from the same coronal hole. The boundaries of the different CIR regions (S, S', F', F) were identified using the plasma data from the WIND-SWE instrument (Ogilvie et. al., 1995) and the magnetic field data from the WIND-MFI experiment (Lepping et. al., 1995), as shown in Figures 4.5 and 4.6. The occurrence times for the three different CIR boundaries are given in Table 4.1 for each CIR. Typically, the forward and reverse shock pairs associated with CIRs do not fully develop until ~2.5 AU. However, the reverse shock for the first CIR was present at 1 AU. In both cases, the forward shocks were not present at 1 AU. The location of the S-S' boundary were not as clear, so the uncertainties in determining this boundary were greater (±30 minutes). The other two boundaries were determined to within ±10 minutes.

The higher energy data from WIND-EPACT (Figures 4.7 and 4.8) were used to check for the occurrence of solar energetic particle (SEP) events. These events are discrete events on the Sun where particles are accelerated to energies greater than 1 MeV and are associated with solar flares. The higher energy (faster) ions are detected

first followed by the lower energy (slower) ions, i.e., velocity dispersion. These events are detected by a sudden rise in the high-energy rate channels followed by a shorter decay time than that in CIR events (Lanzerotti, 1977). SEP events occurring during the first seven months of 1995 have been identified and discussed by Mazur et al. (1996) and by Reames et al. (1997a). SEP events were not present within our CIR time periods.

These two CIR time periods were also checked for the presence of "upstream ion events". Upstream ions are energetic ions below ~1 MeV that are produced by either Fermi acceleration of solar wind ions at the Earth's bow shock (Scholer et al., 1981; Ipavich et al., 1984; Ellison, 1985; Lee, 1985), or by particles accelerated in the Earth's magnetosphere then escaping into the upstream region (Sarris et al, 1976; Krimigis et al., 1978; Anagnostopoulos, 1995). These events were observed to be more intense and last a short time (less than 4 hours) relative to the CIR events (Mason et al., 1996; Dwyer et al., 1997). The upstream events appear as spikes in the lower energy channels (less than 200 keV/amu) of the STEP data, as can be seen in the 80-160 keV/amu He and CNO rates ~12:00 on day 99 and ~21:00 on day 100 in Figure 4.7. Also, their peak intensities show-up mainly in the STICS earthward looking azimuthal sectors in the spacecraft frame. There were no upstream ion events within our CIR time periods.

Table 4.1. The CIR boundaries for the two different events in our study.

#	S-S'	S'-F'	F'-F	Comments
1	4/6/95 12:00 (96.50)	4/7/95 12:18 (97.51)	4/7/95 20:24 (97.85)	Reverse Shock present at 1 AU. (Day of 1995)
2	5/29/95 4:50 (149.20)	5/30/95 5:58 (150.25)	5/31/95 4:00 (151.17)	Longest lasting event for STICS.

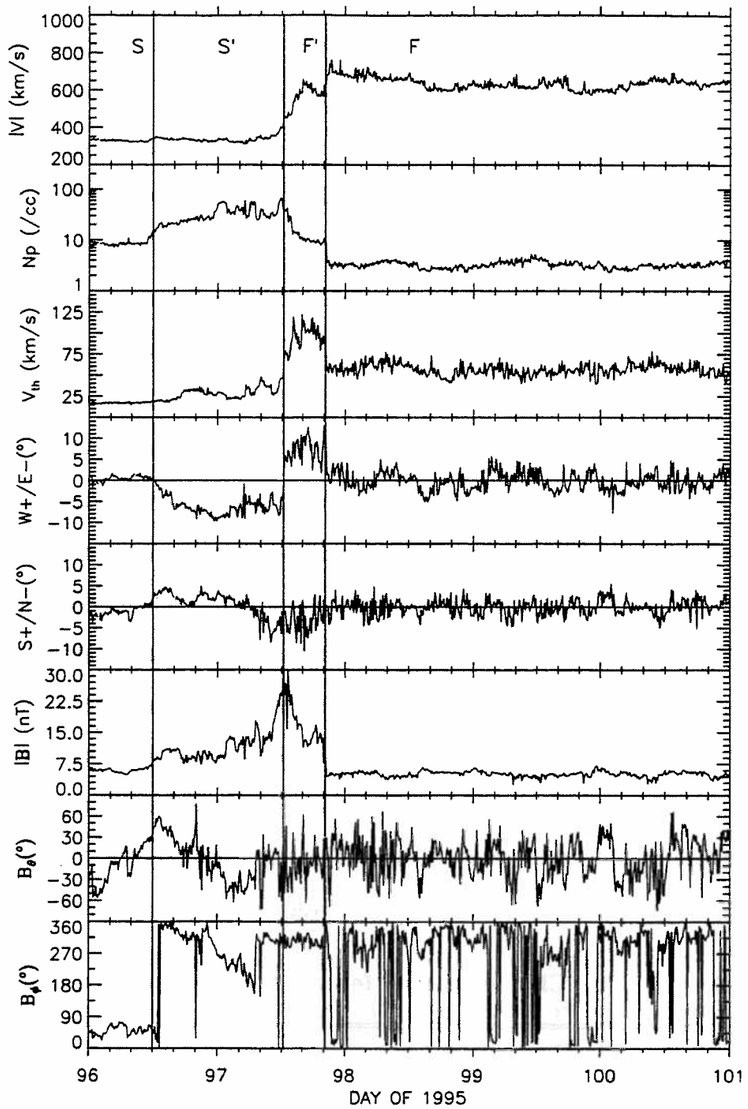

Figure 4.5. Solar wind plasma data from WIND-SWE (courtesy K. Ogilvie) and magnetic field data from WIND-MFI (courtesy R. Lepping) for CIR 1. The time period covers April 6 - 10, 1995 with 10-minute resolution. The solar wind speed, |V|, the density, Np, the thermal speed, V_{th}, the West-East, W+/E-, and the South-North, S+/N-, flow directions are all obtained from SWE. The magnetic field data consists of the field intensity, |B|, the polar, B_θ, and the azimuthal, B_ϕ, directions. The different CIR regions (S, S', F', F) are explained in Figure 1.3.

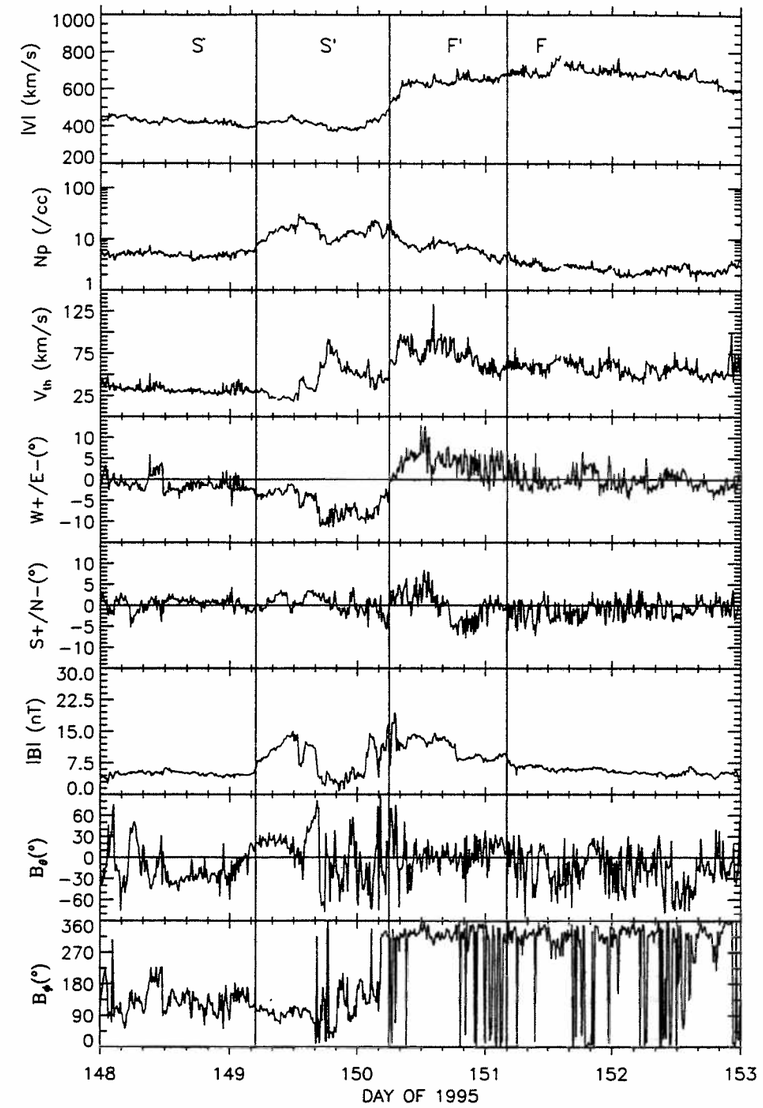

Figure 4.6. Solar wind plasma data from WIND-SWE (courtesy K. Ogilvie) and magnetic field data from WIND-MFI (courtesy R. Lepping) for CIR 2. The time period covers May 28 - June 1, 1995 with 10-minute resolution. The solar wind speed, |V|, the density, Np, the thermal speed, V_{th}, the West-East, W+/E-, and the South-North, S+/N-, flow directions are all obtained from SWE. The magnetic field data consists of the field intensity, |B|, the polar, B_θ, and the azimuthal, B_ϕ, directions. The different CIR regions (S, S', F', F) are explained in Figure 1.3.

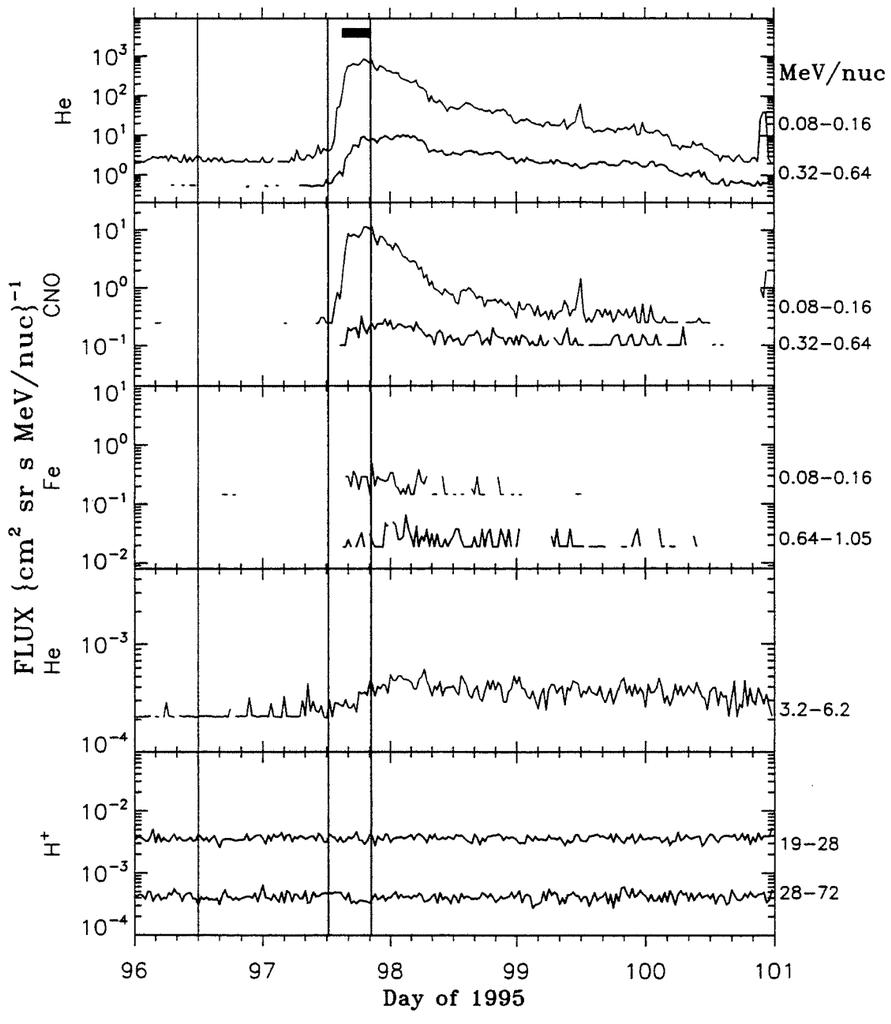

Figure 4.7. CIR 1 data for the higher energy ions from WIND-EPACT (courtesy T. T. von Rosenvinge). The top three panels contain data from the STEP sensor, the fourth panel from the top presents data from the LEMT sensor, and the bottom shows data from the APE-B sensor. The time period covers April 6 - 10, 1995 with 30-minute resolution. The vertical lines indicate the different CIR boundaries as shown in Figure 4.5.

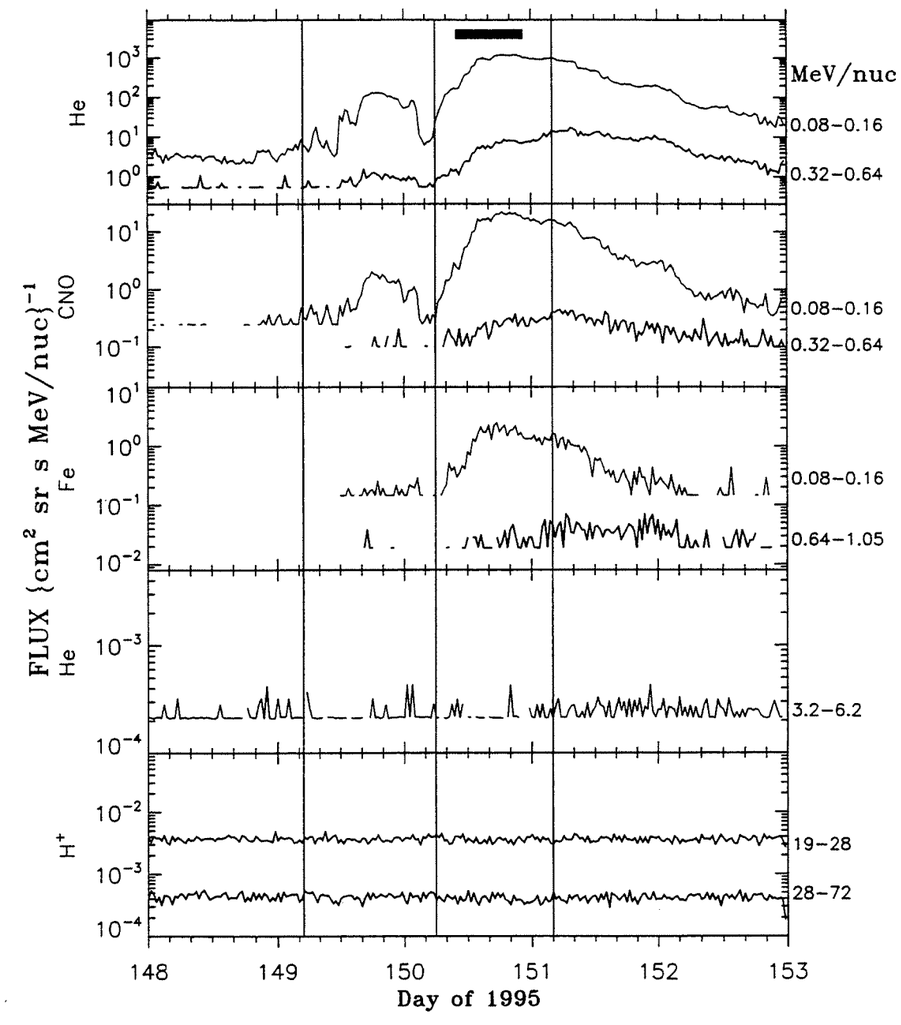

Figure 4.8. CIR 2 data for the higher energy ions from WIND-EPACT (courtesy T. T. von Rosenvinge). The top three panels contain data from the STEP sensor, the fourth panel from the top presents data from the LEMT sensor, and the bottom shows data from the APE-B sensor. The time period covers May 28 - June 1, 1995 with 30-minute resolution. The vertical lines indicate the different CIR boundaries as shown in Figure 4.6.

4.5 Observations

The STICS H^+ omni-directional data for three different energy ranges (10-35, 40-100, and 100-200 keV/amu), the He^{2+}/H^+ ratio, and the He^+/He^{2+} ratio for the 10-35 keV/amu energy range for each CIR are shown in Figures 4.9 and 4.10. The rates were determined using the PHA data with 30-minute time resolution. The energy ranges were obtained by adding together data from adjacent energy bins, and the data were averaged over all azimuthal and polar sectors. The ratios were calculated only if there were at least 5 counts for each ion. The H^+, He^{2+}, and He^+ ions were identified from mass-per-charge charge data alone (double coincidence) and also from both mass and mass-per-charge data (triple coincidence, as explained in Section 2.3).

For the April event, the STICS count rates were very low before the stream interface, but the H^+, He^{2+}, and He^+ rates all increase near the interface and peak within the compressed fast wind, F' region, approximately 1 hour downstream of the reverse shock (Figure 4.9). The He^{2+}/H^+ and He^+/He^{2+} remained relatively constant with average values of ~0.15 and ~0.20, respectively. Energetic particle instruments (e.g. WIND-EPACT) typically observe the corotating energized ions up to 2-3 days after the F'-F boundary, well into the unperturbed high speed stream (Reames et al, 1997b). STICS detects the accelerated ions for 10-16 hours, at most, after the F'-F boundary because of its smaller geometric factor. The May event is the longest lasting CIR event observed by STICS. It is the only CIR event in 1995 in which STICS sees energized ions throughout all four regions (S, S', F', F). Here again the He^{2+}/H^+ and He^+/He^{2+} remained relatively constant in the F' region with average values of ~0.20 and ~0.25 in the 10-35 keV/amu energy range, respectively. But, in the S' region, the He^{2+}/H^+ was lower with an average value of ~0.10.

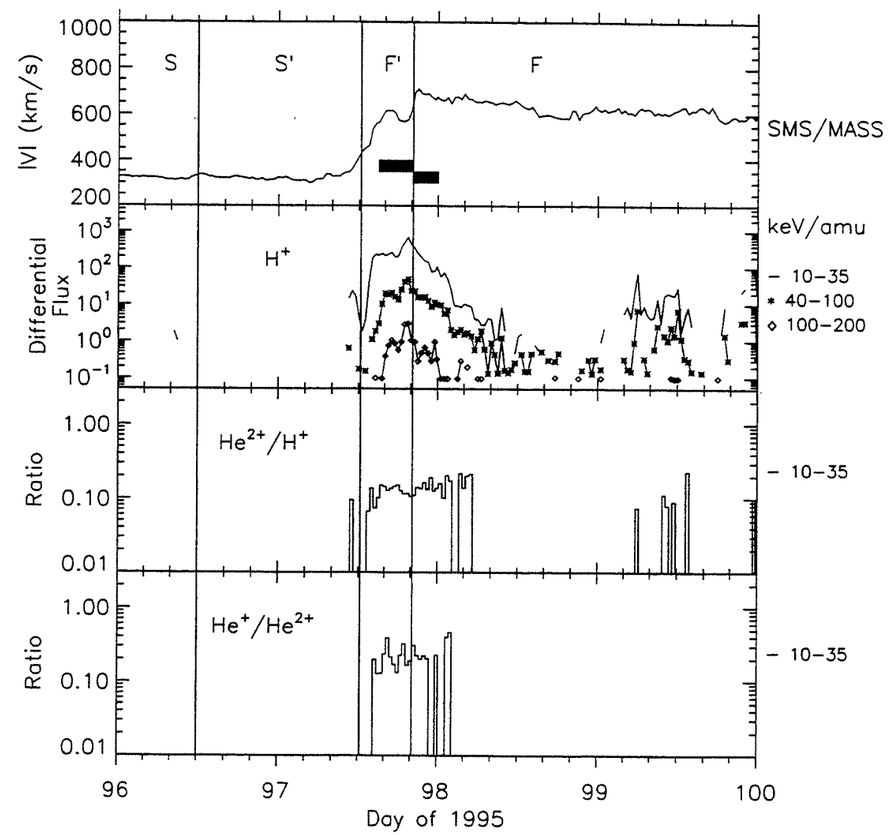

Figure 4.9. The STICS omni-directional H^+ rates at three different energy levels (10-35, 40-100, and 100-200 keV/amu) are shown for CIR 1. The He^{2+}/H^+ and He^+/He^{2+} ratios are presented for the 10-35 energy range. The proton solar wind speed was obtained from SMS-MASS. The time period covers April 6 - 10, 1995 with 30-minute resolution. The shaded rectangular bars in the top panel indicate the two time intervals over which spectra were obtained.

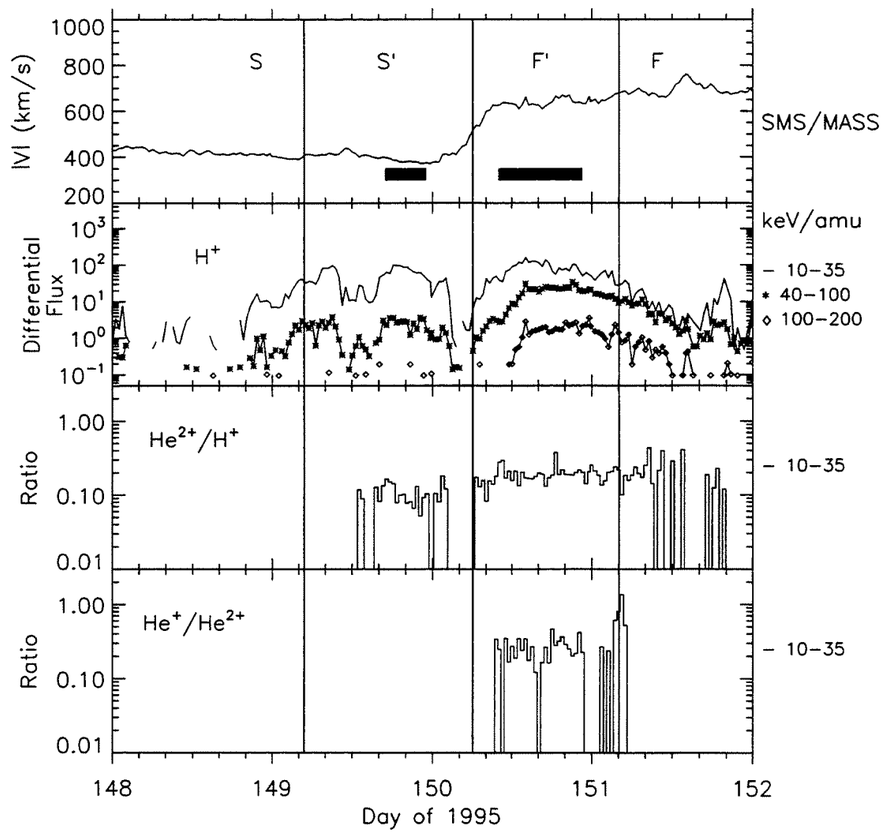

Figure 4.10. The STICS omni-directional H^+ rates at three different energy levels (10-35, 40-100, and 100-200 keV/amu) are shown for CIR 2. The He^{2+}/H^+ and He^+/He^{2+} ratios are presented for the 10-35 energy range. The proton solar wind speed was obtained from SMS-MASS. The time period covers May 28 - June 1, 1995 with 30-minute resolution. The shaded rectangular bars in the top panel indicate the two time intervals over which spectra were obtained.

The H^+, He^{2+}, and He^+ distribution functions were determined for four different time periods, two from the April event and two from the May event. Table 4.2 gives the plasma (SWE) and magnetic field (MFI) data for each time period. The SWE parameters were obtained from fitting the peak of the proton reduced distribution function to a Maxwellian for 90 s intervals (J. Steinberg, private communication). The values shown in Table 4.2 are the average of the 90 s values over the entire time period, and the associated error limits represent one standard deviation from the mean. The magnetic field data are also the average of 90 s values.

Table 4.2. The four different time periods for which H^+, He^{2+}, and He^+ distribution functions were obtained. The proton plasma parameters (V_p, solar wind speed, v_{thp}, thermal speed, n_p, density) were obtained from the average of 90-second values from the SWE data. Similarly, the magnitude of the magnetic field (|B|) is the average of 90 s values. The error limits represent one standard deviation from the mean.

	Time Period	V_p (km/s)	v_{thp}(km/s)	n_p (cm^{-3})	|B| (nT)
1a	Apr 7, 15:00 - 20:00	599 ± 28	100 ± 11	9.8 ± 1.5	14.2 ± 1.7
1b	Apr 7, 20:30 - 24:00	698 ± 20	59 ± 17	3.3 ± 0.3	4.9 ± 0.4
2a	May 29, 17:00-23:00	388 ± 12	65 ± 12	10.6 ± 2.0	3.5 ± 1.2
2b	May 30, 10:00-22:30	645 ± 23	80 ± 11	7.3 ± 1.1	11.5 ± 2.3

The solar wind He^{2+} parameters given in Table 4.3 were obtained by first concatenating the MASS and STICS uni-directional reduced distribution functions up to 1.6 V_{sw} averaged over the entire time period. The parameters were then determined by fitting the combined solar wind He^{2+} distribution to the following one-dimensional kappa function:

$$g(v) = \frac{n\Gamma(\kappa+1)}{v_{th}\sqrt{\pi}\kappa^{3/2}\Gamma(\kappa-1/2)}\left[1 + \frac{(v-v_{sw})^2}{\kappa v_{th}^2}\right]^{-\kappa} \qquad (4.1)$$

(Summers and Thorne, 1991). In this expression, g(v) is the reduced distribution function in units of $[cm^3\ km/s]^{-1}$; n is the particle density; v_{th} is the thermal speed; v_{sw} is the solar wind speed; Γ is the gamma function, and κ is the power law index of the differential intensity at higher energies. The core plasma parameters from the kappa fit agreed with those obtained from fitting only the peak to a Maxwellian to within 10% (Chotoo et al., 1998; see Figure 4.11). The values for time period 2a were obtained from the MASS data alone because of the low solar wind speed, and the MASS statistics were not as good as those of the other time periods. Since the peak proton channels saturate, similar MASS solar wind values for H^+ are not given.

Table 4.3. Results of the kappa fits to the combined STICS and MASS He^{2+} data. The mean MASS proton solar wind speed, V_p, is the average of all the 3-minute speeds determined from Maxwellian fits. The bulk speed (V_α), thermal speed ($v_{th\alpha}$), density (n_α), and the Kappa values are all determined from the kappa fit to the helium spectra over the entire interval.

Time Period	V_p(km/s)	V_α/V_p	$v_{th\alpha}/v_{thp}$*	n_α/n_p* ($\times 10^{-2}$)	Kappa
1a	590 ± 27	1.045 ± 0.007	1.14 ± 0.15	4.8 ± 0.8	$2.99^{+0.96}_{-0.31}$
1b	688 ± 18	1.030 ± 0.003	1.18 ± 0.35	4.8 ± 0.5	$3.36^{+0.43}_{-0.29}$
2a	383 ± 9	0.998 ± 0.015	0.95 ± 0.22	3.1 ± 0.7	$4.19^{+6.06}_{-1.18}$
2b	638 ± 21	1.065 ± 0.004	1.25 ± 0.18	5.2 ± 0.8	$3.87^{+0.26}_{-0.17}$

*Proton density, n_p, and thermal speed, v_{thp}, obtained from WIND-SWE as given in Table 4.2.

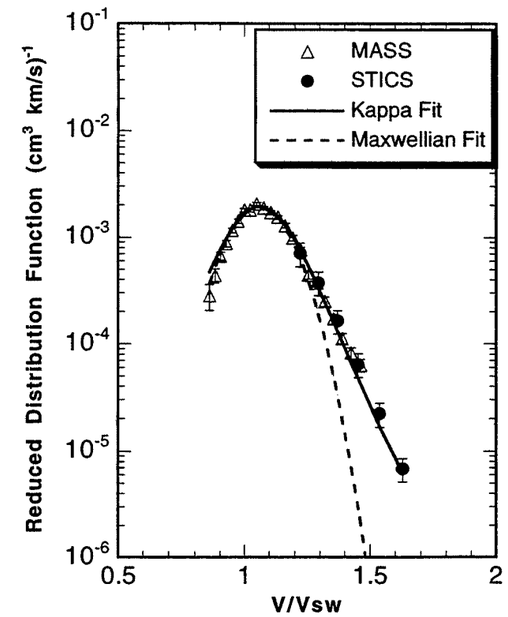

Figure 4.11. The Maxwellian fit to the core of the He^{2+} solar wind distribution and the Kappa fit to the entire solar wind distribution are shown for the time interval May 30, 1995, 10:00 - 22:30 UT.

To obtain reasonable statistics for STICS, the time periods covered several hours. The solar wind speed, V_{SW}, was obtained from the SWE key parameter data every 3 minutes. For both MASS and STICS, the distribution function was then binned according to ion speed in the spacecraft frame normalized by the solar wind speed, V_{SW}, every 3 minutes for each time period. However, the STEP data were first accumulated over the entire time period, then the velocity bins were normalized to the average solar wind speed. STEP cannot distinguish between the different charge states, so its data consist of both He^+ and He^{2+}. But since the abundance of He^+ relative to He^{2+} is roughly 15% as determined by STICS (see table 4.5), then the STEP counts are mainly He^{2+} ions.

As the normalized velocity bins for He^{2+} extended down to solar wind energies, the He^{2+} distribution involved adding together the highly anisotropic solar wind ions and the omni-directional accelerated ions (Gosling et al., 1981; Gloeckler et al., 1995). Chotoo et al. (1998) found that the core He^{2+} solar wind ions in the ambient fast solar wind extended up to 1.6 V_{SW}. So, the distribution function below 1.6 V_{SW} was taken to be a parallel beam, and that above 1.6 was analyzed as omni-directional. The "break" in the He^{2+} spectrum at 1.6 V_{SW} is due to the differences in the instrument response function for parallel beams versus omni-directional ions. Physically, there would be a gradual transition in the spectrum from parallel beam to omni-directional ions. However, limitations in our instrumentation does not allow us to map this transition region in detail. Only data from the in-ecliptic STICS TOF telescope were used in obtaining the various spectra.

4.5.1 April Event Spectra

Figure 4.12a shows the H^+, He^{2+}, and pickup He^+ distribution functions in the spacecraft frame for the first time period, April 7, 1995, 15:00 - 20:00 UT. This time period occurred within the CIR in the compressed fast wind (F' region) downstream of the reverse shock. Due to the large thermal speed, v_{th}, of the solar wind ions, the suprathermal tails of the H^+ and He^{2+} ions blend smoothly into the accelerated ion distributions at 2 V_{SW}. The distributions for all three species beyond 2 V_{SW} are well fit to power laws ($f = Av^{-\gamma}$) with all three species having the same spectral index agreeing within one standard deviation (see Table 4.4). The abundance ratios for the different species between 2.5 - 6.0 V_{SW} are given in Table 4.5. Due to the low He^+ counts, adjacent He^+ velocity bins were added together to increase the statistics. These larger bins are indicated by the horizontal error bars. The relatively large uncertainties associated with the He^+/He^{2+} ratios are reflective of the low He^+ counts as Poisson statistics were used to determine the error bars.

The second time period (Figure 4.12b) occurred upstream of the reverse shock in the ambient fast wind (F region) outside the interaction region. Here, the smaller thermal speed and the harder energetic ion spectrum reveal a "ledge" in the He^{2+} distribution between 1.6 and 2.0 V_{SW}. The ledge is also present in the H^+ distribution, but it is not as clear. The expected ledge in the He^+ distribution represents the un-accelerated pickup ions. In this speed interval the He^+/He^{2+} ratio is approximately equal to 1, as seen in Figure 4.12b. Even though the He^+/He^{2+} ratio between 1.6 - 2.0 V_{SW} is about 100 greater than that in the first time period, the value between 2.5 - 6.0 V_{SW} remains the same at 0.13, as seen in Table 4.5. This suggests that the ledge in the H^+ and He^{2+} data may simply be the "leveling off" of the accelerated ion spectra at lower energies and not source ions. Note that the un-accelerated pickup He^+ flux in the F' region (Figure 4.12a) is about 10 times greater in than that in the F region (Figure 4.12b), as observed previously (Gloeckler et al., 1994). Due to the increased

densities in the S' and F' region, the flux of the pickup ions is enhanced because of the increased charge exchange of neutrals with the solar wind.

The H^+ distribution beyond 2.3 V_{SW} fits better to an exponential ($f = Ae^{-v/v_o}$) function than to a power law as determined by the χ^2 of the fits. Both the He^{2+} and He^+ fit equally well to both the power law and exponential because of the smaller velocity range and lower counts. The exponential nature of the spectra is probably a result of the decreasing flux in the F region as the spacecraft moves away from the reverse shock (see Figure 4.9).

The extended helium spectrum is shown for the first time period (Figure 4.13). This extended spectrum was obtained by adding together data from three separate sensors, SMS-MASS, SMS-STICS, and EPACT-STEP, covering approximately 1 - 1000 keV/amu in energy and spanning 14 orders of magnitude in phase space density. The combined data shows the thermal solar wind distribution, the non-thermal tail, and the accelerated ion population up to ~25 V_{SW}. The power law nature of the spectrum is also seen in the STEP data, which has a slightly larger power law index of 8.02 ± 0.01.

(4.12a)

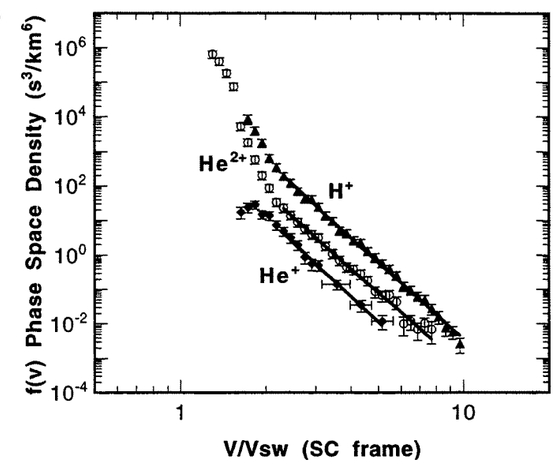

(4.12b)

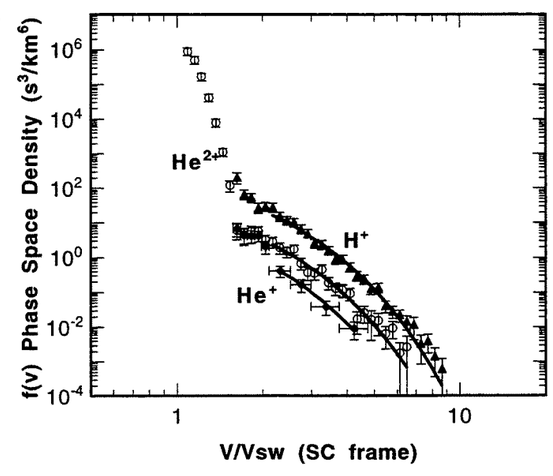

Figure 4.12. The STICS H^+, He^{2+}, and He^+ omni-directional velocity distributions in the spacecraft frame for CIR 1 (a) April 7, 1995, 15:00 - 20:00 UT, F' region (b) April 7, 1995 20:30-24:00 UT, F region. The horizontal error bars on the He^+ represent the larger summed velocity bins.

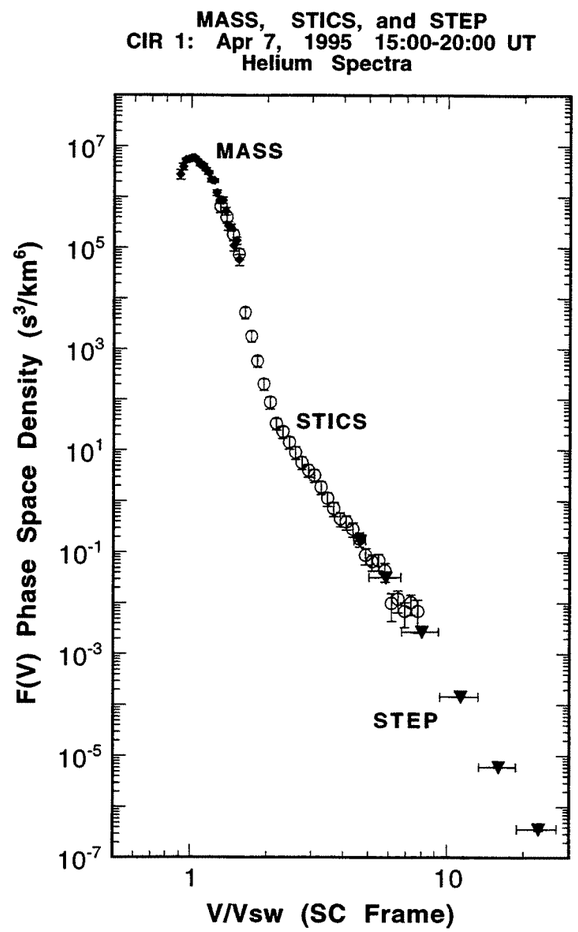

Figure 4.13. The combined helium distribution function using SMS-MASS, SMS-STICS, and EPACT-STEP for CIR 1, April 7, 1995, 15:00 - 20:00. The energy range is from ~1 - 1000 keV/amu covering 14 orders of magnitude in phase space density.

4.5.2 May Event Spectra

The first time period analyzed for this event (see Table 4.2) occurred in the compressed slow wind (S' region). Because of the low solar wind speed, 388 km/s, STICS was only able to measure the accelerated ions beyond 2 V_{SW}. Also the He^+ count rate was not high enough to get a reasonable spectrum. The distributions for H^+, He^{2+}, and He^+ in the spacecraft frame displayed power law spectra with $\gamma \approx 8$ for all three species (Figure 4.14a). The alpha-proton ratio was the same as that in the April event.

For time period 2b, the data were accumulated over 12.5 hours in order to get as many He^+ counts as possible (see Figure 4.14b). Both the H^+ and He^{2+} distributions are exponential in form with the same characteristic velocity, v_o, as shown in Table 4.4. However, the He^+ spectrum displayed a power law form. The He^{2+}/H^+ ratio was largest in this case, but the He^+/He^{2+} ratio was the same as those obtained in the April event (Table 4.5). The extended helium distribution is also shown for this time period in figure 4.15. The exponential nature of the distribution also extends through the STEP data.

Table 4.4. The STICS data above 2 V_{SW} were fit to either a power law, $Av^{-\gamma}$, or to an exponential, Ae^{-v/v_o}, where A, γ, and v_o are constant fit parameters. The spectral indices, γ and v_o, are given for each species in the spacecraft frame.

Time Period	Spectral Form: $Av^{-\gamma}$ or Ae^{-v/v_o}			
	H^+	He^{2+}	He^+	Region
1a	$\gamma = 7.4 \pm 0.1$	$\gamma = 7.2 \pm 0.2$	$\gamma = 7.6 \pm 0.6$	F'
1b	$v_o = 0.57 \pm 0.02$	$v_o = 0.53 \pm 0.04$	$v_o = 0.49 \pm 0.08$	F
2a	$\gamma = 8.1 \pm 0.2$	$\gamma = 8.3 \pm 0.2$	$\gamma = 8.4 \pm 1.2$	S'
2b	$v_o = 0.87 \pm 0.03$	$v_o = 0.83 \pm 0.05$	$\gamma = 6.3 \pm 0.8$	F'

Table 4.5. Abundance ratios between 2.5-6.0 V_{SW} for the different time periods. For time period 2a, the He^+ counts were to low to get a reasonable abundance so no ratio is given.

Time Period	Velocity Range = 2.5 - 6.0 V_{SW}			
	He^{+2}/H^+	He^+/He^{+2}	E/Nuc (keV/amu)	Region
1a	0.12 ± 0.01	0.17 ± 0.06	11.7 - 67.6	F'
1b	0.14 ± 0.01	0.17 ± 0.12	15.9 - 91.4	F
2a	0.11 ± 0.01	---------	4.9 - 28.3	S'
2b	0.18 ± 0.01	0.16 ± 0.06	13.6 - 78.0	F'

(4.14a)

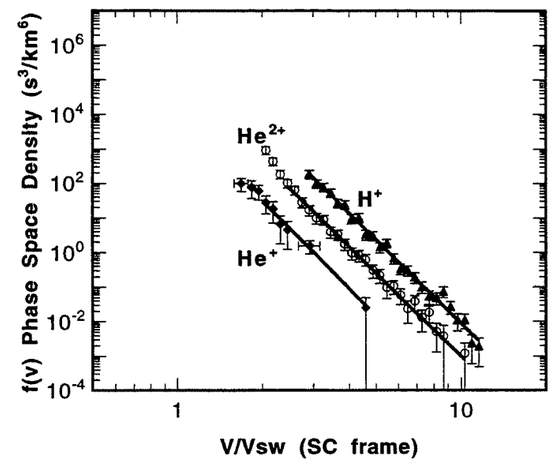

(4.14b)

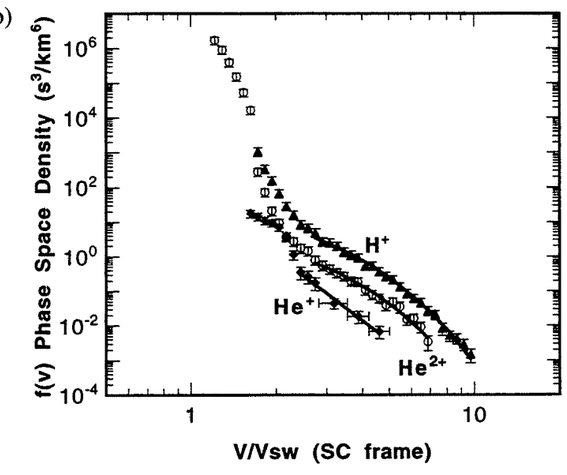

Figure 4.14. The STICS H^+, He^{2+}, and He^+ omni-directional velocity distributions in the spacecraft frame for CIR 2 (a) May 29, 1995, 17:00 - 23:00 UT, S' region (b) May 30, 1995 10:00 - 22:30 UT, F' region.

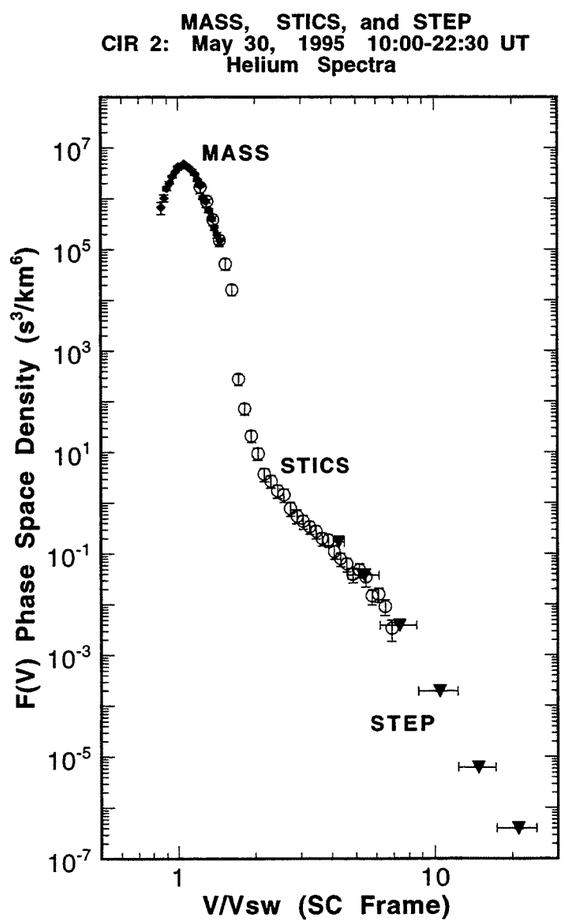

Figure 4.15. The combined helium distribution function using SMS-MASS, SMS-STICS, and EPACT-STEP for CIR 2, May 30, 1995, 10:00 - 22:30. The energy range is from ~1 - 1000 keV/amu covering 14 orders of magnitude in phase space density.

4.6 Analysis

4.6.1 Comparison between the Fisk and Lee (1980) model and observations

As a basis for comparison, equation (4.5) was used to generate a spectrum, which was then compared to H^+, He^{2+} and He^+ STICS data and the extended He STEP data from CIR 1a. The value of β was first calculated using equation (4.3). The measured value of B'/B = 1.68 was obtained from the magnetic field instrument (courtesy Adam Szabo), and V = 697 km/s and V' = 580 km/s were measured by WIND-SWE (courtesy K. Ogilvie). Since the measurements were made at 1 AU and the reverse shock was also present at 1 AU, then $r/r_s = 1$. The value used for κ_o was 0.014. By substituting these parameters into equation (4.5), the predicted distribution function, f, from the Fisk and Lee model is

$$f \sim \left(\frac{v}{v_{sw}}\right)^{-6.25} \exp\left(-0.19\frac{v}{v_{sw}}\right) \qquad (4.6)$$

Both the data and the normalized model distributions are shown in Figure 4.16a. As can be seen from the figure, the model fits the data reasonably well. Using the measured value for $\psi = 300^\circ$ along with the value for κ_o and r = 1 AU, a mean free path of $\lambda_{||} = 0.17$ AU was obtained from equation (4.6). This $\lambda_{||}$ value is similar to that obtained by Zwickl and Webber (1977), whose value was used by Fisk and Lee (1980) when comparing their model to actual data.

Since the reverse shock was not present at 1 AU during CIR 2b, r_s and β could not be measured directly. Using $\kappa_o = 0.014$, $\beta = 0.57$, and $r_s = 1.18$ AU in equation (4.4), we can get the predicted distributions from the Fisk and Lee model for H^+, He^{2+}, and He^+. The normalized model distributions fit the data for time period 2b reasonably well, as shown in Figure 4.16b. The shock location, $r_s = 1.18$ AU, is reasonable because the low energy particles detected by STICS are expected to originate from regions relatively close to 1 AU. Also, the similarity in the abundance ratios for

the two CIRs (see Table 4.5) suggests that the two shock locations should be close. This clearly shows that the particles are originating from much closer in than previously expected [*Reames et al.,* 1997].

Since the solar wind speed remains relatively constant between 1.00 AU and 1.18 AU, then using the measured speeds at 1 AU, i.e., V' = 645 km/s and V = 690 km/s, along with $\beta = 0.57$, and $r_s = 1.18$ AU in equation (4.3), we get B'/B = 1.67, similar to the measured value for CIR 1a.

Clearly the first case, CIR 1a, is better constrained since the reverse shock was present at 1 AU. In this case, only one free parameter, $\lambda_{||}$, exists in the model. The agreement here suggests once again that convection, adiabatic cooling, and diffusion are the essential ingredients for diffusive acceleration. In the case of CIR 2b, the exponential spectrum suggests that ions are accelerated beyond the point of observation and cooled as they diffuse to the point of observation.

4.6.2 CIR 1 and 2 Source Distributions

In this section, we describe the solar wind H^+ and He^{2+} spectra with kappa distributions, and determine the speed, v_1, at which the He^{2+}/H^+ abundance becomes the same as that observed for the energetic particles. In Figure 4.17, the kappa distributions for H^+ and He^{2+} are shown along with the ratio He^{2+}/H^+ for CIR 1a and 2b. The H^+ and He^{2+} distributions were generated using equation 4.1 along with the measured parameters in Tables 4.2 and 4.3. The H^+ kappa value was first taken to be the same as the He^{2+} value. Then it was adjusted slightly until the He^{2+}/H^+ ratio agreed with the STICS data at 1.7 and 1.8 V_{SW}. Because of the larger thermal speed and greater bulk velocity, there are relatively more He^{2+} ions than H^+ ions in the suprathermal tail than in the core distribution.

For CIR 1a (Figure 4.17a), the He^{2+}/H^+ abundance ratio at 1.45 V_{SW} (870 km/s) is the same as that of the energetic particles between 2.5 - 6.0 V_{SW} as given in Table 4.5. With the reverse shock absent at 1 AU during CIR 2b, the accelerated particles originated from the shock at 1.2 AU, as determined in Section 4.6.1. Since the source distribution below 2 V_{SW} is not expected to change much between 1.0 and 1.2 AU, the source measurements made at 1.0 should be similar to those at 1.2 AU. In Figure 4.17b, the He^{2+}/H^+ ratio above 1.30 V_{SW} (838 km/s) is ~0.20, essentially the same as that of the accelerated particles.

Therefore, this suggests that the average injection speed for the H^+ and He^{2+} ions is roughly 1.4 V_{SW} (or 850 km/s). Also, differences in the abundance ratio between events can be attributed to changes in the source population.

4.6.3 Accelerated Ion Intensities

The STICS H^+ and He^{2+} data are plotted together for both CIRs, time periods 1a and 2b, in Figure 4.18a and b, respectively. With the reverse shock present at 1 AU for the first CIR, the intensity of the accelerated ions around 3 V_{SW} are about 10 times greater than that during the second CIR, when the shock was no longer present. However, the difference in intensity decreases with speed. The lower energy ions would experience greater difficulty in traveling back from 1.2 AU causing less to be observed at 1 AU. On the other hand, the higher energy ions easily make the trip from 1.2 AU to 1.0 AU causing the spectra for the two CIRs to merge at the higher energies.

(4.16a)

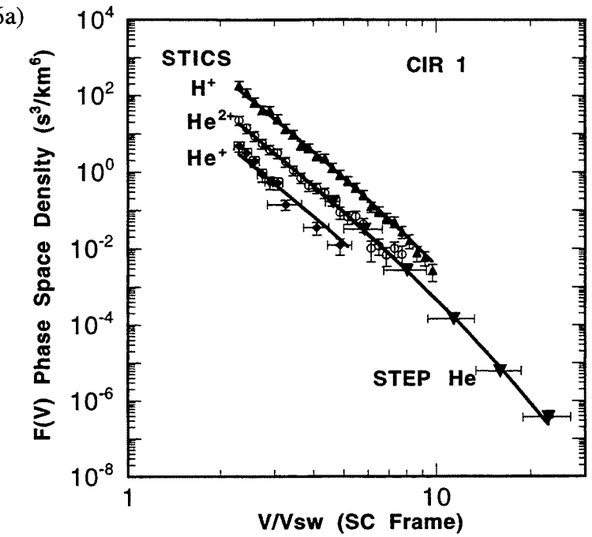

(4.16b)

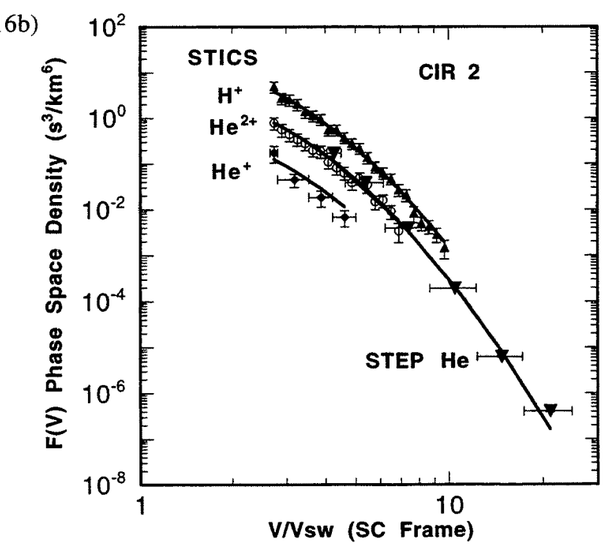

Figure 4.16. Comparison between the STICS H^+, He^{2+}, and He^+ data and EPACT-STEP He data and the Fisk and Lee model for CIR 1a (a) and CIR 2b (b). The solid lines through the data points represent the normalized predicted distributions. The model fits the data reasonably well in both cases. In both cases, a mean free path of 0.17 AU was used. For CIR 2, the shock location was found to be 1.18 AU.

(4.17a)

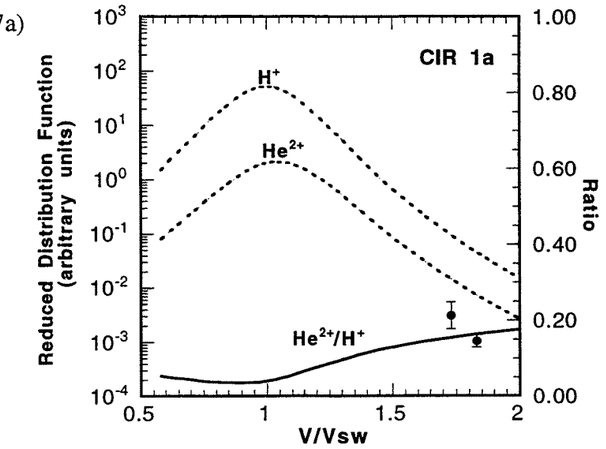

(4.17b)

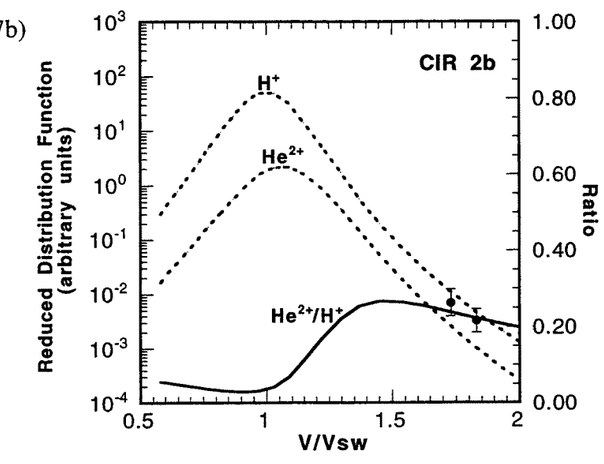

Figure 4.17. The kappa distributions for H^+ and He^{2+} are shown along with the ratio He^{2+}/H^+ for CIR 1a and 2b. The H^+ and He^{2+} distributions were generated using equation 4.1 and the measured parameters in Tables 4.2 and 4.3. The H^+ kappa value was first taken to be the same as the He^{2+} value, then slightly adjusted until the He^{2+}/H^+ ratio was similar to the STICS measured values at 1.7 and 1.8 V_{SW} (circular data points). (a) For CIR 1a, the abundance ratio above 1.45 V_{SW} (870 km/s) is the same as that of the energetic particles between 2.5 - 6.0 V_{SW} as given in Table 4.5. (b) For CIR 2b, the ratio above 1.30 V_{SW} (838 km/s) is essentially the same as that of the accelerated particles.

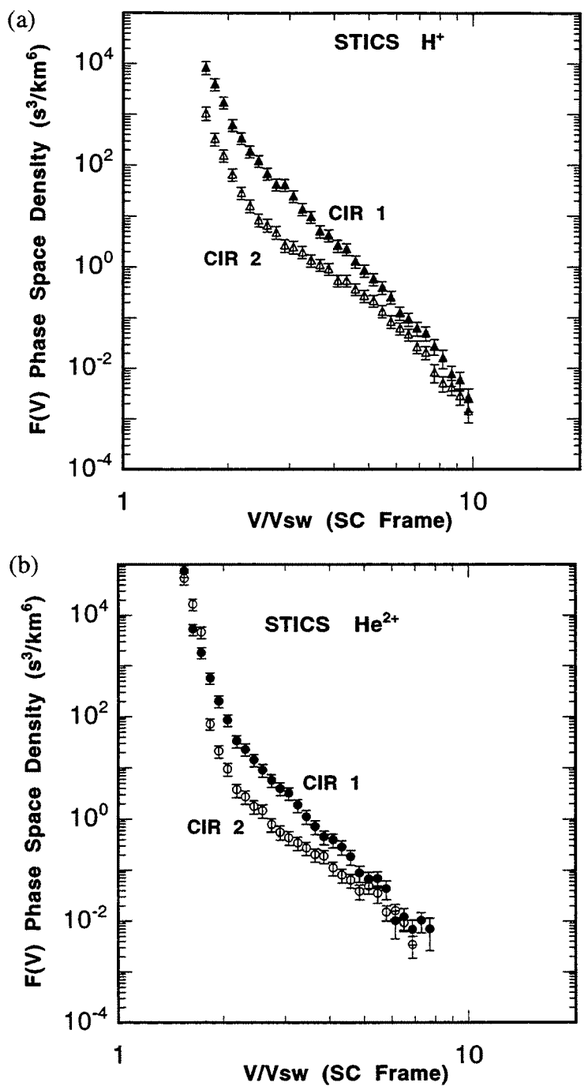

Figure 4.18. The STICS H^+ (a) and He^{2+} (b) data are plotted together for both CIRs.

4.7 Discussion

In modeling the solar wind as a source population for ions accelerated in CIRs it is important to accurately describe the ion distributions (e.g., Kappa Function).

The kappa function form is ubiquitous in space plasmas, and it is very useful in describing the solar wind. The Maxwellian function fits the core of the solar wind ion distribution, but it completely misses the tail, as shown in Figure 4.11. On the other hand, the kappa function (see equation 4.1) does the job of the Maxwellian by determining the plasma parameters (V_{SW}, v_{th}, and n) and accurately fits the entire solar wind He^{2+} distribution. In addition, the κ value gives a measure of the relative amount of particle flux in the high energy tail of the distribution; as κ decreases, the distribution becomes less Maxwellian and the suprathermal tail becomes more pronounced. As κ becomes infinitely large, the kappa distribution becomes Maxwellian. In the CIR fast wind regions, $\kappa = 3\text{-}4$, which is one unit less than the values obtained by Chotoo et al. (1998) in the ambient high-speed streams, indicating that the solar wind ions are being accelerated in the CIRs, as expected. A lower kappa value means that there are more particles in the suprathermal tail that can be injected into the acceleration process.

The location of ion acceleration is reasonably constrained through comparison of observed spectra and the Fisk and Lee (1980) model.

The general trends of the observed spectra are consistent with the predictions of the Fisk and Lee (1980) model. For the first CIR event, where the reverse shock is present at 1 AU, the spectra conform to a single power law, and for the second CIR event, in which no shocks had yet formed, exponential spectra are observed. By balancing convection, diffusion, and adiabatic cooling, the Fisk and Lee model shows that if shocks are nearby, distributions form power laws driven directly by the shock acceleration. If the acceleration occurs due to non-local shocks, the distribution

takes on an exponential shape since ions are adiabatically cooled as they diffuse from the shock. In the case of the first CIR event, detailed fits using the observed shock compression were performed and proved consistent with the observed spectrum.

The Fisk and Lee (1980) model was developed in the frame of reference corotating with the Sun. For particle speeds much greater than the corotation speed (~400 km/s at 1 AU), the omnidirectional distribution function is the same in both the corotating frame and the spacecraft frame. The model expects all CIR accelerated ions to display the same spectral form and have the same spectral index regardless of their mass or charge. By examining Table 4.4 and Figure 4.16, we see that this holds true even down to particle speeds as low as 3 times the corotation speed.

When no shock is present at 1 AU, the conventional view is that the energetic particles observed at 1 AU originate from between 3 - 5 AU [*Reames et al.,* 1997]. However, we find that the energetic particles are originating from only 0.2 AU beyond our observing point.

Solar Wind H^+ and He^{2+}: Injection and Bulk Motion

From Tables 4.2 and 4.3, the following average ratios for solar wind ions

$$n_\alpha/n_p = 0.050 \qquad v_{th\alpha}/v_{thp} = 1.19$$

for the fast wind (both F' and F regions) agree with previous work within experimental uncertainties (Feldman et al., 1977; Steinberg et al., 1996) giving us confidence in our analysis even though the two species are measured by different instruments. The average ratio of the He^{2+} bulk speed relative to the H^+ bulk speed in the compressed fast wind is about 2-3% greater than that found in the ambient fast solar wind (Neugebauer, 1981; Chotoo et al., 1998). This may be due to the increased Alfvén velocity in the compressed fast wind since the difference in the H^+ and He^{2+} bulk speeds is usually equal to the Alfvén speed in the fast wind (Marsch et al., 1982).

The abundance ratio from STICS of He^{2+}/H^+, N_α/N_p, is between 0.12 - 0.18 in the velocity range 2.5 - 6.0 V_{sw} (10 - 90 keV/amu) for the fast wind. These values are almost double the values of 0.07 - 0.09 obtained at higher energies (0.5 - 2.5 MeV/amu) (Gloeckler et al., 1979; Scholer et al., 1979), and more than double the solar wind abundances, n_α/n_p, but the same as that in the suprathermal tail above 1.4 V_{sw}. The increased He^{2+}/H^+ ratio in the suprathermal tail relative to the core is due to the larger He^{2+} thermal speed and bulk velocity, as shown is Section 4.6.2.

Therefore, the H^+ and He^{2+} ions are injected from the suprathermal tail into the acceleration process. Since the abundance ratio of the source ions is the same as that of the energetic ions, then the acceleration process is independent of the ion mass-per-charge, which is proportional to the ion gyroradius.

Injection of interstellar pickup ions into shock acceleration

He^+ is unique since it is predominantly produced as a result of the pickup of photoionized interstellar helium atoms. The pickup process itself leads to a population of ions much hotter than solar wind ions; the pickup populations are thereby more readily injected into acceleration mechanisms at CIRs. For the pre-accelerated ions between 1.7 - 1.9 V_{sw}, the He^+/He^{2+} ratio is about 0.05. But, this ratio increases to ~0.15 for the post-accelerated ions between 2.5 - 6.0 V_{sw} (see Table 4.5) indicating that the injection efficiency of the pickup He^+ ions is greater than that of the solar wind ions, as previously determined at 4.5 AU by Gloeckler et al. (1994).

Gloeckler et al. (1994) examined the H^+, He^{2+}, and He^+ distribution at 4.5 AU using data from the Ulysses-SWICS instrument. They found that the He^+/He^{2+} abundance ratio was greater than 1.0 beyond 2.0 V_{sw}. However, we find that the He^+/He^{2+} values in our two cases at 1 AU are ~0.15 in the velocity range 2.5 - 6.0 V_{sw}.

From the pickup ion model of Vasyliunas and Siscoe (1976), the radial (or characteristic) distance, λ, around which the pickup ion density is maximum, is 0.7 AU for He^+. Figure 4.19 shows a plot of the normalized flux of the interstellar pickup ions as a function of distance from the Sun for three values of the speed (V_O) of the Sun relative to the interstellar neutral gas. From this plot, we find that the flux of the pickup He^+ ions at 4.5 AU (~7λ) is roughly 0.5 times the flux at 1 AU (~1λ) using the V_O = 20 km/s curve. For a spherically expanding solar wind, the density of the solar wind ions varies as $1/r^2$, where r is radial distance from the Sun; so the density of the solar wind He^{2+} ions at 4.5 AU relative to that at 1 AU is ~20 times less. Therefore the He^+/He^{2+} ratio for the CIR accelerated ions could be up to ~10 times greater at 4.5 AU resulting in a ratio of ~1.5. Hence our measurements at 1 AU are consistent with those at 4.5 AU by Gloeckler et al. (1994).

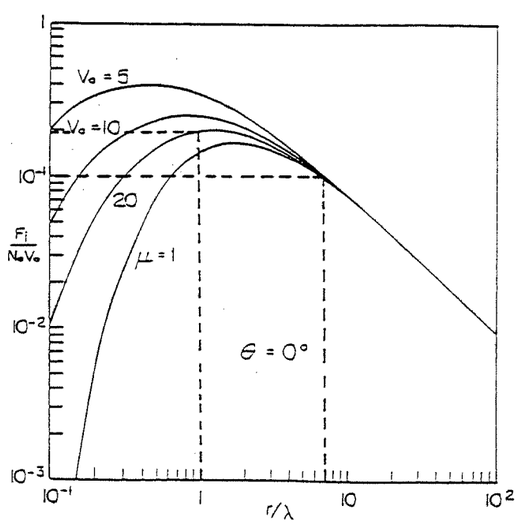

Figure 4.19. The normalized flux of interstellar ions as a function of normalized distance from the Sun is shown for three values of V_O (speed of Sun relative to the interstellar medium) taken from Vasyliunas and Siscoe (1976). For pickup He^+, the characteristic distance, λ, is equal to 0.7 AU.

4.8 Summary

In this chapter, composition and spectral measurements at 1 AU were presented for H^+, He^{2+}, and He^+ during two CIRs. These observations are unique because they are the first to give charge state information in CIRs at 1 AU in the energy range 6 - 200 keV/e.

The extended helium distribution was also shown for solar wind ions (~1 keV/amu) through energetic particles up to ~1 MeV/amu by combining data from three separate sensors on WIND (SMS-MASS, SMS-STICS, and EPACT-STEP). The distribution covered 14 orders of magnitude in phase space density. This is the first time such an extended helium distribution is being reported for CIRs at any radial distance.

The kappa distribution is important in modeling the solar wind as a source population for ions accelerated in CIRs because a single kappa function best describes the extended solar wind distribution. The core plasma He^{2+} distributions were found to have kappa values between 3 and 4. These values were one unit less than those obtained in the ambient fast solar wind (Chotoo et al., 1998) indicating that there are more particles in the tail of the distribution available for further acceleration.

The reverse shock was present at 1 AU for the first CIR resulting in power law spectra with all three species having the same power law index, as expected by the Fisk and Lee (1980) model. Two solar rotations later, the reverse shock was no longer present at 1 AU for the second CIR. The spectra for the solar wind H^+ and He^{2+} ions were exponential in character having the same characteristic velocity, also consistent with the Fisk and Lee model. For both CIRs, the model Fisk and Lee (1980) distributions fit the data reasonably well. For the second CIR, the shock location was found to be 1.2 AU.

The He^{2+}/H^+ ratio of the CIR accelerated ions between 2.5 - 6.0 V_{SW} (5 - 90 keV/amu) was 0.11 - 0.18, which is greater than twice the value of the core solar wind

plasma. The larger thermal speeds of the He^{2+} ions result in relatively more particles at higher energies that can be injected into the acceleration process. Using the kappa distributions and direct observations to determine the ratio of He^{2+}/H^{+} in the suprathermal tail, we found that the injection speed of the source ions is 1.4 V_{SW} (~850 km/s), and that the acceleration is independent of the ions' mass-per-charge. This is the first direct evidence that particles are accelerated from the suprathermal tail.

By examining the He^{+}/He^{2+} ratio for the pre-accelerated and post-accelerated ions at 1 AU, we found that the pickup He^{+} ions are more readily injected into the acceleration process than the solar wind ions.

The He^{+}/He^{2+} ratio was ~0.15 at 1 AU and is much less than the value obtained previously at 4.5 by Gloeckler et al. (1994). Between 1 - 5 AU the un-accelerated pickup ion He^{+} density is relatively constant within a factor of ~2 (Vasyliunas and Siscoe, 1976). However, the density of the spherically expanding solar wind He^{2+} ions at 4.5 AU is about 20 (4.5^2) times less than that at 1 AU. Therefore, the He^{+}/He^{2+} ratio of the accelerated ions should be greater than 1 at 4.5 AU, as observed. Hence, the relative contribution of pickup He^{+} to the seed population in CIRs increases with radial distance away from the Sun between 1 and 5 AU.

CHAPTER 5: ANISOTROPY MEASUREMENTS

5.1 Introduction

The anisotropy of a distribution of particles in the solar wind frame can give important clues to the origin, acceleration, and transport of the particles (Scholer et al., 1979b, 1983; Terasawa et al., 1985; Beeck et al., 1987; Mason et al., 1989). Particles, which have a specific angular distribution (isotropic or anisotropic) in one frame of reference, will display a different distribution when observed from another frame of reference that is moving relative to the first because the energy and arrival directions of the individual particles are different in the second frame. This is referred to as the Compton-Getting effect (Compton and Getting, 1935; Gleeson and Axford, 1968; Forman, 1970; Ipavich, 1974). In general, particle distributions measured in the spacecraft frame of reference in interplanetary space are transformed to the plasma frame, i.e., the solar wind frame, because the ions are convected away from the Sun with the solar wind creating an extra anisotropy.

Anisotropy measurements in CIRs have played a crucial role in our understanding of this phenomenon. For example, the anisotropy observations of Marshall and Stone (1978) showing sunward streaming of the energetic (MeV) ions in the solar wind frame were one of two sets of measurements that provided strong evidence for the acceleration occurring in interplanetary space rather that at the Sun. The other was the increasing ion intensity away from the Sun observed by McDonald et al. (1976).

In a recent study using anisotropy data from the EPACT-STEP instrument on WIND, Dwyer et al. (1997) found that although the accelerated particles generally streamed towards the Sun in the solar wind frame, the particle anisotropy did not line-up with the magnetic field. They applied a simple diffusion model to the data, and the anisotropy measurements fit the model very well. Their results indicated significant transport of energetic particles *across* magnetic field lines. Even though previous authors have used perpendicular transport to explain their observations (Intriligator and

Siscoe, 1994, 1995; Intriligator et al, 1995; Tsurutani et al., 1982), the work by Dwyer et al (1997) is the first to provide direct observational evidence for motion of charged particles perpendicular to magnetic field lines.

Although there has been some work done on perpendicular transport (Giacalone and Jokipii, 1996; and references therein), the mechanisms involved in this process is not well understood. The scientific community mainly concentrated on motion parallel to the magnetic field lines (Jokipii, 1971; Fisk and Lee, 1980; Smith et al., 1990) and generally ignored perpendicular transport. The strong observational evidence for perpendicular transport provided by Dwyer et al. (1997) goes against conventional thinking and has been received with some skepticism. Their results are not accounted for in the conventional CIR model, which expects particles to move primarily along the magnetic field lines (Fisk and Lee, 1980).

Since the Dwyer et al. results impinge on the fundamental concept of particle transport, it is important to first verify their observations. STICS is ideally suited to do such a job because it has angular resolution both in and out of the ecliptic plane, its energy range overlap with that of STEP, and it is also on WIND. In this chapter we present anisotropy measurements made by STICS for H^+ and He^{2+} from two of the same CIRs studied by Dwyer et al. (1997). The STICS results are compared to those from the STEP sensor.

5.2 Example of Apparent Off-field Streaming

The observations of Dwyer et al. (1997) were discussed in terms of perpendicular transport across magnetic field lines. In this section we present an example from cosmic ray theory that produces an apparent off-field component to the streaming even though the particles are diffusing primarily parallel to the magnetic field. Cosmic rays originate from beyond the solar system and have energies around 100 MeV-per-nucleon. The main transport equation used in cosmic ray transport theory to describe the motion of particles is (Parker, 1956; Gleeson and Axford, 1967)

$$\frac{\partial f_o}{\partial t} + \mathbf{U} \bullet \nabla f_o + \nabla \bullet \mathbf{S} - \nabla \bullet \mathbf{U} \frac{v}{3} \frac{\partial f_o}{\partial v} = 0 \qquad (5.1)$$

where f_o is the isotropic part of the distribution function, v is the speed of the ions, **U** is the solar wind velocity, and **S** is the streaming of the particles. If we assume that the streaming is created due to spatial gradients only, then it may be related as follows

$$\mathbf{S} = -\kappa \bullet \nabla f_o \qquad (5.2)$$

where κ is the diffusion tensor and captures the effects of spatial diffusion. If we consider diffusion only parallel to the field lines, then the diffusion coefficient becomes

$$\kappa = \kappa_{\|} \mathbf{bb} \qquad (5.3)$$

where $\kappa_{\|} = \lambda_{\|} v / 3$, in which $\lambda_{\|}$ is the parallel mean free path, and **b** is the unit vector parallel to the magnetic field. Now consider the case where the magnetic field consists of a mean component $\mathbf{b}_o$ and a variable component $\delta\mathbf{b}$, or

$$\mathbf{b} = \mathbf{b}_o + \delta\mathbf{b} \qquad (5.4)$$

The only restriction we put on $\delta\mathbf{b}$ is that it is random such that its ensemble average is zero, or

$$\langle \delta\mathbf{b} \rangle = 0 \qquad (5.5)$$

Substituting equations 5.3 and 5.4 into 5.2 and taking an ensemble average, we get

$$\langle \mathbf{S} \rangle = -\kappa_{\|} \left\langle (\mathbf{b}_o \mathbf{b}_o) \bullet \nabla f_o + (\delta\mathbf{b}\delta\mathbf{b}) \bullet \nabla f_o \right\rangle \qquad (5.6)$$

The second term in equation 5.6 indicates that the variations in the magnetic field can significantly alter the streaming of the ions away from the mean magnetic field direction.

This example may or may not be applicable to CIR ions since a detailed treatment of the streaming and the field fluctuations has not been worked out, however, it illustrates that there can be an apparent off-field component even though the particles are diffusing along the field.

5.3 Compton-Getting Transformation

The Compton-Getting transformation involves a simple Galilean transformation of the ion velocity and distribution function in the spacecraft frame of reference to the solar wind reference frame. The method used in our study does not require the ion velocities to be much greater than the solar wind velocity. The measurements made in the spacecraft frame are given in terms of the geocentric solar ecliptic (GSE) coordinate system, which is centered on the Earth and rotates around the Sun. The spherical GSE coordinates has its radial component, v, pointing away from the Earth, the polar angle, θ, is measured relative to the north axis (ecliptic pole) perpendicular to the ecliptic plane with $\theta = 90^\circ$ being in the ecliptic plane, and the azimuthal angle, ϕ, is measured in the ecliptic plane with $\phi = 0^\circ$ pointing towards the Sun and $\phi = 270^\circ$ pointing in the direction of the Earth's motion around the Sun.

As mentioned in Section 2.3, the STICS sensor consists of three identical telescopes stacked vertically in the instrument. Telescope 1 looks above the ecliptic plane in the polar direction from $\theta = 10.5 - 63.5^\circ$, telescope 2 from $\theta = 63.5 - 116.5^\circ$, and telescope 3 from $\theta = 116.5 - 169.5^\circ$. The spacecraft spin axis is always perpendicular to the ecliptic plane, and as the spacecraft spins, the instrument is swept through the azimuthal direction. One complete spin is divided-up into sixteen 22.5° azimuthal sectors labeled 0-15 (see Figure 2.5).

From the pre-launch calibration done at the University of Bern, Switzerland, the effective angular opening for each telescope is are given in Table 5.1 (see Appendix A.2). The polar angles for telescopes 1, 2, and 3 are centered at $\theta = 37^\circ$, 90°, and 143°, respectively.

For a selected time period, the velocity distribution function (phase space density), $f(\mathbf{v})$, defined as the number of particles in an infinitesimal coordinate-space volume d^3r and an infinitesimal velocity-space volume d^3v, may be determined for each azimuthal sector and telescope as measured in the spacecraft frame of reference

Table 5.1. Polar and azimuthal acceptance angles for each telescope.

	Acceptance Angle (°)	
Telescope	**Polar, $\Delta\alpha$**	**Azimuthal, $\Delta\beta$**
1	31 ± 1	3.0 ± 0.2
2	32 ± 1	3.0 ± 0.2
3	30 ± 1	3.0 ± 0.2

(Section 3.4). Each data point in the distribution represents the average value over the normalized velocity bin, and over the azimuthal and polar directions. If we consider a distribution in the spacecraft frame, $f(\mathbf{v})$, with the solar wind velocity being $\mathbf{u}$, then the ion velocity in the solar wind frame, $\mathbf{v}_{sw}$, and the distribution in the solar wind frame, $f_{sw}(\mathbf{v}_{sw})$ are given by:

$$\mathbf{v}_{sw} = \mathbf{v} - \mathbf{u} \tag{5.7}$$

and

$$f_{sw}(\mathbf{v}_{sw}) = f(\mathbf{v}) \tag{5.8}$$

Equation 5.8 is derived simply from the conservation of particles from one frame of reference to the other (Forman, 1970). Since the measured distribution in the

spacecraft frame, f_{sc}, is an average value over the instrument opening and over the azimuthal sector, then

$$f_{sc}(v_i,\theta_i,\phi_i) = \frac{1}{\Delta\phi}\int_{\phi_1}^{\phi_2} d\phi * \frac{1}{\Delta\Omega}\int_{-\alpha}^{+\alpha} \sin\theta \, d\theta \int_{-\beta}^{+\beta} d\phi \, f_{sw}(\vec{v}-\vec{u}) \qquad (5.9)$$

where $\Delta\phi$ is the angular width of the azimuthal sector in radians, $\Delta\Omega$ is the angular acceptance of the telescope's opening in steradians, $\Delta\alpha$ is the polar acceptance of the telescope opening, and $\Delta\beta$ is the azimuthal acceptance of the telescope opening. The first integral from the left represents the averaging over the azimuthal sector as the spacecraft spins, and the second double integral represents the averaging over the polar and azimuthal acceptance angles of the telescope opening. Note that there is no integration over the width of the speed bin (dv) because the velocity bins are relatively small with $\Delta v/v \approx 0.03$.

To simplify the calculations, the measured average distribution was treated as a representative value for all points in that particular azimuthal sector and telescope at the given velocity. Using the center of the azimuthal sector for the ϕ_i angle and the center of the telescope for the θ_i angle, that single discrete data point is then transformed to the solar wind frame. No integrations are performed over the azimuthal sector nor over the opening of the telescope reducing equation 5.9 to

$$\tilde{f}_{sc}(v_i,\theta_i,\phi_i) = \tilde{f}_{sw}(\vec{v}_i - \vec{u}) \qquad (5.10)$$

Once the data are transformed to the solar wind frame, the distribution function data points are then rebinned into sixteen azimuthal sectors, ϕ_{isw}, and into velocity bins, v_{isw}, the same as those used in the spacecraft frame. If the velocity bin for a given sector receives more than one data point, which may be from different telescopes (polar direction), then the average value is obtained for that bin. This method averages

over the data from the 3 polar directions. There are now sixteen separate spectra one for each sector.

Next, the flux, J, is calculated for a specific velocity range for each sector in the solar wind frame using the following equation:

$$J = nv$$
$$J = \int_{v_1}^{v_2} dv \, v^3 f(v) \qquad (5.11)$$

where n is density. Since our data points are discrete, then for a specific energy range

$$J_{swi} = \sum_j \Delta v_{swj} \, v_{swj}^3 \, \bar{f}_{swij}\left(v_{swj}\right) \qquad (5.12)$$

where i indicates sector, j indicates velocity bin, and Δv is the size of the velocity bin.

In order to determine the anisotropy, the following equation (Zwickl and Webber, 1976) is used

$$\begin{aligned} J_{sw} = a_0 + a_1\cos\phi_{sw} + b_1\sin\phi_{sw} + a_2\cos(2\phi_{sw}) \\ + b_2\sin(2\phi_{sw}) + a_3\cos(3\phi_{sw}) + b_3\sin(3\phi_{sw}) \end{aligned} \qquad (5.13)$$

where a_n, and b_n are all constants. Equation 5.13 may be rewritten as

$$J_{sw} = c_0 + c_1\cos(\phi_{sw}-\phi_1) + c_2\cos(2\phi_{sw}-\phi_2) + c_3\cos(3\phi_{sw}-\phi_3) \qquad (5.14)$$

where $c_0 = a_0$ $\quad a_n = c_n\cos\phi_n$ $\quad b_n = c_n\sin\phi_n$

$$\Rightarrow \quad c_n = \sqrt{a_n^2 + b_n^2} \qquad \phi_n = \tan^{-1}\left(\frac{b_n}{a_n}\right) \quad \text{for } 1 \le n \le 3 \qquad (5.15)$$

From equation 5.14, the magnitude and direction of the anisotropy vector, ξ_n, for the *nth* harmonic relative to the isotropic term are c_n/c_0 and ϕ_n, respectively. The streaming of the particles is typically obtained from the first harmonic term, i.e., ξ_1 (Terasawa et al., 1985; Dwyer et al., 1997). The constant parameters (a_n and b_n) can be determined by substituting the sixteen flux values, J_{swi}, and their corresponding angles, ϕ_{swi}, into equation (5.13) and using the method of least squares (Bevington and Robinson, 1992), which minimizes the χ^2 with respect to each parameter.

$$\chi^2 = \frac{1}{N-\nu}\sum_{i}^{N}\left(\frac{J_{swi} - J_{sw}}{\sigma_i}\right)^2 \qquad (5.16)$$

where N (equal to 16) is the number of data points, ν is the number of parameters (equal to 7 in this case), and σ_i is the error associated with each data point.

The anisotropy was determined over the velocity range for which STICS had the best data coverage. The two velocity ranges used for H^+ are 3.5 - 5.0 V_{SW} and 5.0 - 8.0 V_{SW}, and the two used for He^{2+} are 2.0 - 3.0 V_{SW} and 3.0 - 5.0 V_{SW}.

Figure 5.1 shows pie plots of the proton anisotropy data. The flux is plotted for each of the sixteen azimuthal *flow* directions for a given velocity range. The Sun is to the left in the +x direction as shown, the Earth is to the right in the -x direction, and the angles are measured in the counterclockwise direction from the +x-axis. The anisotropy and magnetic field directions are indicated with arrows. As explained previously, the magnitude, $|\xi|$, and direction, ξ_ϕ, of the anisotropy are defined in equation 5.14, and they are equal to c_1/c_0 and ϕ_1, respectively. For each time interval, the magnetic field data were taken every 3 minutes from the WIND-MFI key parameter data. The 3-minute values were then averaged over the entire interval, and the uncertainty represents one standard deviation from the mean value. Also, the average solar wind velocity in cartesian GSE coordinates was obtained from the WIND-SWE instrument.

5.3.1 Analysis Check

In order to check our Compton-Getting transformation, we used our technique to analyze an upstream ion event occurring on April 20, 1996. Previous authors have shown that the anisotropies in upstream ions events are field aligned in the solar wind frame (Scholer et al., 1979b, Terasawa et al., 1985). Figure 5.1 and 5.2 show the STICS H^+ and He^{2+} results. In all four cases the anisotropy direction is equal to the mean magnetic field direction within one standard deviation, as expected.

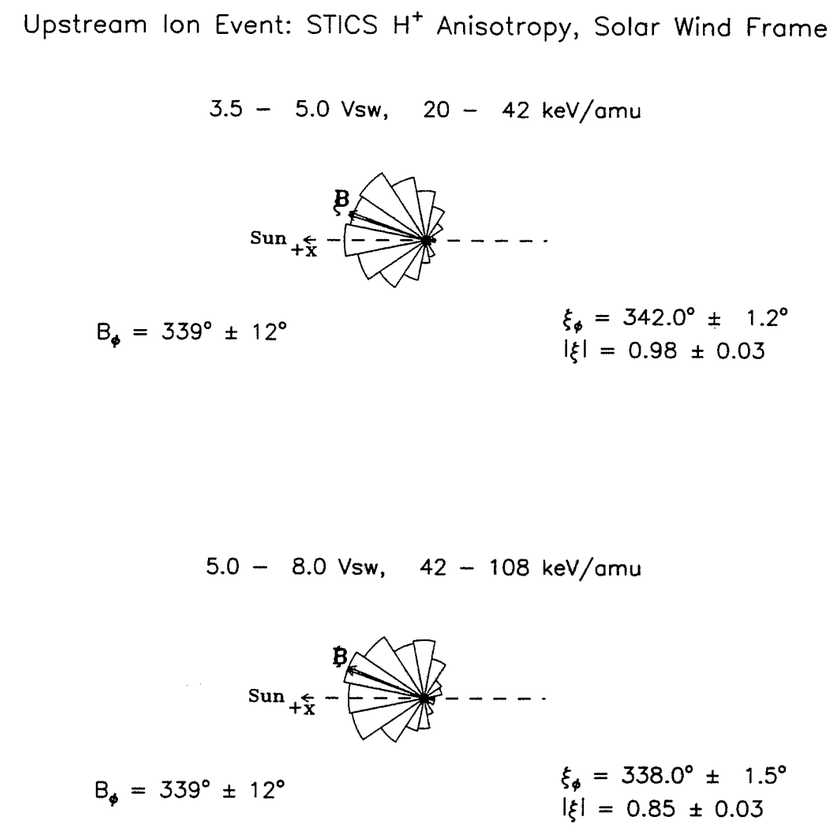

Figure 5.1. STICS H^+ anisotropy for the *upstream ion event* occurring on April 20, 1996 from 13:00 - 17:00 UT. In the solar wind frame, the ions stream towards the Sun essentially along the mean magnetic field direction.

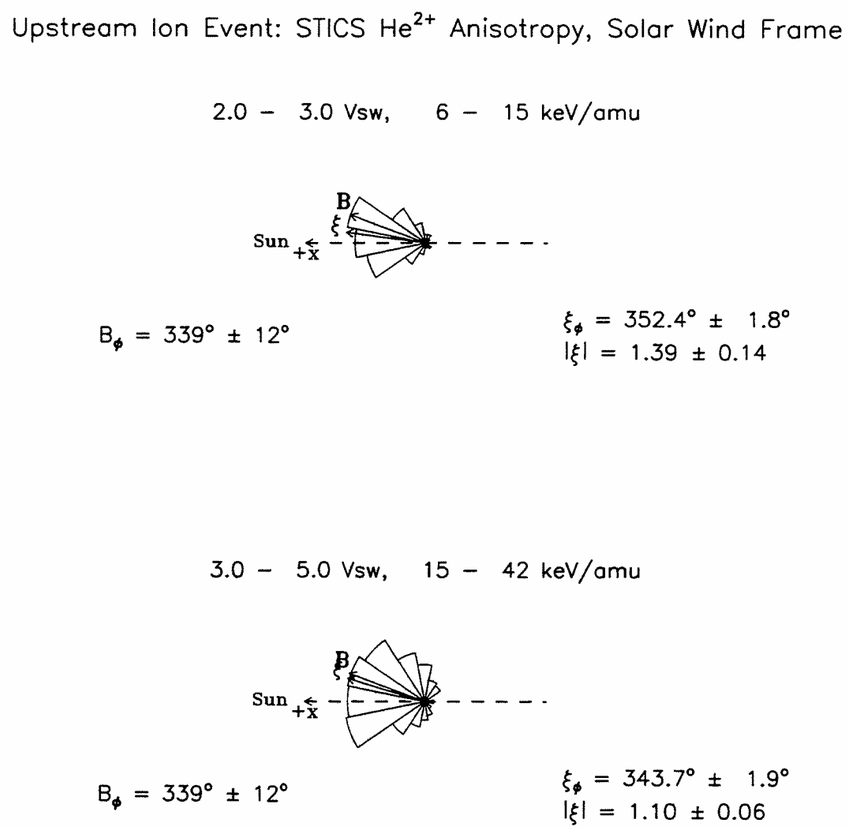

Figure 5.2. STICS He^{2+} anisotropy for the *upstream ion event* occurring on April 20, 1996 from 13:00 - 17:00 UT. In the solar wind frame, the ions stream towards the Sun essentially along the mean magnetic field direction.

5.4 CIR Anisotropies

We now apply our Compton-Getting transformation to CIRs. We examine the same two CIRs that were discussed in Chapter 4. For the first CIR, April 6-7, 1995, its reverse shock was present at 1 AU. Two solar rotations later, the reverse shock is no longer present for the CIR occurring between May 29-31, 1995. These two CIRs were also studied by Dwyer et al. (1997). The rectangular bars in the top panel of Figures 5.3 and 5.4 indicate the time intervals over which the anisotropies were determined. Both time periods were in the compressed fast wind region of the CIR. The anisotropy data for H^+ and He^{2+} are shown in Figures 5.5 - 5.8 for the two CIRs, and the results are given in Table 5.2.

For CIR 1, the H^+ ions were streaming in the opposite direction of the magnetic field away from the Sun, but the He^{2+} anisotropies pointed towards the Sun. However, both anisotropies deviated from the mean magnetic field direction, H^+ by ~40° and He^{2+} by ~65°. These differences are significant because they are greater than the sum of the uncertainties on the anisotropy and magnetic field directions.

For CIR 2, both H^+ and He^{2+} were streaming towards the Sun with deviations of ~25° and ~30° from the mean magnetic field direction, respectively. Here again these differences are significant. The magnitude of the H^+ anisotropy is much greater in CIR 2 than in CIR 1. The same is true for He^{2+} indicating that the distributions in CIR 1 are more isotropic than those in CIR 2.

In order to compare the STICS and STEP anisotropies, the H and He data from both instruments are shown together for CIR 1 and CIR 2 in Figures 5.9 and 5.10. The anisotropies from both instruments agree reasonably well. The difference in the proton anisotropies between the two sensors is due to an energy dependence. For example, in Figure 5.10, the anisotropy directions from STICS and STEP are on either side of the magnetic field because of the difference in energy. This is clearly seen in the STEP data (Figure 5.11). As the energy increases up to ~388 keV (0.388 MeV),

the anisotropy direction points further and further away from the Sun, then remains fairly constant at the higher energies.

Table 5.2. STICS H^+ and He^{2+} anisotropy results in the solar wind frame for CIR 1 and 2.

CIR	Ion	Speed (V_{sw})	$\langle B_\phi \rangle$ (°)	$\xi_{1\phi}$ (°), $\lvert\xi_1\rvert$	Energy (keV/amu)
1	H^+	3.5 - 5.0	306 ± 16	84.5 ± 11.4 0.25 ± 0.04	22 - 46
1	H^+	5.0 - 8.0	306 ± 16	86.3 ± 11.2 0.28 ± 0.05	46 - 118
1	He^{2+}	2.0 - 3.0	306 ± 16	6.8 ± 5.3 0.66 ± 0.15	7 - 16
1	He^{2+}	3.0 - 5.0	306 ± 16	20.4 ± 9.7 0.37 ± 0.09	16 - 46
2	H^+	3.5 - 5.0	318 ± 13	337.0 ± 3.5 0.70 ± 0.06	26 - 53
2	H^+	5.0 - 8.0	318 ± 13	347.4 ± 5.0 0.55 ± 0.06	53 - 136
2	He^{2+}	2.0 - 3.0	318 ± 13	350.2 ± 3.5 1.28 ± 0.23	8 - 19
2	He^{2+}	3.0 - 5.0	318 ± 13	345.3 ± 4.1 0.90 ± 0.11	19 - 53

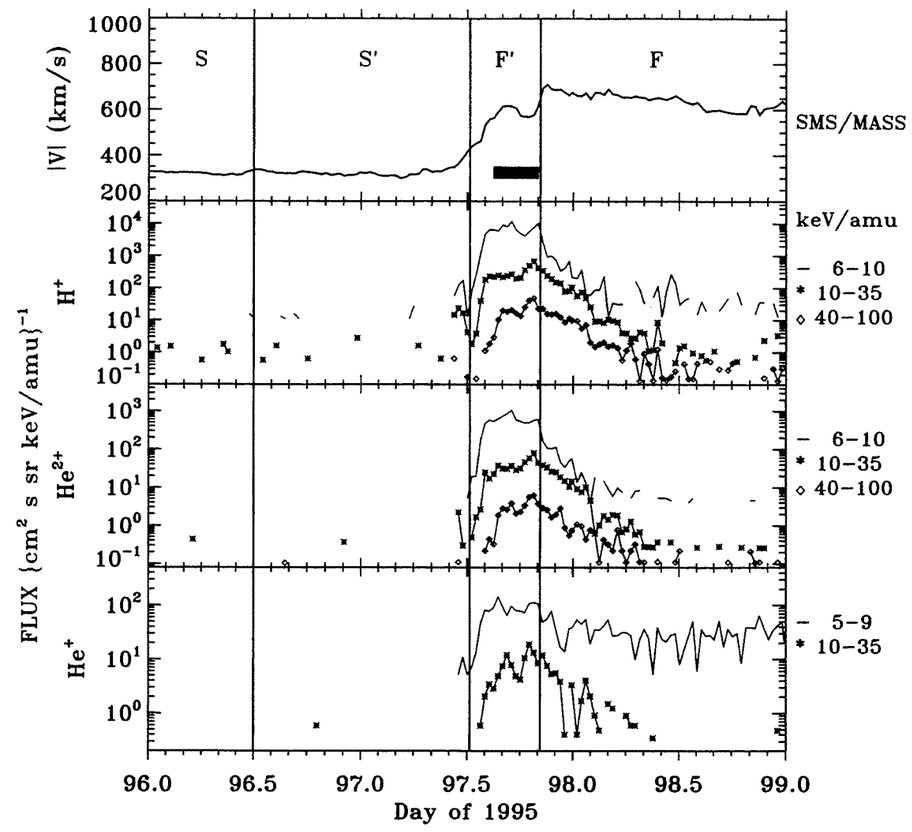

Figure 5.3. STICS omni-directional fluxes for CIR 1 showing the selected time period, April 7, 1995, 15:00 - 20:00.

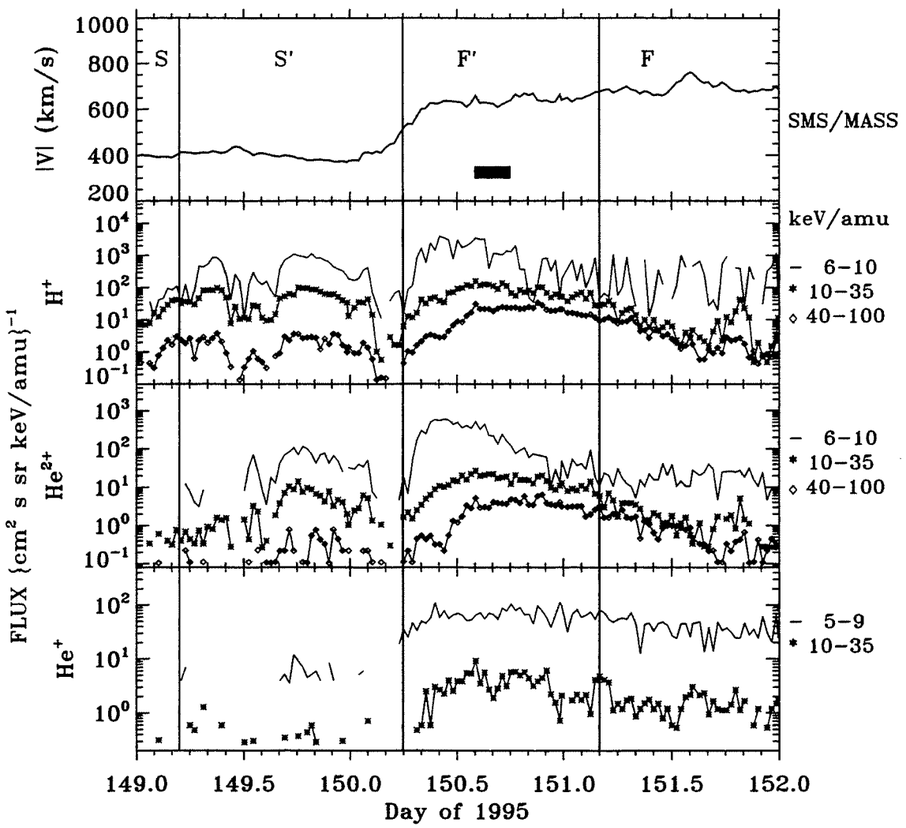

Figure 5.4. STICS omni-directional fluxes for CIR 2 showing the selected time period, May 30, 1995, 14:00 - 18:00 UT.

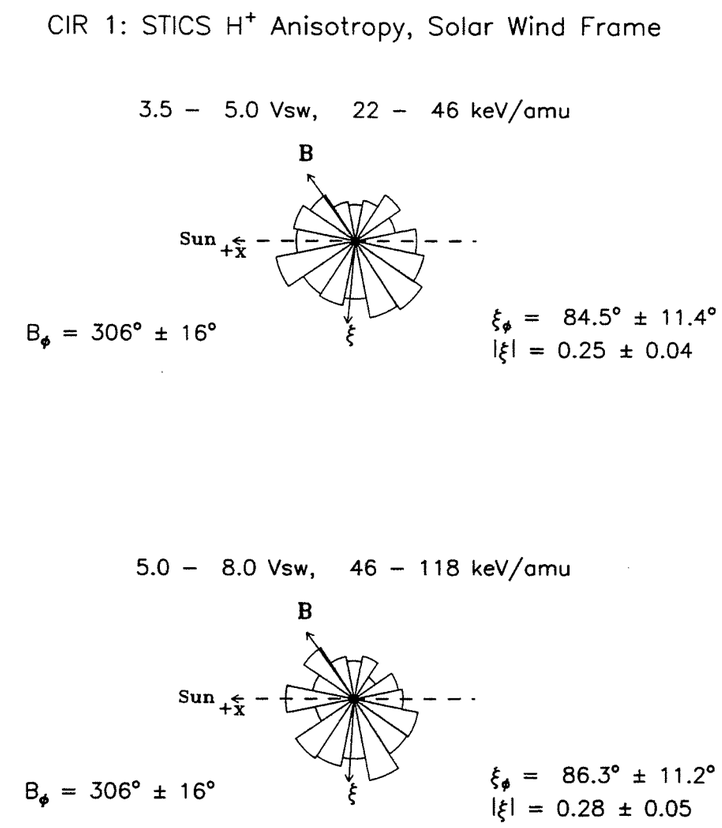

Figure 5.5. STICS H^+ anisotropy in the solar wind frame for CIR 1, April 7, 1995 15:00 - 20:00 UT. The H^+ ions stream *away from* the Sun at an angle of ~40° away from the mean magnetic field direction.

CIR 1: STICS He^{2+} Anisotropy, Solar Wind Frame

2.0 – 3.0 Vsw, 7 – 16 keV/amu

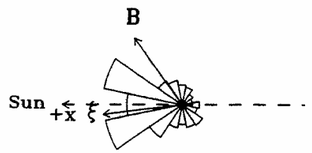

B_ϕ = 306° ± 16°

ξ_ϕ = 6.8° ± 5.3°
$|\xi|$ = 0.66 ± 0.15

3.0 – 5.0 Vsw, 16 – 46 keV/amu

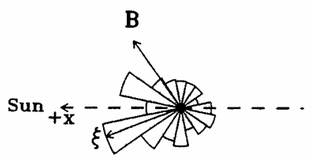

B_ϕ = 306° ± 16°

ξ_ϕ = 20.4° ± 9.7°
$|\xi|$ = 0.37 ± 0.09

Figure 5.6. STICS He^{2+} anisotropy in the solar wind frame for CIR 1, April 7, 1995 15:00 - 20:00 UT. The He^{2+} ions stream *towards* the Sun at an angle of ~65° away from the mean magnetic field direction.

CIR 2: STICS H^+ Anisotropy, Solar Wind Frame

3.5 – 5.0 Vsw, 26 – 53 keV/amu

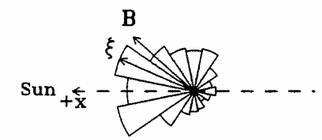

B_ϕ = 318° ± 13°

ξ_ϕ = 337.0° ± 3.5°
$|\xi|$ = 0.70 ± 0.06

5.0 – 8.0 Vsw, 53 – 136 keV/amu

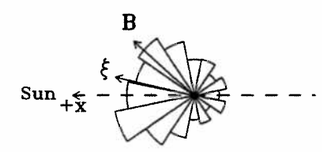

B_ϕ = 318° ± 13°

ξ_ϕ = 347.4° ± 5.0°
$|\xi|$ = 0.55 ± 0.06

Figure 5.7. STICS H^+ anisotropy in the solar wind frame for CIR 2, May 30, 1995 14:00 - 18:00 UT. The H^+ ions stream towards the Sun at an angle of ~25° away from the mean magnetic field direction.

CIR 2: STICS He^{2+} Anisotropy, Solar Wind Frame

2.0 – 3.0 Vsw, 8 – 19 keV/amu

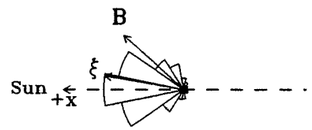

B_ϕ = 318° ± 13°

ξ_ϕ = 350.2° ± 3.5°
$|\xi|$ = 1.28 ± 0.23

3.0 – 5.0 Vsw, 19 – 53 keV/amu

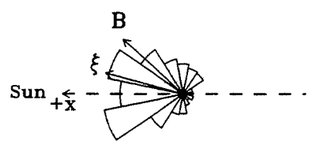

B_ϕ = 318° ± 13°

ξ_ϕ = 345.3° ± 4.1°
$|\xi|$ = 0.90 ± 0.11

Figure 5.8. STICS He^{2+} anisotropy in the solar wind frame for CIR 2, May 30, 1995 14:00 - 18:00 UT. The He^{2+} ions stream towards the Sun at an angle of ~30° away from the mean magnetic field direction.

STICS **STEP**

Protons

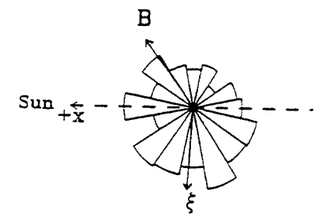

46 - 118 keV/amu

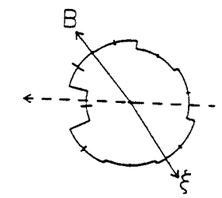

111 keV/amu

Helium

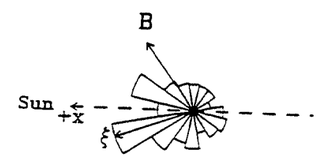

16 - 46 keV/amu

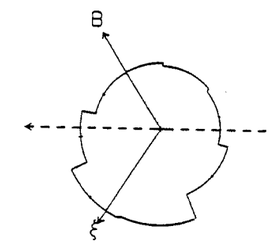

62 keV/amu

Figure 5.9. The STICS and STEP H and He anisotropy (ξ) data are shown for similar energy ranges during CIR 1. The STICS data are plotted to the left, and the corresponding STEP data are to the right. The time interval was 15:00 - 20:00 UT on April 7, 1995 for both sensors. The STICS proton and helium anisotropies agree reasonably well with those from STEP. Both data sets show significant deviation away from the magnetic field (B). The difference in the proton data between the two data sets is due to an energy dependence.

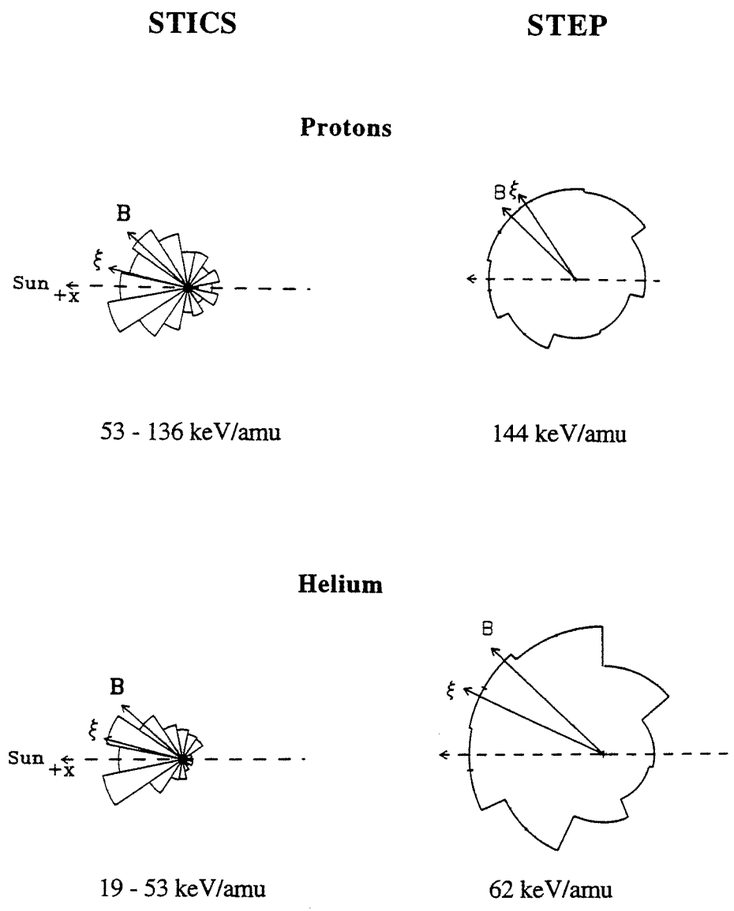

Figure 5.10. The STICS and STEP H and He anisotropy (ξ) data are shown for similar energy ranges during CIR 2. The STICS data are plotted to the left, and the corresponding STEP data are to the right. The STICS time interval was 14:00 - 18:00 UT, and the STEP time interval was 12:00 - 20:00 UT, both on May 30, 1995. The STICS anisotropy for both species agree reasonably well with those from STEP showing significant deviation away from the magnetic field (B). The difference in the proton data between the two data sets is due to an energy dependence.

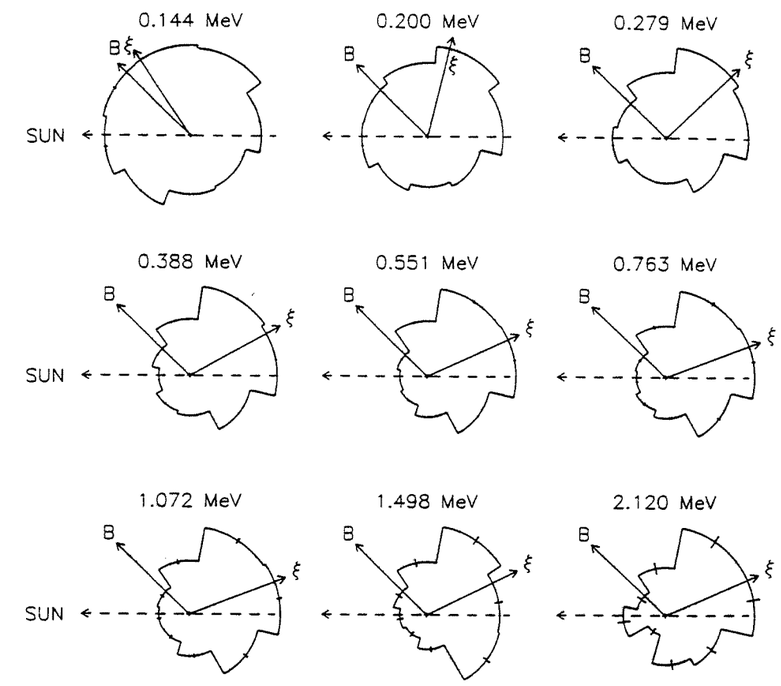

Figure 5.11. STEP proton anisotropies are shown at different energies for CIR 2. As the energy increases up to ~388 keV (0.388 MeV), the anisotropy direction points further and further away from the Sun, then remains fairly constant at the higher energies.

5.5 Discussion

Location of acceleration

With the reverse shock present at 1 AU for CIR 1, the ions are naturally accelerated by the shock. The ion distributions are more omnidirectional in this case. With the absence of the reverse shock at 1 AU for CIR 2, the Fisk and Lee (1980) model expects the observed energetic ions to have originated from shock acceleration at some location beyond 1 AU. The sunward streaming of both the H^+ and He^{2+} confirms this. The exponential nature of the spectra and the determination of the shock location at 1.17 AU in Chapter 4 also support this expectation.

Difference in H^+ and He^{2+} Streaming

It is not yet fully understood why the anisotropy of the H^+ and He^{2+} are different for CIR 1. Streaming towards (away from) the Sun implies that the intensity of the ions increase (decrease) with radial distance. Therefore, the sunward streaming of the He^{2+} indicates a positive radial gradient, agreeing with previous observations at higher energies (McDonald et al., 1976; Marshall and Stone, 1978). However, the outward flow of the H^+ ions is not expected.

The difference in streaming is not energy dependent because it is also observed at higher energies by STEP. In the previous chapter (Section 4.6), we found that the acceleration process was independent of the ion mass-per-charge from composition measurements. This means that the different gyroradii are not important since the ion gyroradius is proportional to its mass-per-charge.

One possible explanation may have to do with the injection of the ions. The solar wind He^{2+} ions may be more easily injected beyond 1 AU, whereas the solar wind H^+ ions may be more readily injected at 1 AU. However, the role of the pickup H^+ ions in the source population increases with radial distance. Since the pickup ions are hotter than solar wind ions, they would have a greater injection efficiency into the

acceleration process, as seen in Section 4.7. Therefore, the combined pickup and solar wind H^+ source population is not expected to have a lower injection efficiency further out. Thus, the outward flow of the H^+ remains a puzzle.

Transport across field lines

For CIR 1 and 2, both the STICS and STEP H and He data show significant deviations in the anisotropy away from the mean magnetic field direction in agreement with the STEP observations of Dwyer et al. (1997). Dwyer et al. (1997) applied a simple diffusion model to their observations and found significant transport across field lines. However, as indicated by the example in Section 5.2, this apparent off-field streaming may be a result of the field fluctuation, which is more prominent in CIRs because of the increased turbulence created by the collision of the slow and fast winds. If the field is fluctuating more rapidly than the allowable time resolution of the particle instrument, then the anisotropy measurements may be skewed.

A better understanding of the magnetic field fluctuations in CIRs may be the key to interpreting the observed off-field component. But, the work of Dwyer et al. (1997) showing perpendicular transport is still a strong possibility.

5.6 Summary

A simple Galilean conversion was used to transform the H^+ and He^{2+} ion velocities and distribution function from the spacecraft frame to the solar wind frame. The Compton-Getting transformation method was first checked by determining the anisotropies in an upstream ion event, and the results were similar to those obtained previously.

The transformation was then applied to CIRs. The anisotropy measurements supported conclusions made in Chapter 4 from spectral measurements concerning the location of the shock acceleration.

The anisotropy directions showed significant deviations away from the mean magnetic field direction in agreement with STEP anisotropies. Therefore, the STICS anisotropy results are similar to the observations of Dwyer et al. (1997).

CHAPTER 6: CONCLUSIONS

In this dissertation we presented composition, spectral, and anisotropy measurements of H^+, He^{2+}, and He^+ in two corotating interaction regions (CIRs) at 1 AU using the SMS-STICS instrument on WIND. The results presented in this dissertation are important because they address some of the current concerns in the study of CIRs. These measurements are unique because of the STICS energy range, 6 - 200 keV/e, and because they are the first charge state measurements for CIRs at 1 AU. The energy range of STICS allowed us to examine both the source and accelerated ion populations simultaneously. The STICS charge state information allowed us to distinguish between the solar wind He^{2+} ions from the pickup He^+ ions.

The different CIR boundaries were identified in the standard way as described by Richardson et al. (1993) using the solar wind plasma data from WIND-SWE and magnetic field data from WIND-MFI. The forward-reverse shock pair that bound a CIR typically develop beyond 2 AU. However, the first CIR was unusual in that its reverse shock was present at 1 AU. Two solar rotations later, the reverse shock was no longer present for the second CIR examined.

By combining data from the three separate sensors on WIND (SMS-MASS, SMS-STICS, and EPACT-STEP), the extended helium distribution was shown for solar wind ions (~1 keV/amu) through energetic particles up to ~1 MeV/amu. The distribution covered 14 orders of magnitude in phase space density. This is the first time such an extended helium distribution is being reported for CIRs at any radial distance.

The solar wind He^{2+} velocity distribution function from ~0.8 - 1.6 V_{SW} were fit to a single kappa function using data from SMS-MASS and STICS. The kappa values were between 3 - 4, which is one unit less than that measured in the ambient fast solar wind by Chotoo et al. (1998). This means that the higher energy tail of the solar wind

distribution contains more particles resulting in a greater number being available for CIR acceleration.

During the first CIR with its reverse shock present at 1 AU, the velocity distribution functions for the accelerated H^+, He^{2+}, and He^+ ions beyond 2 V_{SW} all exhibited power law spectra and had the same power law index as expected from the conventional CIR model of Fisk and Lee (1980). When the reverse shock was no longer present at 1 AU for the second CIR, the spectra for both H^+ and He^{2+} were exponential in nature with the same characteristic velocity for both ions. This is consistent with ions being accelerated beyond 1 AU and traveling back towards the Earth suffering adiabatic deceleration in the process as explained in the CIR model.

The He^{2+}/H^+ ratio of the CIR accelerated ions between 2.5 - 6.0 V_{SW} (5 - 90 keV/amu) was 0.11 - 0.18, which is between 2 - 4 times greater than the solar wind values. From direct measurements and using a single kappa function to describe the solar wind distribution up to 2.0 V_{SW}, we found that the larger bulk and thermal speeds of the He^{2+} ions result in relatively more He^{2+} particles in the suprathermal tail. The He^{2+}/H^+ ratio for the accelerated ions was the same as that in the suprathermal tail beyond 1.4V_{SW} (~850 km/s). Therefore, we concluded that the H^+ and He^{2+} ions are injected equally into the CIR acceleration process out of the suprathermal tail of the solar wind, and that the acceleration mechanism is independent of the charge to mass ratio of the ions, consistent with the Fisk and Lee (1980) model. These measurements provide the first direct evidence that particles are accelerated from the suprathermal tail of the solar wind.

The pickup He^+ ions are more readily injected into acceleration mechanisms at CIRs. The He^+/He^{2+} ratio is about 3 times greater for the post-accelerated ions between 2.5 - 6.0 V_{SW} than for the pre-accelerated ions between 1.7 - 1.9 V_{SW} indicating that the injection efficiency of the pickup He^+ ions is greater than that of the solar wind ions.

The He^+/He^{2+} ratio of the accelerated ions was ~0.15 at 1 AU as measured by STICS, but the value obtained by Gloeckler et al. (1994) at 4.5 AU was greater than 1.0. This is a direct reflection of the changes in the source population with radial distance, r, away from the Sun. The density of un-accelerated pickup He^+ is relatively constant within a factor of 2 between 1 and 5 AU (Vasyliunas and Siscoe, 1976). However the density of the spherically expanding solar wind ions decreases as $1/r^2$, and the He^+/He^{2+} ratio of the source ions is expected to be ~10 times greater at 4.5 AU than at 1 AU resulting in a He^+/He^{2+} ratio of greater than 1.0 for the accelerated ions. Hence the pickup He^+ ions become more dominant in the source population with increasing radial distance relative to the solar wind He^{2+} ions.

The anisotropies of the STICS H^+ and He^{2+} ions were determined in the solar wind frame. With the reverse shock present at 1 AU for CIR 1, the distributions were found to be more isotropic than those in the absence of the shock, indicative of particles being accelerated at 1 AU. With the reverse shock no longer present at 1 AU during CIR 2, both the H^+ and He^{2+} distributions were highly anisotropic and showed sunward streaming. This indicated that particles were being accelerated at some point beyond 1 AU, consistent with spectral measurements explained earlier. With the reverse shock present, the He^{2+} ions streamed towards the Sun, as expected, while the H^+ flowed away from the Sun. This is not yet fully understood.

The anisotropy directions for both the H^+ and He^{2+} ions showed significant deviations from the mean magnetic field direction. These anisotropy results agreed with those from the EPACT-STEP instrument. Dwyer et al. (1997) used EPACT-STEP anisotropy data to provide strong observational evidence for transport of particles across magnetic field lines. It is possible that the increased magnetic field fluctuations in CIRs give the appearance of an off-field component even though the particles may in fact be moving parallel to the field.

At this point we know for certain that there is an off-field component in the streaming of the ions; it is unclear as to what exactly is causing it. The key lies in the magnetic field fluctuations, but motion across field lines cannot be ruled out. The generally accepted CIR model (Fisk and Lee, 1980) may have to be modified to include perpendicular transport.

The results presented in this dissertation impact directly on diffusive shock theory (e.g., Fisk and Lee, 1980). The equations that govern particle motion in diffusive theory are generally valid for particles that can move freely throughout the plasma, e.g., MeV particles. The lower energy particles measured by STICS cannot move about the plasma so easily. For diffusive shock acceleration to be effective, ions must be able to jump across the shock many times. Typically this injection speed, in the *solar wind frame*, is larger than the solar wind speed. However, we see that particles are injected into the acceleration mechanism at ~0.4 V_{SW} in the solar wind frame. A full theoretical understanding of the injection is lacking. Thus far, the observations suggest that the role of cross-field diffusion also needs to be better addressed in the theory.

In closing, the STICS observations are important to the study of CIRs because of the new charge state information given at a relatively unexplored energy range. The results added insight to current concerns on seed population, injection, acceleration, and transport. Some of the observations can be accounted for by theory; other observations cannot be fully explained at this time. Now that these new observations are available, more theoretical work is needed to get a better understanding of the big picture.

APPENDIX A: CALIBRATION DATA ANALYSIS

A.1 Calibration

In 1993 STICS was calibrated at the NASA Goddard Space Flight Center (GSFC) in Greenbelt, Maryland, and at the Physikalisches Institut, Universität Bern, Bern, Switzerland. A full description of the Bern accelerator facility is given by Ghielmetti et al. (1983) and by Steinacher et al. (1995). The instrument was placed in a vacuum chamber and the pressure reduced to less than 10^{-5} mmHg. Beams of different ions were accelerated to different energies by an ion accelerator then aimed at the entrance aperture of the sensor. First, the beam intensity and profile were carefully determined by the available Faraday cups and channeltrons. Then the various instrument rates and PHA data were recorded. At Goddard, tests were done with beams of H^+, He^+, C^+, C^{2+}, N^+, N^{2+}, O^{2+}, and Ne^+. At Bern, beam measurements were done for H^+, He^+, C^+, O^+, Ne^+, Ne^{3+}, Ar^{4+}, and Kr^{5+}. The combined calibration covered deflection voltage steps (DVS) 0, 2, 4, 8-10, 12-20, and 23-31. The majority of the testing was done on the middle time-of-flight telescope, but since all three telescopes are nearly identical, the results of telescope 2 should also apply to telescopes 1 and 3, at least to first order.

A total of three different accelerators were used in this calibration, two at GSFC and one at Bern. At GSFC, the first (small) accelerator voltage went up to 110 kV. The second (big) accelerator, which is normally used to accelerate ions to the MeV range, was used to produce beam energies from 60-230 keV/e. The Bern accelerator had a maximum acceleration voltage of 60 kV. The combined calibration covered the entire E/Q range of STICS. The difference in the beam characteristics between GSFC and Bern required the sensor to be operated at higher MCP levels at Bern in order to get similar TOF efficiencies at the same energies. At GSFC the beams were narrow (~2 cm in diameter), and more focused. The intensity fluctuated making it difficult to get a good measurement of the beams' incident flux. The accelerator at Bern produced broad

(~25 cm diameter), uniform beams with narrow energy passbands. An accurate measurement of the beam's flux was obtained using a Faraday cup. With the combined information from Goddard and Bern, we were able to produce reasonable results.

At the Goddard small accelerator, the middle telescope was calibrated with the ion beams entering near its center in the polar direction. The instrument's position was then adjusted in the azimuthal direction so as to give the maximum response in the rates. With the deflection voltage fixed, beams of H^+ ions with E/Q values above and below the nominal entrance value were directed at the sensor. The E/Q value that gave the peak response in the double coincidence rate was then used to obtain efficiencies and PHA data for all ions. The MCP levels for both the front and rear SEDA (secondary electron detector assembly) were 155 (~1750 V), and the TOF housing voltage was set to level 220. All three solid state detectors (SSD) were set to threshold level 8 (~30 keV). Spot checks were done on the side telescopes.

For the GSFC big accelerator, physical limits of the vacuum chamber restricted the calibration to one entrance point in the middle telescope (i.e., there were no position adjustments possible). The instrument settings were the same as those used at the small accelerator.

At Bern, angle scans were done with the deflection voltage fixed. This involved rotating the sensor in the polar or azimuthal (alpha or beta) direction so that the particles enter at different angles, Figure A.1. In some cases one angle was fixed while the other angle was changed with the beam energy held constant. In other cases the beam energy was rapidly varying over a fixed energy interval (Beam Wobble). These angle scans covered all three telescopes. The MCP level was 175 (~1975 V) for both front and rear SEDA and the TOF housing set to level 225. The threshold levels for SSD1, 2, 3 were 8, 7, 7 respectively for all ions, except for He and Ne which used level 8 only.

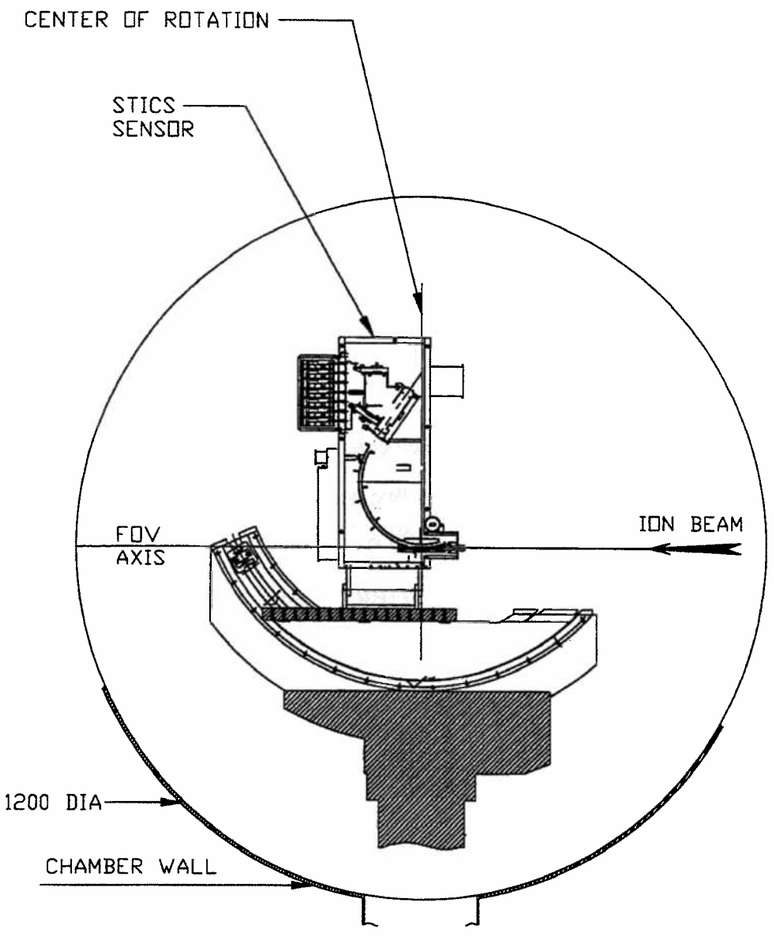

Figure A.1. A cross-sectional view of the STICS sensor inside the vacuum chamber at the Bern accelerator facility.

At the University of Maryland, calibrations were done using energy and time pulsers (see section A.3) to obtain the energy - channel conversions, the TOF - channel conversions, and the energy threshold values. Based on pulser calibrations done at University of Maryland in 1993, the threshold levels 7 and 8 ranged from 30.5 - 34.2 keV. At Bern the threshold levels were set to 8, 7, 7 for SSD1, 2, 3, respectively, for their values to be similar.

A.2 Calibration Results

A.2.1 Rate Linearity Tests

To ensure that the STICS microchannel plates were not being saturated during calibration, rate linearity tests were first done to determine the point where the rates are no longer proportional to the incident flux. Figure 3.2 shows a plot of the Front SEDA Rate 3&4 (FSR34) and Basic Rate 2 (BR2) against the incident parallel beam helium flux with energy 49.35 keV. BR2 begins to saturate for an incident flux of ~3 x 10^5 counts sec^{-1} cm^{-2}, whereas FSR34 starts to saturate at ~7 x 10^5 counts sec^{-1} cm^{-2}.

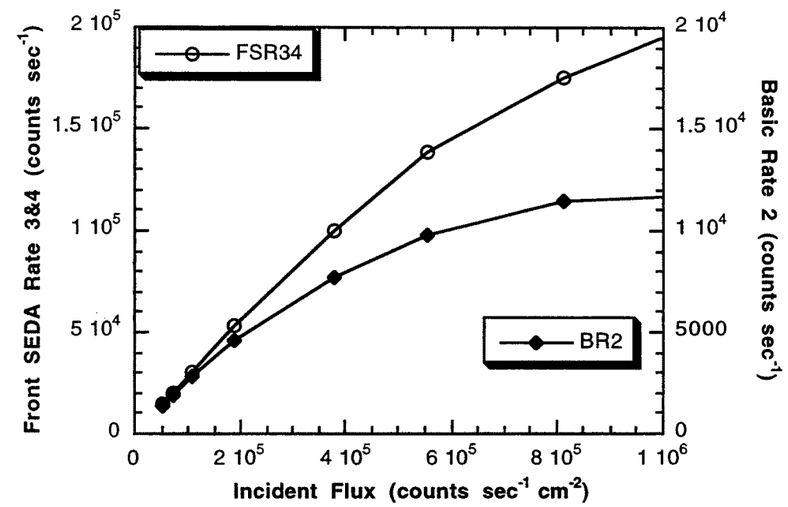

Figure A.2. Rate linearity test using He^+ at 49.35 keV for telescope 2.

BR2 becomes non-linear before FSR34 because the DPU needs extra classifying time for the Science Rates (see section 3.2.1). Fortunately, the saturation values are much higher than any value encountered in flight thus far. Therefore, the Electronic Deadtime effect will not be considered.

A.2.2 Angular Response

From the data taken at Bern, the instrument's angular responses both in the azimuthal (ß) and polar (α) directions of the entrance aperture were determined. With the deflection voltage and α angle fixed, ß scans were done at different energies (Figure A.3). These scans show that the peak E/Q value changes with ß. The envelope profile of DCR against ß for the combination of several energies, shown in Figure A.3, was fitted to a Gaussian, and the FWHM (Δß) was used as the effective azimuthal opening of the aperture.

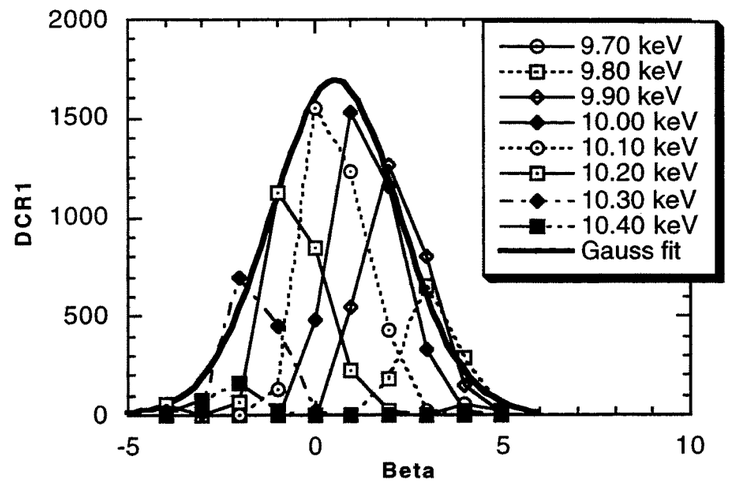

Figure A.3. Beta scans done at energies 9.70-10.40 keV using H^+ at Bern with alpha = 46 deg for DVS 04. The envelope profile is fitted to a Gaussian.

These scans were done with various ions at different deflection voltage steps. Figure A.4 shows a plot of $\Delta\beta$ at different polar directions, α, where $\alpha = 0$ is at the center of telescope 2. Note that between $\alpha = -20^\circ$ to $+20^\circ$, $\Delta\beta \approx 3^\circ$, but outside this range $\Delta\beta$ increases up to 6° on the sides. These outer values of $\Delta\beta$ are definitely incorrect since the maximum possible azimuthal acceptance angle of the physical opening is 4.8° (see section 2.3.2).

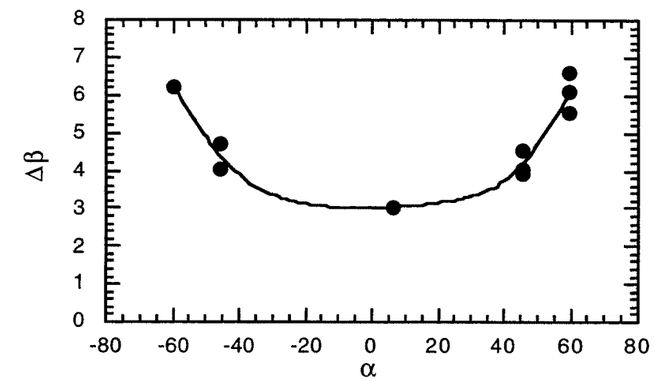

Figure A.4. The change in the azimuthal acceptance angle, $\Delta\beta$, is shown along the polar direction (α) of the entrance aperture using different ions (dots). The line is simply a smoothed curve through the data points. The outer values beyond $\alpha = \pm 20^\circ$ are not correct as explained in the below.

After discussing the matter with one of the engineers who built the sensor, Bob Cates, he came up with the following explanation. At Bern, the sensor is initially set up so that the ion beam enters the center of the opening (α=0, $\beta = 0$), Figure A.1. To change the relative incident angle of the beam, the sensor is rotated in the α and β directions, then minor adjustments are required in the vertical direction to ensure proper alignment. However, during the entire calibration at Bern, the vertical component was never changed due to a limitation in the program for automating the angle scans. This resulting effect is more pronounced at the higher values of α leading to the larger values of $\Delta\beta$, which Cates has verified from geometric calculations. The value of $\Delta\beta$ should be the same for all telescopes. Using the value for the center telescope, we get

$$\Delta ß_1 = \Delta ß_2 = \Delta ß_3 = 3.0 \pm 0.2^\circ \qquad (A.1)$$

For the polar direction, the first α scan was done at ß=0° and DVS 19 for beam energies of 55.35, 55.45, 55.55, and 55.65 keV using He^{+1}. However, this scan only covered the middle telescope as the α angle was changed from -28° to +28° in increments of 2° (Figure A.5). A slit was placed in front of the instrument to simulate a narrow beam. The boundaries of the middle telescope are clearly indicated by the profile going to zero at ±26°. The sharp decreases occuring at -12°, 0° and 14° are due to the blockages mentioned in section 2.3.2.

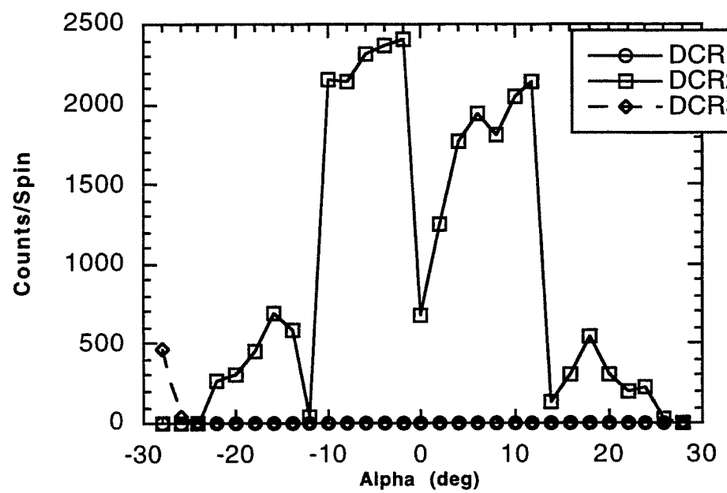

Figure A.5. Alpha scan using He^+ at 55.35 keV with ß=0.

The other α scans were done at ß=0°, 0.5° and 1°, and DVS 4 with a beam of H^+ ions, whose energy was "wobbled" between 9.4 and 10.7 keV at 28 Hz. These scans covered all three telescopes (Figure A.6). The FWHM (Δα) of DCR against alpha was

determined for each telescope at each beta. The sharp decreases within telescopes are not as

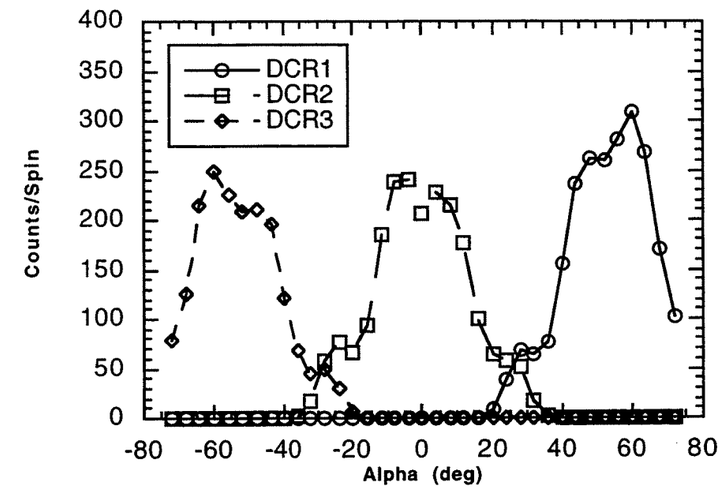

Figure A.6. Alpha scan using H^+ with energy wobbled between 9.4-10.7 keV at ß=0.

distinct here probably because α was incremented by 4° and the peak E/Q may have occurred just at the edge of a blockage. The approximate value of Δα for each telescope is as follows:

$$\Delta\alpha_1 = 31 \pm 1^\circ$$
$$\Delta\alpha_2 = 32 \pm 1^\circ \qquad (A.2)$$
$$\Delta\alpha_3 = 30 \pm 1^\circ$$

Therefore, the effective solid angle, $\Delta\Omega$, subtended by each telescope is

$$\Delta\Omega_1 = 0.028 \pm 0.002 \text{ sr}$$
$$\Delta\Omega_2 = 0.029 \pm 0.002 \text{ sr} \qquad \text{(A.3)}$$
$$\Delta\Omega_3 = 0.027 \pm 0.002 \text{ sr}$$

A.2.3 Energy Passband $\Delta E/Q$

The E/Q scans were used to obtain the energy passband for each voltage step. A plot of DCR against E/Q was first fitted to a Gaussian distribution (Figure A.7). The full width at half maximum (FWHM) was then taken to be $\Delta E/Q$. Table A.2 shows a list of the FWHM divided by the mean E/Q value from the fit for each voltage step that was calibrated. The values are all between 1-2% of the mean, except for voltage step 0 which is about 6%. The E/Q profile for this step produces a double peak which may be due to the beam at Goddard. Because the beam energies at Bern were more precisely known, only the Bern data for ß=1.0° (unshaded data in Table A.2) were used in determining the energy passband,

$$\Delta E/Q = (0.019 \pm 0.001)E/Q \qquad \text{(A.4)}$$

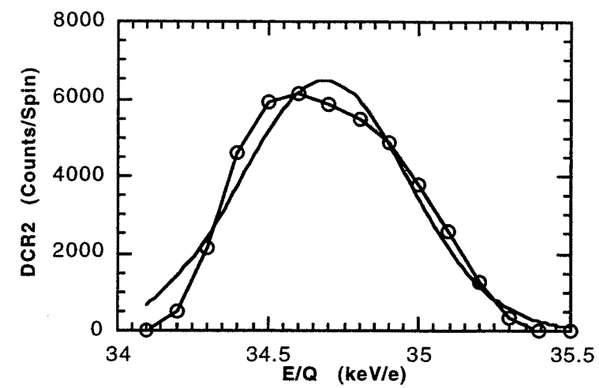

Figure A.7. E/Q scan of deflection voltage step (DVS) 15 using O^+ with alpha =6.4°, ß=1.0° for telescope 2 at Bern.

Table A.1. E/Q resolution [FWHM/(Mean E/Q)] for all calibrated ions. Only the unshaded data (rows 0 - 14) were used to determine the E/Q resolution.

	Telescope	Ion	Mass	DVS	Mean E/Q	FWHM	FWHM/(Mean E/Q)	Accelerator
0	1	H+	1	17	44.23	0.79415	0.018	Bem
1	3	H+	1	4	9.94	0.18553	0.019	Bem
2	2	H+	1	18	48.81	0.81809	0.017	Bem
3	2	H+	1	13	27.50	0.46795	0.017	Bem
4	2	Ne+	20	2	7.89	0.14952	0.019	Bem
5	2	Ne+	20	14	30.88	0.57739	0.019	Bem
6	2	Ne+	20	4	9.87	0.18868	0.019	Bem
7	2	Ne+	20	10	19.55	0.37737	0.019	Bem
8	3	Ne+	20	4	9.96	0.20498	0.021	Bem
9	1	O+	16	8	15.81	0.32855	0.021	Bem
10	3	O+	16	8	15.69	0.31334	0.020	Bem
11	2	O+	16	17	43.67	0.82359	0.019	Bem
12	2	O+	16	12	24.58	0.47235	0.019	Bem
13	2	O+	16	8	15.57	0.30054	0.019	Bem
14	2	O+	16	15	34.69	0.65225	0.019	Bem
15	1	He+	4	18	50.04	0.78546	0.016	Bem
16	3	He+	4	18	49.68	0.74834	0.015	Bem
17	2	Ne+	20	2	7.98	0.11379	0.014	Bem
18	2	He+	4	18	49.47	0.59118	0.012	Bem
19	2	He+	4	19	55.47	0.68777	0.012	Bem
20	2	He+	4	19	55.49	0.69700	0.013	Bem
21	2	H+	1	0	6.27	0.39985	0.064	Small
22	2	H+	1	4	9.89	0.34576	0.035	Small
23	2	H+	1	9	17.53	0.38584	0.022	Small
24	2	H+	1	12	24.69	0.39455	0.016	Small
25	2	H+	1	13	27.69	0.43514	0.016	Small
26	2	H+	1	14	31.07	0.46056	0.015	Small
27	2	H+	1	15	34.83	0.43956	0.013	Small
28	2	H+	1	16	39.14	0.56597	0.014	Small
29	2	H+	1	18	49.28	0.60109	0.012	Small
30	2	H+	1	20	61.98	0.76011	0.012	Small
31	2	H+	1	23	87.58	1.01384	0.012	Small
32	2	H+	1	24	98.35	1.06737	0.011	Small
33	2	H+	1	25	110.35	1.19670	0.011	Small
34	2	H+	1	20	59.98	1.39858	0.023	big
35	2	H+	1	24	96.74	1.02399	0.011	big
36	2	H+	1	26	122.32	2.26532	0.019	big
37	2	H+	1	27	136.83	2.04440	0.015	big
38	2	H+	1	28	153.45	2.26676	0.015	big
39	2	H+	1	29	172.72	2.63318	0.015	big
40	2	H+	1	30	193.85	2.09030	0.011	big
41	2	H+	1	31	217.98	2.81279	0.013	big

A.2.4 Start and Stop TOF Effieciencies

Figures A.8 - A.15 shows the TOF efficiency curves for the Start Efficiency (η_1) and Stop Efficiencies (η_2) plotted against energy-per-nucleon (in units of keV/amu) for telescope 2. The data from all three accelerators were plotted on the same graph and the best smooth curve was drawn by hand through the data points (see Tables A.2 - A.7 for values). The data points lie within the smoothed curves to an accuracy of 10% for the Start Efficiency and 20% for the Stop Efficiency for all ions. In most cases the smoothing was not difficult. However, looking at the hydrogen and nitrogen curves, the problem in using different accelerators is apparent. The data from the big accelerator for DCR/FSR and TCR/FSR do not follow the data from the other two accelerators for hydrogen and nitrogen. But the DCR/RSR data matchup fairly well for all three accelerators. The beam may not have been entering at the best angle so as to give these reduced ratios.

The elements carbon, nitrogen, oxygen, and neon all seem to have the same efficiencies to within experimental errors. The same set of smooth curves is used for carbon, nitrogen, oxygen, and neon. The data for argon and krypton only covered a small energy-per-nucleon range; however the smoothed curves extend far below and above the data. The smoothed curves for argon were drawn using the data points along with the smoothed neon curves and using the assumptions that the argon should be displaced above the oxygen curve and that the curves should not cross.

Figure A.16 shows the smoothed curves for hydrogen, helium, carbon, nitrogen, oxygen, neon, argon, and krypton for the three different efficiencies. The curves for other elements can be obtained by interpolating linearly between these curves.

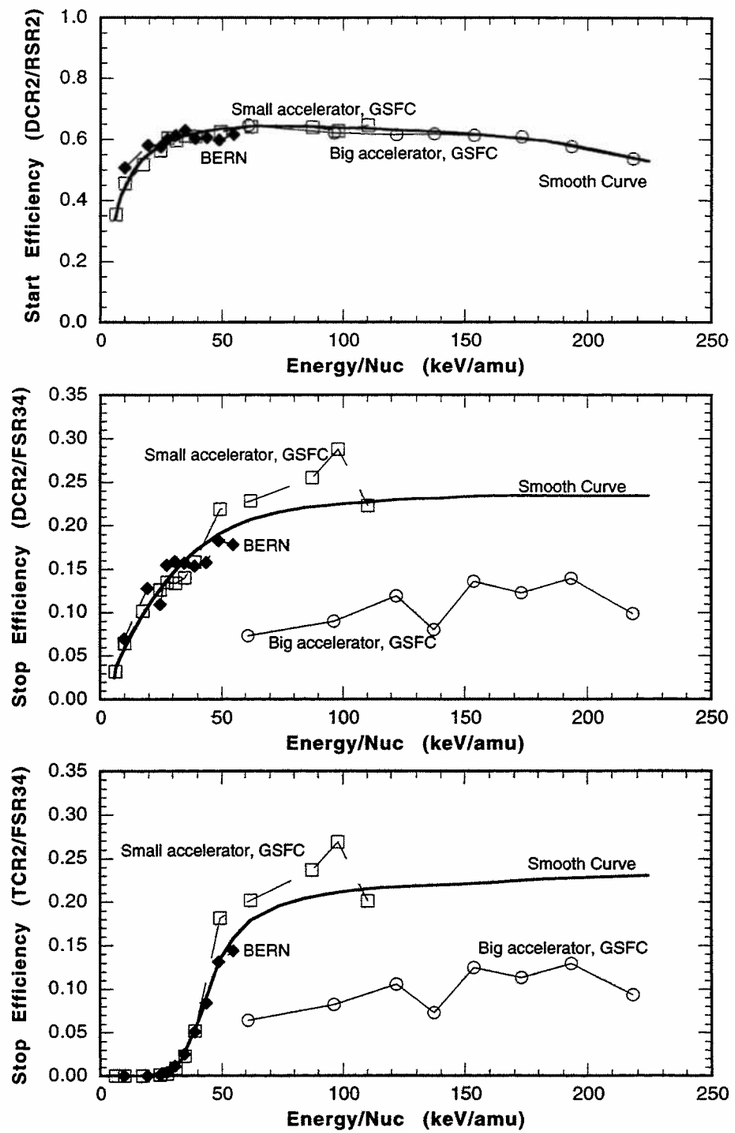

Figure A.8. Hydrogen TOF telescope efficiencies.

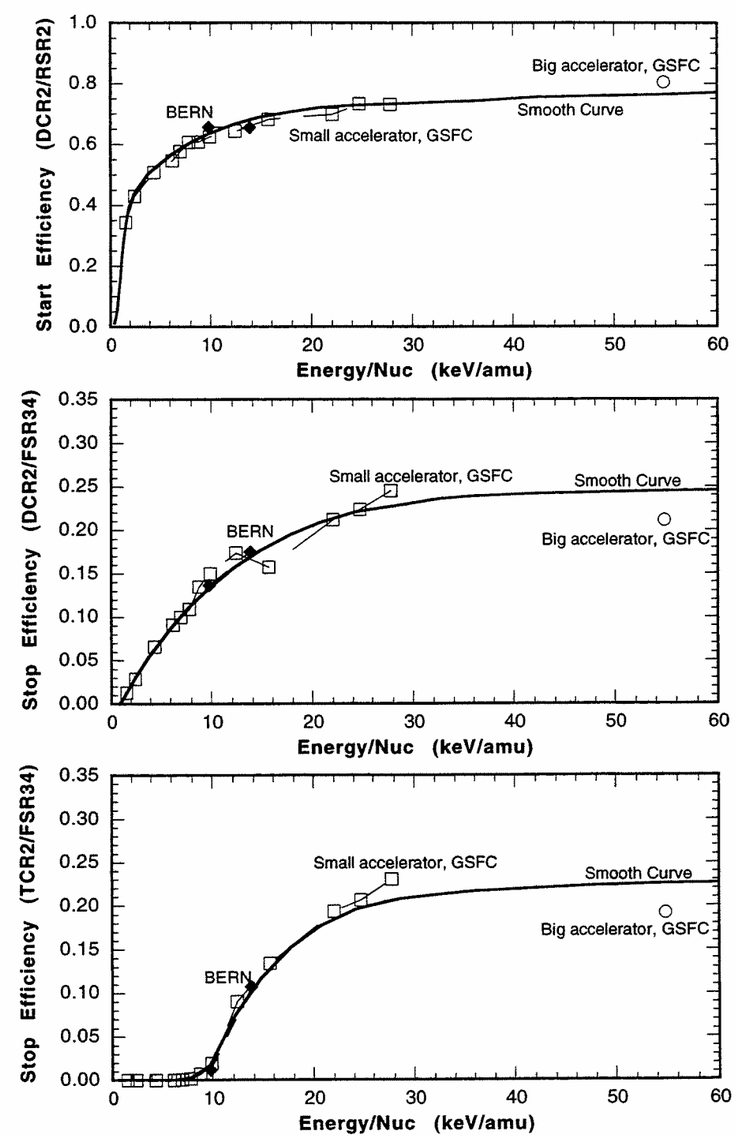

Figure A.9. Helium TOF telescope efficiencies.

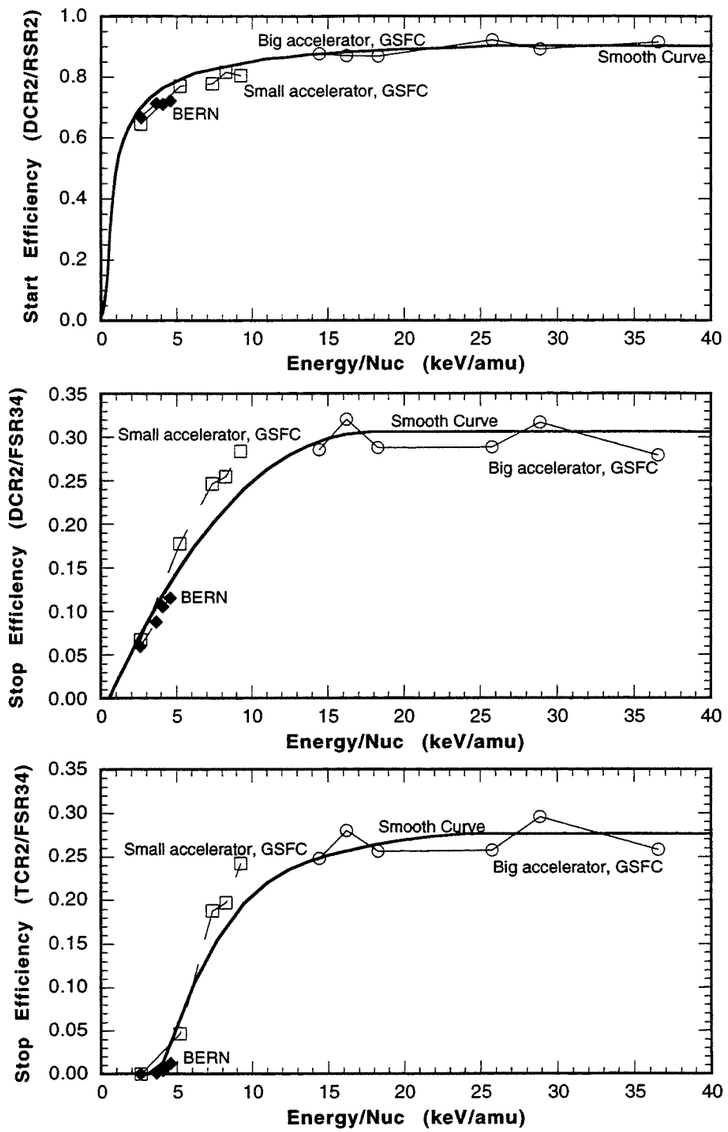

Figure A.10. Carbon TOF telescope efficiencies.

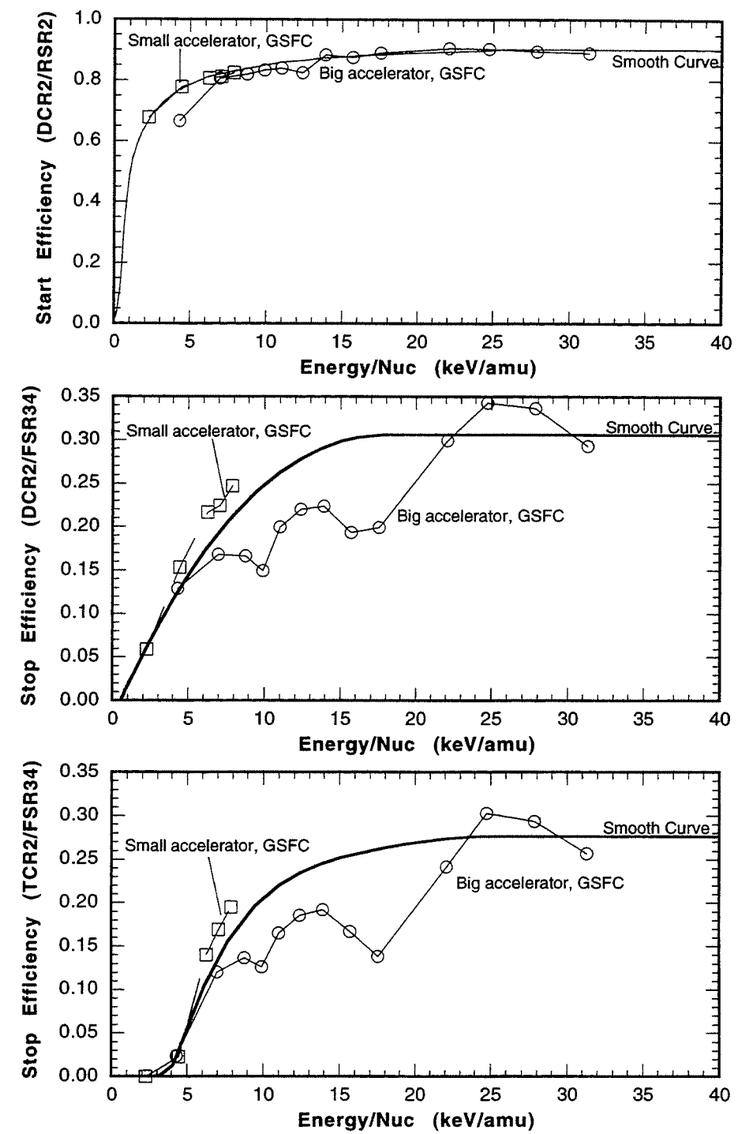

Figure A.11. Nitrogen TOF telescope efficiencies.

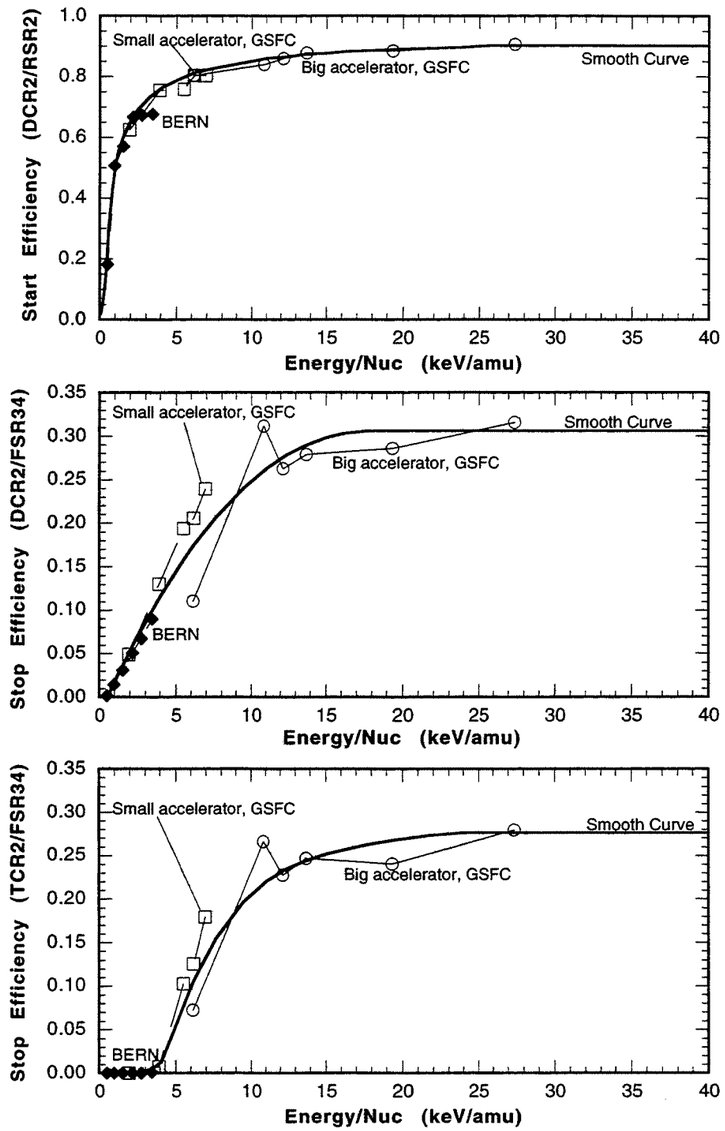

Figure A.12. Oxygen TOF telescope efficiencies.

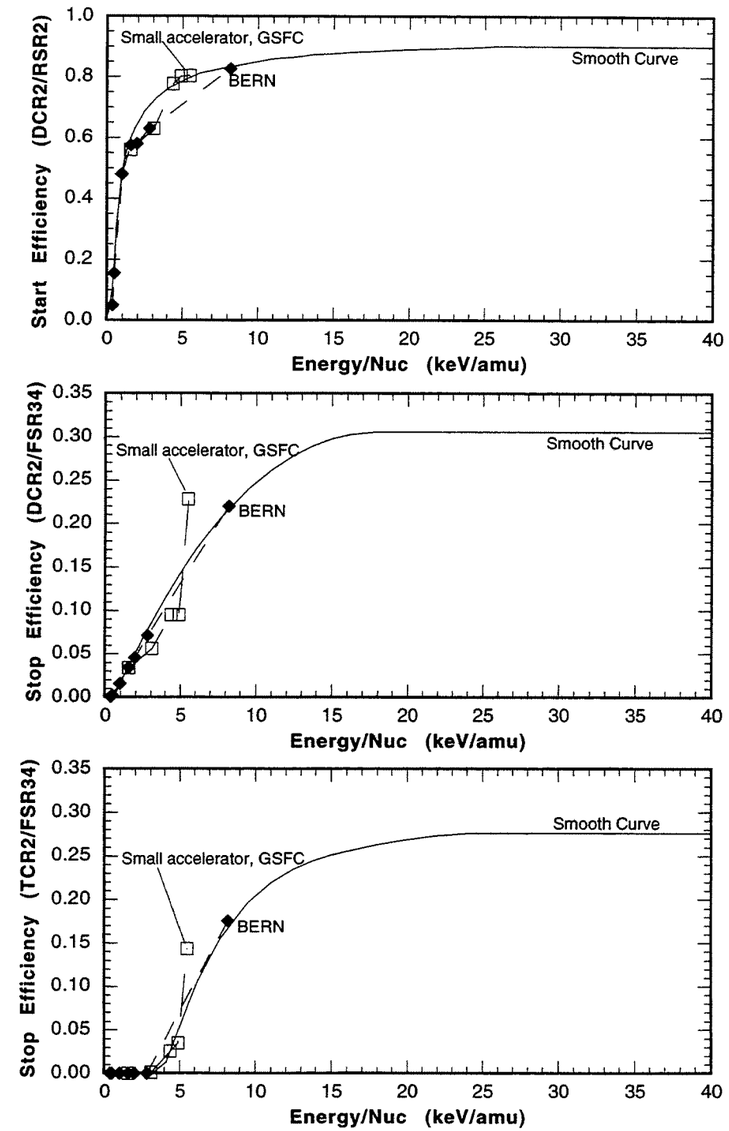

Figure A.13. Neon TOF telescope efficiencies.

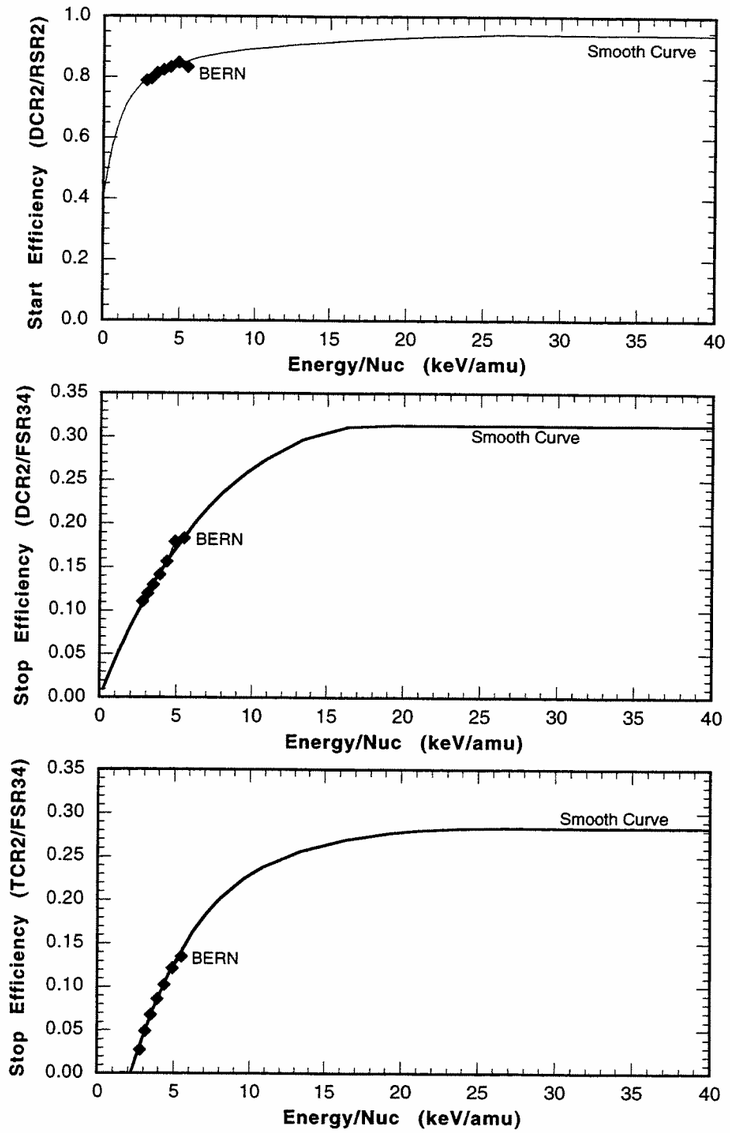

Figure A.14. Argon TOF telescope efficiencies.

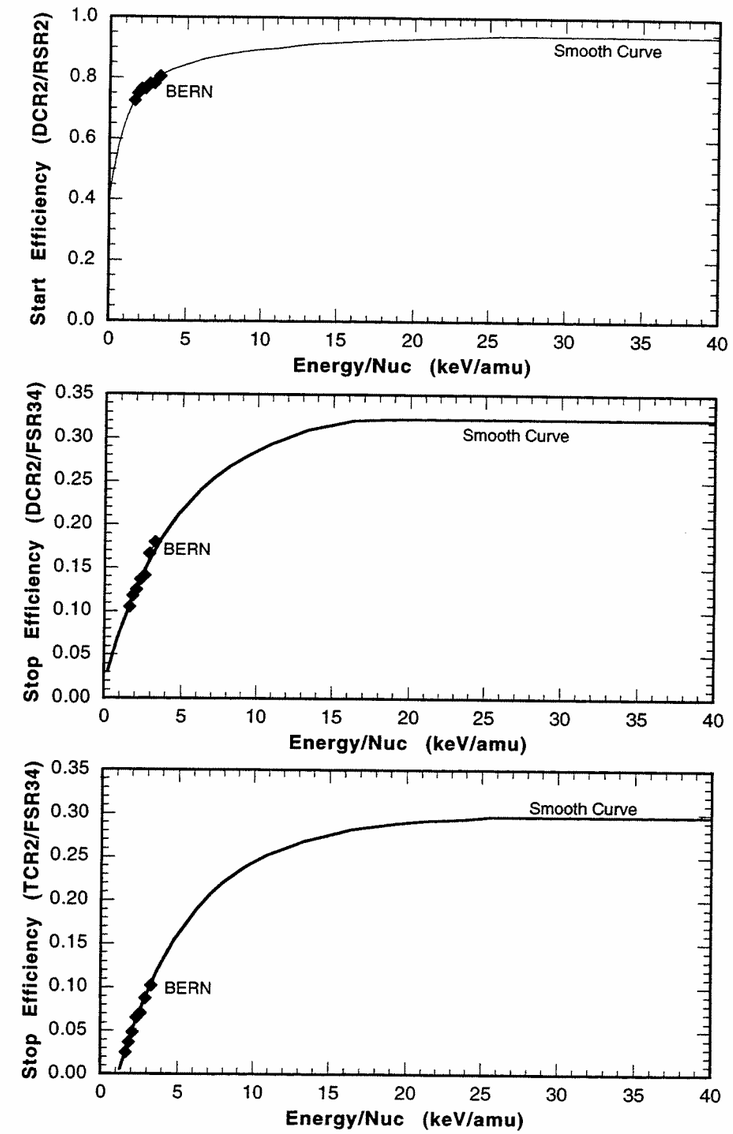

Figure A.15. Krypton TOF telescope efficiencies.

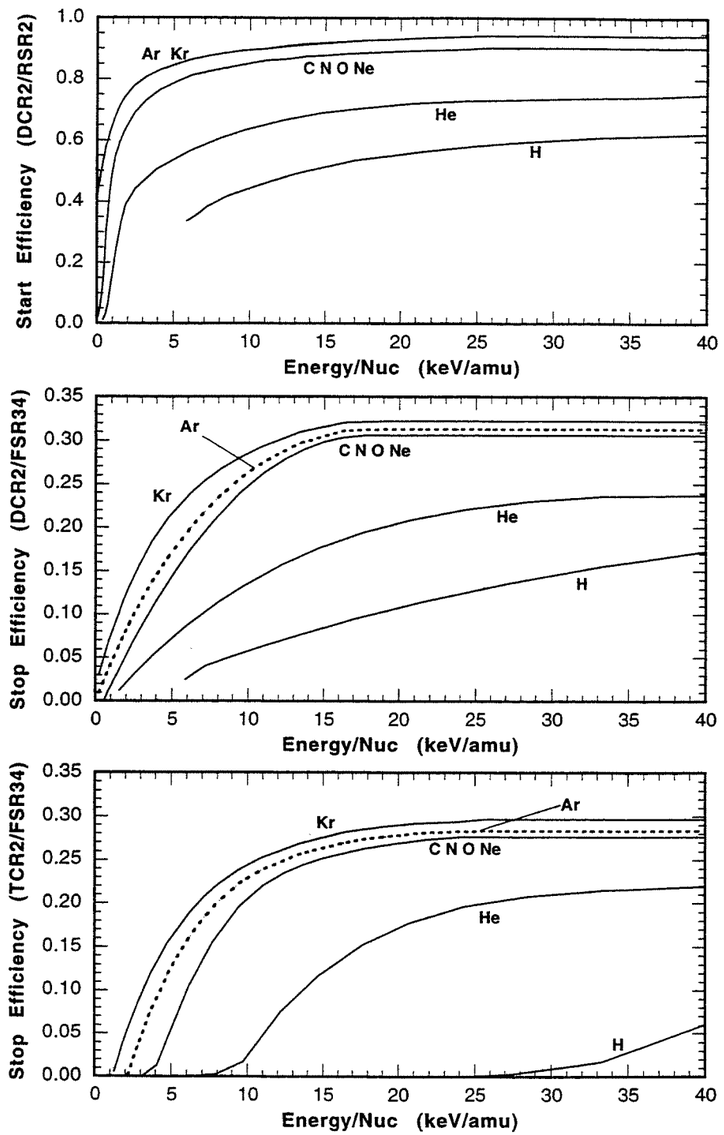

Figure A.16. Smoothed TOF telescope efficiency curves for H, He, C, N, O, Ne, Ar, and Kr. Same curves used for C, N, O, and Ne.

Table A.2. Hydrogen TOF telescope smoothed efficiency values.

	Prob 2	Prob 3	Prob 1
	Hydrogen		
E/Nuc(keV/amu)	DCR/FSR (stop)	TCR/FSR (triple)	DCR/RSR (start)
224.543106	0.233878	0.230433	0.528571
203.655396	0.233878	0.228942	0.566122
191.906006	0.233878	0.227583	0.584082
182.767593	0.233878	0.226308	0.595510
175.587494	0.233878	0.225150	0.600408
161.060104	0.233878	0.222668	0.611837
148.825104	0.232653	0.220856	0.620000
139.033905	0.231429	0.219693	0.624898
129.242798	0.230612	0.218588	0.628163
121.409897	0.229411	0.217496	0.631429
116.188004	0.228220	0.216545	0.633061
109.007797	0.226634	0.214824	0.636327
101.827698	0.225051	0.212526	0.637959
93.689301	0.223093	0.209132	0.641224
84.856400	0.220428	0.204340	0.642857
73.759789	0.215455	0.195714	0.644490
62.010441	0.206702	0.178872	0.642857
54.830292	0.198571	0.158163	0.637143
48.955608	0.190120	0.133080	0.634694
39.817230	0.172303	0.059007	0.621633
33.289822	0.155498	0.017209	0.610204
27.415140	0.136898	0.002862	0.592245
24.799999	0.126932	0.001029	0.580816
21.540470	0.114511	0.000000	0.564490
16.971279	0.094156	0.000000	0.533469
13.054830	0.074449	0.000000	0.491020
11.096610	0.063758	0.000000	0.460000
8.485640	0.048587	0.000000	0.417551
7.180157	0.040594	0.000000	0.383274
6.527415	0.032857	0.000000	0.357143
5.874674	0.024490	0.000000	0.337551

Table A.3. Helium TOF telescope smoothed efficiency values.

Helium			
E/Nuc(keV/amu)	DCR/FSR	TCR/FSR	DCR/RSR
150.000000	0.250000	0.230204	0.775510
80.000000	0.250000	0.230204	0.775510
75.000000	0.248571	0.228980	0.775510
66.422981	0.247143	0.227755	0.771429
60.469971	0.245714	0.226531	0.771429
54.516972	0.244286	0.225306	0.763265
47.937340	0.242857	0.222857	0.759184
42.297649	0.241429	0.220408	0.755102
36.031330	0.238571	0.216735	0.742856
32.584862	0.235714	0.213061	0.738776
28.511749	0.228571	0.208104	0.734286
24.281981	0.220928	0.196104	0.728571
20.678850	0.208635	0.177230	0.720000
17.702351	0.194634	0.152558	0.705714
14.725850	0.176314	0.116710	0.688571
12.219320	0.156813	0.075522	0.665714
9.712794	0.132823	0.017300	0.634286
7.989556	0.113283	0.002792	0.605714
6.220100	0.090004	0.000100	0.568479
5.953003	0.086490	0.000000	0.562857
3.916449	0.055119	0.000000	0.505714
2.506527	0.030367	0.000000	0.442857
1.879896	0.018495	0.000000	0.391429
1.566580	0.012347	0.000000	0.334286
1.344648	0.007543	0.000000	0.270173
1.174935	0.004715	0.000000	0.221783
1.044386	0.002683	0.000000	0.176998
0.861619	0.001048	0.000000	0.106552
0.704961	0.000339	0.000000	0.060627
0.574413	0.000087	0.000000	0.032604
0.483029	0.000034	0.000000	0.019082
0.404700	0.000014	0.000000	0.011816

Table A.4. TOF telescope smoothed efficiency values for Carbon, Nitrogen, Oxygen, and Neon.

Carbon, Nitrogen, Oxygen, Neon			
E/Nuc(keV/amu)	DCR/FSR	TCR/FSR	DCR/RSR
150.000000	0.305510	0.276005	0.902040
40.000000	0.305510	0.276005	0.902040
25.691910	0.305510	0.276005	0.902040
24.047001	0.305510	0.276005	0.897959
21.853790	0.305510	0.273061	0.893878
19.582251	0.305510	0.267947	0.889796
17.859011	0.305510	0.262447	0.885714
16.214100	0.302895	0.256482	0.881633
15.039160	0.298140	0.251399	0.877551
13.707570	0.289692	0.244102	0.873469
12.454310	0.278642	0.234841	0.865306
11.044390	0.262457	0.220206	0.861224
9.477807	0.239599	0.196350	0.844898
7.672400	0.206581	0.154709	0.828571
6.187990	0.173823	0.105044	0.812245
5.248042	0.150359	0.064501	0.791837
4.073107	0.117964	0.013165	0.763265
3.211488	0.091988	0.001459	0.730612
2.558747	0.070918	0.000107	0.693200
2.428198	0.066704	0.000000	0.685714
1.801567	0.045311	0.000000	0.632653
1.472585	0.033658	0.000000	0.591429
1.190601	0.023438	0.000000	0.544082
0.992167	0.016116	0.000000	0.485714
0.861619	0.010985	0.000000	0.428571
0.704961	0.004988	0.000000	0.359184
0.626632	0.003060	0.000000	0.306122
0.469974	0.001338	0.000000	0.183673
0.417755	0.000829	0.000000	0.141257
0.339426	0.000467	0.000000	0.103589
0.287206	0.000266	0.000000	0.078139
0.208877	0.000133	0.000000	0.052655
0.104439	0.000052	0.000000	0.026021
0.052219	0.000031	0.000000	0.019088

Table A.5. Argon TOF telescope smoothed efficiency values.

Argon			
E/Nuc(keV/amu)	DCR/FSR	TCR/FSR	DCR/RSR
150.000000	0.312873	0.283250	0.942858
40.000000	0.312873	0.283250	0.942858
25.691910	0.312873	0.283250	0.942858
24.047001	0.312873	0.282623	0.939308
21.853790	0.312873	0.280642	0.935684
19.582249	0.312873	0.277151	0.931398
17.859009	0.312177	0.272843	0.926756
16.214100	0.310607	0.268112	0.921890
15.039162	0.304666	0.262971	0.917700
13.707569	0.297933	0.257146	0.912954
12.454311	0.287745	0.248907	0.906632
11.044389	0.274838	0.238606	0.898828
9.477807	0.255882	0.221970	0.892246
7.672400	0.227705	0.193613	0.879258
6.187989	0.198972	0.160527	0.864446
5.248043	0.177023	0.132043	0.848980
4.073107	0.146746	0.090513	0.828182
3.211488	0.121459	0.053141	0.806978
2.558747	0.100355	0.020095	0.782822
2.428198	0.095922	0.012960	0.776870
1.801567	0.073678	0.000000	0.740818
1.472585	0.061169	0.000000	0.711764
1.190601	0.050041	0.000000	0.675918
0.992168	0.041986	0.000000	0.644898
0.861618	0.036640	0.000000	0.624150
0.704961	0.030002	0.000000	0.597620
0.626631	0.026683	0.000000	0.584354
0.469973	0.019868	0.000000	0.546624
0.417754	0.017566	0.000000	0.532182
0.339426	0.014113	0.000000	0.510518
0.287207	0.011812	0.000000	0.496074
0.208877	0.008302	0.000000	0.474122
0.104438	0.004759	0.000000	0.444082
0.052219	0.003523	0.000000	0.424190

Table A.6. Krypton TOF telescope smoothed efficiency values.

Krypton			
E/Nuc(keV/amu)	DCR/FSR	TCR/FSR	DCR/RSR
150.000000	0.322154	0.296428	0.942858
40.000000	0.322154	0.296428	0.942858
25.691910	0.322154	0.296428	0.942858
24.047001	0.322154	0.294251	0.939308
21.853788	0.322154	0.292191	0.935684
19.582249	0.322154	0.289191	0.931398
17.859009	0.321329	0.285055	0.926756
16.214100	0.319836	0.280400	0.922018
15.039162	0.315542	0.275279	0.918796
13.707568	0.310676	0.269475	0.915146
12.454310	0.303007	0.261883	0.908164
11.044388	0.293221	0.252544	0.898980
9.477807	0.280094	0.238415	0.892246
7.672400	0.260642	0.215282	0.879258
6.187989	0.239111	0.188593	0.864446
5.248044	0.220592	0.165530	0.848980
4.073106	0.192971	0.131354	0.828182
3.211488	0.167539	0.100189	0.806978
2.558747	0.144677	0.072417	0.782822
2.428199	0.139695	0.066390	0.776870
1.801567	0.113829	0.035228	0.740818
1.472584	0.098521	0.016892	0.711764
1.190601	0.084524	0.004399	0.675918
0.992168	0.074185	0.001517	0.644898
0.861618	0.067279	0.000000	0.624150
0.704961	0.058496	0.000000	0.597620
0.626631	0.054104	0.000000	0.584354
0.469973	0.044914	0.000000	0.546624
0.417754	0.041784	0.000000	0.532182
0.339426	0.037088	0.000000	0.510518
0.287208	0.033957	0.000000	0.496076
0.208877	0.029232	0.000000	0.474122
0.104439	0.022857	0.000000	0.444082
0.052219	0.019126	0.000000	0.424190

Table A.7. Iron TOF telescope smoothed efficiency values obtained from linear interpolation between Argon and Krypton efficiencies.

Iron (interpolated)			
E/Nuc(keV/amu)	DCR/FSR	TCR/FSR	DCR/RSR
150.000000	0.316238	0.288028	0.942858
40.000000	0.316238	0.288028	0.942858
25.691910	0.316238	0.288028	0.942858
24.047001	0.316238	0.286839	0.939308
21.853790	0.316238	0.284829	0.935684
19.582249	0.316238	0.281516	0.931398
17.859009	0.315495	0.277271	0.926756
16.214100	0.313953	0.272567	0.921936
15.039161	0.308609	0.267433	0.918098
13.707570	0.302553	0.261616	0.913748
12.454311	0.293278	0.253612	0.907188
11.044389	0.281503	0.243659	0.898884
9.477807	0.264660	0.227932	0.892246
7.672399	0.239647	0.201469	0.879258
6.187990	0.213525	0.170703	0.864446
5.248044	0.192820	0.144184	0.848980
4.073107	0.163506	0.105320	0.828182
3.211488	0.138166	0.070199	0.806978
2.558747	0.116425	0.039065	0.782822
2.428199	0.111793	0.032332	0.776870
1.801567	0.088235	0.012772	0.740818
1.472585	0.074712	0.006124	0.711764
1.190602	0.062543	0.001595	0.675918
0.992168	0.053660	0.000550	0.644898
0.861618	0.047749	0.000000	0.624150
0.704962	0.040333	0.000000	0.597620
0.626632	0.036625	0.000000	0.584354
0.469973	0.028949	0.000000	0.546624
0.417753	0.026347	0.000000	0.532182
0.339427	0.022443	0.000000	0.510518
0.287207	0.019841	0.000000	0.496074
0.208877	0.015890	0.000000	0.474122
0.104438	0.010498	0.000000	0.444082
0.052219	0.008637	0.000000	0.424190

A.2.5 Geometric Factor

At Bern the beam's incident flux, I_O (before entering the instrument), was calculated from the current measured by the Faraday Cup using the following equation:

$$I_O = \frac{\text{current}}{Q \bullet e \bullet A_{FC}} \quad \text{[units of counts sec}^{-1}\text{ cm}^{-2}\text{]} \qquad (A.5)$$

where Q is the charge state of the particles, e is the elecronic charge 1.6×10^{-19} C, and A_{FC} is the effective area of the of the Faraday Cup (5 cm^2). Assuming that the beam's flux does not change while passing through the deflection system, the rate at which the particles pass through the carbon foil, CFR, is given by

$$CFR = I_O A_C \qquad (A.6)$$

where A_C is the effective area of the carbon foil that the particles pass through. From equation (3.13)

$$CFR = FSR*RSR/DCR \qquad (A.7)$$

If we plot CFR/Io against energy-per-nucleon for all the elements measured at Bern for telescope 2 (Figure A.17), we can see that the ratio is fairly constant, as expected. The Kr values are substantially above the average line because the Faraday Cup readings for Kr were so low that the digitization error was significant. Excluding the Kr data, we get

$$A_C = CFR/I_O = 0.49 \pm 0.03 \quad cm^2 \qquad (A.8)$$

Since the beams used in the calibration were parallel, the Parallel Beam Geometric Factor, G, is equal to A_C (equation 3.12). The Parallel Beam Geometric Factors for the other two telescopes were also determined using the same method. Therefore,

$$G_1 = 0.52 \pm 0.03 \text{ cm}^2$$
$$G_2 = 0.49 \pm 0.03 \text{ cm}^2 \qquad (A.9)$$
$$G_3 = 0.53 \pm 0.03 \text{ cm}^2$$

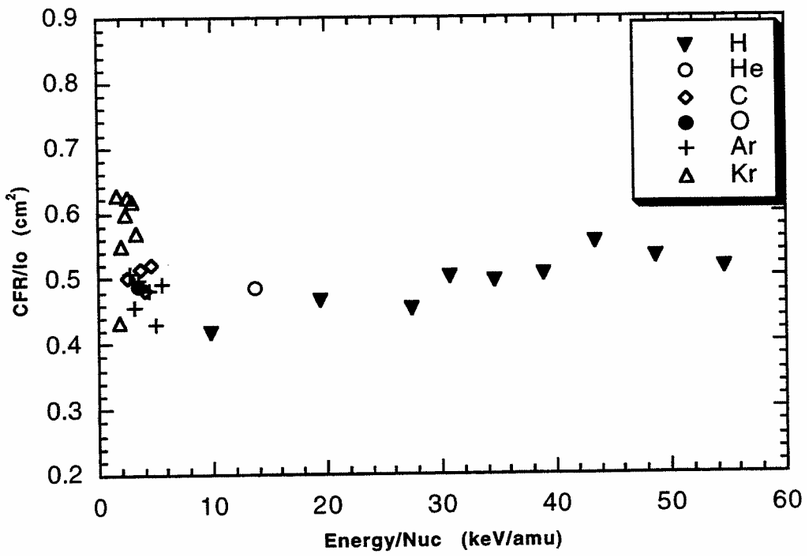

Figure A.17. Parallel Beam Geometric Factor for telescope 2 using Bern pre-flight calibration data. Kr values are artificially high due to low Faraday Cup current readings.

From the effective solid angles given in equation (A.3) and using equation (3.11), the Isotropic Geometric Factor, g, for each telescope is as follows:

$$g_1 = 0.015 \pm 0.001 \text{ cm}^2 \text{ sr}$$
$$g_2 = 0.014 \pm 0.001 \text{ cm}^2 \text{ sr} \qquad \text{(A.10)}$$
$$g_3 = 0.014 \pm 0.001 \text{ cm}^2 \text{ sr}$$

The total Isotropic Geometric Factor for the sensor is simply the sum of the individual ones, i.e., $g = 0.043 \pm 0.005$ cm^2 sr.

A.2.6 Sphere Efficiency

Even though a particle may have the correct E/Q, it is not guaranteed to make it all the way through the deflection system because the deflection system is not 100% efficient. The efficiency, η_D, of the spherical deflection system is defined as the ratio of the number of particles exiting the system to the number of particles entering the system, i.e.,

$$\eta_D = \frac{CFR}{I_o A_e} \qquad \text{(A.11)}$$

where I_o is the flux of the beam outside the instrument, and A_e is the area of the entrance aperture, which is equal to 0.84 cm^2 for each telescope (see section 2.3.2). From equations (A.8) and (A.9), we get

$$\eta_{D1} = 0.62 \pm 0.04$$
$$\eta_{D2} = 0.58 \pm 0.04 \qquad \text{(A.12)}$$
$$\eta_{D3} = 0.63 \pm 0.04$$

These values compare reasonably well to the analysis done by Paolini and Theodoridis (1967) on the transmission of charged particles through spherical electrostatic analyzers.

A.3 Pulser Calibrations

A.3.1 Energy Pulser Tests

The ion energy is measured by a solid-state detector (SSD) in the time-of-flight chamber (see Section 2.3.1). The SSD sends a charge pulse, which is proportional to the ion energy, to an amplifier. The amplifier magnifies the signal and sends it to the analog electronics, which converts the signal to an energy channel number, E_{ch}. The energy pulser tests were done to determine the relation between the incident energy, E, in units of keV (kiloelectronvolts) and the energy channel number, E_{ch}.

These energy pulser tests were done in November, 1993. To do this an EG&G Ortec Research Pulser, Model 448, was used to create a charge pulse of a known energy, E. The pulser changes the charge which corresponds to changing the energy. The pulser was connected directly to the SSD preamplifier, bypassing the SSD detector itself. The pulser was calibrated on 10/20/93. The Rise Time for each pulse was 20 ns and the Decay Time Constant, 50 μsec. The Relay was set to Internal Oscillation and the Pulse/Sec, to 100. The output was connected to the Charge Terminator, which is used to convert the voltage output pulse into a charge pulse. The Charge Terminator was then connected to the SSD preamplifier (Figure A.18). For the STICS housekeeping FIFO, LOGCAL and TGS were ON. The SSD biases were turned ON, and the thresholds were all set to Level 8. The Trigger mode was E+T, and all other settings were at the default.

For the first set of data the pulser was connected to the preamplifier of SSD1. The energy on the pulser was set to 40 keV, and data were collected for 1 minute. A histogram of Channel Number versus Counts was then plotted using a computer program, called Mariah, which also calculated the mode, mean (μ), standard deviation (σ) and full width at half maximum (FWHM) of the distribution. The program used the following equation to calculate σ:

$$\sigma = \sqrt{\frac{\sum_i \text{Counts}(i) * [i - \mu]^2}{\sum_i \text{Counts}(i)}} \qquad (A.13)$$

where i is the channel number and Counts(i) is the number of counts at a given channel number. The distribution was assumed to be Gaussian, so FWHM = 2.354σ.

Data were collected for different energy settings between 40 - 2600 keV. For each energy setting the mode, mean, σ and FWHM were recorded. The same was done for SSD2 and SSD3 (see Table A.8-A.10). A plot of energy versus mean channel number is shown in Figure A.19 for SSD2. If the SSD1 and SSD3 data were also plotted, they would fall directly on the SSD2 line shown in Figure A.19, as expected.

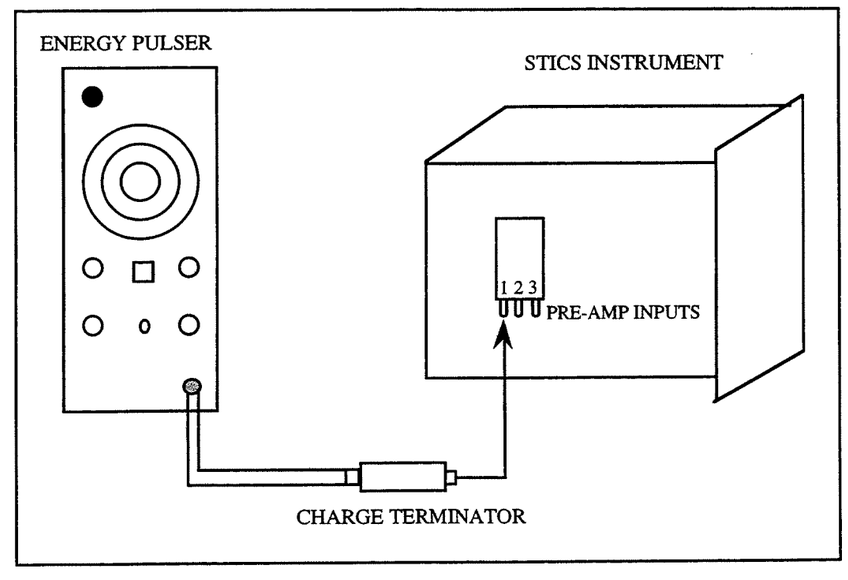

Figure A.18. Diagram of set-up for the energy pulser test.

In July 1992, energy pulser were also done (see Table A.11-A.13). These results were used to determine the following energy to channel number conversion currently being used by the DPU for all three solid state detectors:

$$E\,\{keV\} = (E_{chn} + 6)/0.37654587 \qquad (A.14)$$

After the 1992 data were taken, some resistors were re-trimmed and threshold values changed. Therefore, the November 1993 data may be used to generate new energy to channel algorithms.

So should it?

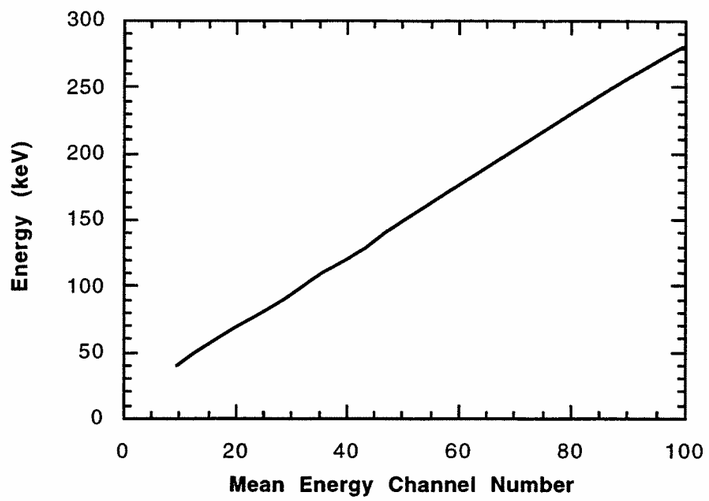

Figure A.19. The linear relation between the energy, E, and the mean energy channel number, E_{ch}, is shown in this plot for SSD2.

Table A.8. Energy pulser results for SSD1 done November 1993.

E(keV)	Mode1 Chn #	Mean1 Chn #	Sigma1	FWHM1
40	9	10.02	2.67	6.29
50	11	13.14	2.77	6.52
60	15	16.92	2.55	6.01
70	19	20.71	2.62	6.16
80	24	24.81	2.59	6.10
90	29	28.85	2.35	5.53
100	32	32.39	2.25	5.29
110	35	35.86	2.17	5.11
120	39	39.65	2.32	5.47
130	43	43.33	2.24	5.27
140	46	47.06	1.90	4.48
150	50	50.70	2.02	4.76
175	60	59.81	2.01	4.72
200	68	69.09	2.12	4.98
225	78	78.45	2.03	4.78
250	87	87.95	1.89	4.46
275	97	97.43	2.02	4.77
300	106	106.65	2.05	4.82
325	116	116.37	2.05	4.83
350	125	125.97	1.92	4.53
375	134	135.23	2.14	5.03
400	145	144.91	2.18	5.12
450	163	164.13	2.14	5.04
500	183	183.22	2.12	4.99
550	203	202.48	2.23	5.24
600	222	221.93	1.94	4.56
650	240	241.44	2.07	4.87
700	260	260.22	2.18	5.14
750	280	279.91	2.17	5.12
800	298	299.40	2.31	5.43
900	338	338.79	2.20	5.18
1000	380	379.53	2.37	5.59
1100	420	420.46	2.23	5.25
1200	462	461.60	2.43	5.72
1300	502	502.71	2.23	5.25
1400	544	542.59	2.06	4.85
1500	584	583.08	1.98	4.65
1600	624	624.65	2.59	6.09
1800	704	706.49	2.06	4.85
2000	788	787.84	2.53	5.95
2200	864	866.34	2.06	4.84
2400	940	942.50	2.06	4.85

Table A.9. Energy pulser results for SSD2 done November 1993.

E(keV)	Mode2 Chn #	Mean2 Chn #	Sigma2	FWHM2
40	8	9.38	2.47	5.81
50	11	12.56	2.56	6.02
60	15	16.64	2.71	6.38
70	21	20.48	2.76	6.50
80	24	24.48	2.43	5.73
90	29	28.21	2.26	5.31
100	31	32.01	2.23	5.24
110	35	35.65	2.39	5.63
120	39	39.48	2.15	5.05
130	43	43.25	2.17	5.11
140	46	46.85	2.19	5.16
150	50	50.33	2.18	5.12
175	59	59.49	2.03	4.78
200	68	68.72	2.07	4.88
225	78	78.24	2.29	5.40
250	87	87.55	2.06	4.86
275	97	97.04	2.18	5.14
300	106	106.57	2.05	4.82
325	115	116.03	2.16	5.08
350	125	125.50	2.06	4.85
375	134	134.97	2.20	5.19
400	144	144.48	2.08	4.90
450	163	163.58	2.08	4.89
500	183	182.93	1.95	4.59
550	202	202.06	2.24	5.28
600	220	221.38	2.11	4.97
750	278	279.33	1.98	4.67
900	338	338.41	2.21	5.20
1100	420	419.88	2.47	5.82
1400	540	542.18	2.04	4.80
1600	624	624.07	2.62	6.18
1800	704	706.04	2.01	4.73
2200	868	866.81	2.04	4.80

Table A.10. Energy pulser results for SSD3 done November 1993.

E(keV)	Mode3 Chn #	Mean3 Chn #	Sigma3	FWHM3
40	10	11.00	2.41	5.67
50	13	13.63	2.65	6.23
70	21	21.06	2.68	6.31
100	31	32.79	2.28	5.36
130	43	44.12	2.25	5.30
150	51	51.35	2.06	4.85
175	59	60.44	2.11	4.96
250	88	88.50	2.07	4.87
325	117	116.91	1.91	4.50
450	165	164.60	2.08	4.90
600	222	222.29	2.08	4.90
750	280	280.19	2.22	5.24
900	338	338.92	2.25	5.29
1100	420	420.75	2.25	5.28
1400	544	542.72	2.05	4.83
1600	624	625.00	2.71	6.38
1800	704	706.15	2.03	4.78
2000	784	785.25	2.54	5.97
2200	864	863.62	2.51	5.92
2400	940	940.40	2.52	5.92
2600	1004	1004.14	1.79	4.21

Table A.11. Energy pulser results for SSD1 done July 1992.

E(keV)	Mean1 Chn #	Sigma1
40	15.63	3.04
50	15.85	2.82
60	17.44	2.82
70	20.50	3.10
80	24.73	3.12
90	28.46	3.14
100	32.20	2.83
125	41.43	2.65
150	50.31	2.73
175	59.89	2.63
200	69.09	2.55
250	87.53	2.72
300	106.31	2.62
350	125.31	2.73
400	144.18	2.67
450	163.28	2.82
500	182.21	2.69
600	220.63	2.73
700	258.62	2.69
800	297.44	2.79
900	336.63	2.80
1000	376.90	2.86
1250	478.64	2.88
1500	579.41	3.01
1750	681.11	3.01
2000	782.54	3.23
2250	881.72	2.87
2400	938.41	2.94
2500	976.11	2.83

Table A.12. Energy pulser results for SSD2 done July 1992.

E(keV)	Mean2 Chn #	Sigma2
50	16.33	2.34
60	17.46	2.48
70	20.32	2.81
80	24.28	2.94
90	28.10	2.99
100	32.04	2.82
125	41.09	2.68
150	50.50	2.55
175	59.50	2.47
200	68.66	2.55
250	87.61	2.64
300	106.66	2.73
350	125.72	2.63
400	144.59	2.63
450	163.64	2.69
500	182.93	2.67
600	221.62	2.66
700	259.98	2.69
800	299.27	2.74
900	338.80	2.71
1000	379.39	2.82
1250	482.13	2.72
1500	583.88	3.13
1750	686.36	2.94
2000	788.59	2.99
2250	889.41	2.84
2400	947.58	2.89
2500	985.64	2.76

Table A.13. Energy pulser results for SSD3 done July 1992.

E(keV)	Mean3 Chn #	Sigma3
60	18.20	2.54
70	21.22	2.97
80	25.33	3.13
90	29.19	2.90
100	33.53	2.83
125	43.15	2.65
150	52.93	2.54
175	62.28	2.50
200	71.83	2.50
250	91.17	2.55
300	110.98	2.52
350	130.41	2.53
400	149.99	2.57
450	169.81	2.54
500	189.81	2.52
600	229.68	2.48
700	269.39	2.58
800	309.89	2.63
900	350.88	2.76
1000	393.14	2.77
1250	499.35	2.70
1500	604.27	3.05
1750	709.61	2.81
2000	813.03	2.75
2250	913.61	2.82
2400	972.88	2.64
2500	1010.72	2.49

A.3.2 Threshold Tests

Using the same set-up as described in Section A.3.1, data were acquired to determine the energy of Threshold Levels 7 and 8. The pulser setting was adjusted such that it emitted 100 pulses per second at any given energy. The pulser energy was varied and the corresponding SSD rate was averaged over 20 spins using the computer program Mariah. For each SSD at a given threshold level, data were collected for pulser energy versus SSD rate, which is summed over 2.72 seconds.

The noise counts were determined when the pulser was switched off. Then these counts were subtracted from the SSD rates, and the rates were then normalized to the largest value. Plots of the normalized rate versus energy were then made (see Figure A.19). The threshold energy was then found by determining the energy when the rate is 50%:

Table A.14. Energy thresholds for the different solid state detectors.

	Threshold level 7 (keV)	Threshold level 8 (keV)
SSD1	---	30.5
SSD2	32.4	34.2
SSD3	31.3	32.5

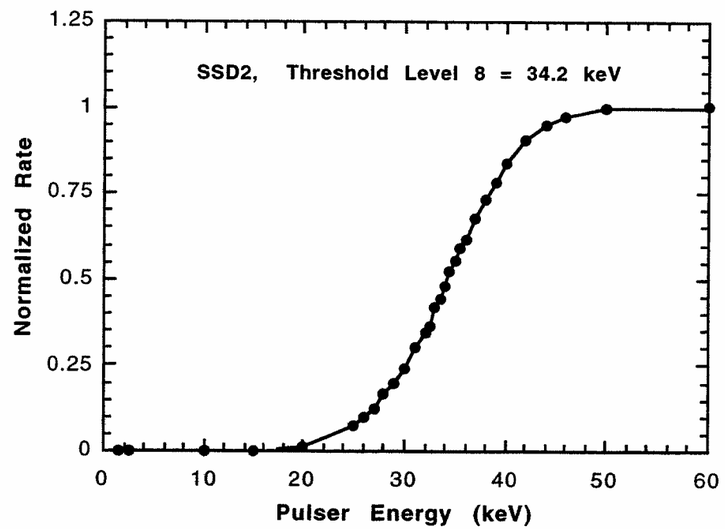

Figure A.20. Normalized SSD2 rate plotted against pulser energy. The threshold level is obtained by finding the energy at the 50% SSD value.

A.3.3 Time Pulser Tests

A diagram of the apparatus is shown in Figure A.20. An EG&G Ortec Delay Generator, Model 9650, was connected to a Tektronix Time Pulse Generator, Model PG502. The pulser was then connected to an Oscilloscope which was triggered by the Delay Generator. The Oscilloscope was then connected to a Voltage Attenuator which was in turn connected to the START and STOP of the STICS time-of-flight telescope. The time on the Delay Generator was varied between 10 - 400 nanoseconds and the corresponding mean channel number was obtained from the histogram plotted using Mariah (Table A.15 - A.17).

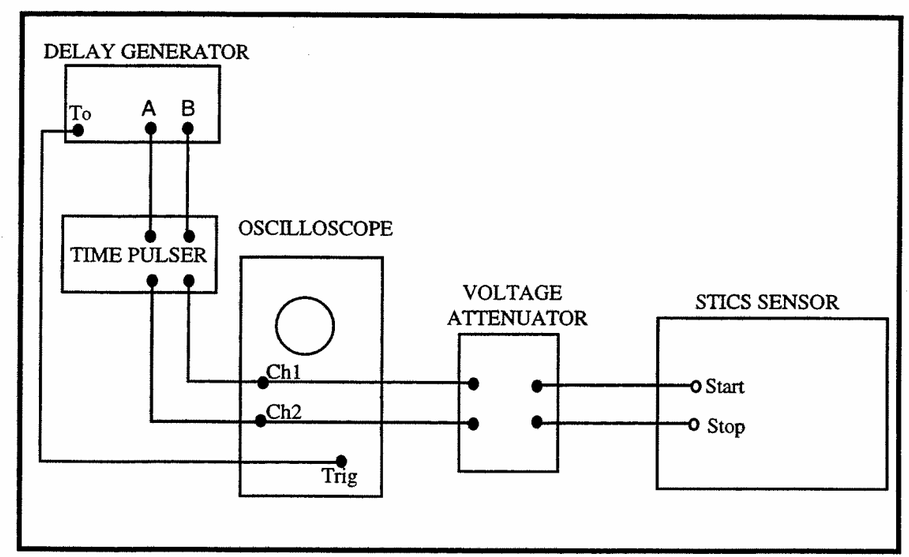

Figure A.21. Set-up used for time pulser tests.

Table A.15. Telescope 1 time pulser results done November 1993.

	Time(ns)	Mode Chn #	Mean Chn #	Sigma
FSR1, RSR1	10	73	73.68	0.63
	50	167	167.58	0.57
	100	282	282.48	0.52
	200	522	522.43	0.56
	300	764	764.66	0.65
	340	861	861.42	0.60
	400	1005	1005.53	0.62
FSR2, RSR1	10	73	73.74	0.66
	50	167	167.65	0.61
	100	282	282.49	0.51
	200	522	522.43	0.57
	300	764	764.79	0.69
	340	861	861.45	0.59
	400	1005	1005.57	0.66

Table A.16. Telescope 2 time pulser results done November 1993.

	Time(ns)	Mode Chn #	Mean Chn #	Sigma
FSR3, RSR2	10	74	74.52	0.52
	50	168	168.49	0.51
	100	283	283.43	0.56
	200	523	523.30	0.64
	300	765	765.53	0.61
	340	862	862.27	0.66
	350	886	886.62	0.67
	400	1006	1006.50	0.61
FSR4, RSR2	10	74	74.50	0.51
	50	168	168.48	0.52
	100	283	283.26	0.66
	200	523	523.06	0.70
	300	765	765.46	0.58
	400	1006	1006.45	0.60

Table A.17. Telescope 3 time pulser results done November 1993.

	Time(ns)	Mode Chn #	Mean Chn #	Sigma
FSR5, RSR3	10	74	74.72	0.65
	50	168	168.50	0.51
	100	283	283.48	0.52
	200	523	523.42	0.57
	300	765	765.69	0.66
	340	862	862.43	0.59
	400	1006	1006.49	0.63
FSR6, RSR3	10	73	73.92	0.70
	50	167	167.71	0.65
	100	282	282.49	0.51
	200	52	522.46	0.56
	300	764	764.91	0.71
	340	861	861.46	0.60
	400	1005	1005.57	0.66

The following equation is used by the DPU to convert from channel number, T_{ch}, to time, T:

$$T\ (ns) = (T_{ch} - 44)/2.3725306895 \qquad (A.15)$$

This equation was determined from data taken in July 1992, and should still be valid because no changes were made to the time-of-flight system since then.

A.4 Inflight Cross Calibration

In order to check the accuracy of our instrument response function, we compared our He flux values to those from two other sensors on WIND. The first comparison was done with the SupraThermal Energetic Particle (STEP) instrument which is part of the energetic particle investigation EPACT (von Rosenvinge et al., 1995) on WIND. STICS and STEP overlap in energy at the higher end of the STICS range. Events were chosen during corotating interaction regions (CIRs) when the fluxes are generally omni-directional. For the second comparison, STICS He flux values were compared with those from the MASS sensor, which is part of the SMS experiment. MASS measures ions at solar wind energies (0.5 - 11.6 keV/e) where the incident flux can be treated as a parallel beam. STEP cannot distinguish between different charge states, so its data would include both He^{+1} and He^{+2}, whereas STICS data contain only He^{+2}. However, this should not be a problem because the He^{+1} contribution is very small (as verified with the STICS He^{+} data).

A.4.1. STEP Comparison

The STEP sensor is similar to STICS in that it measures time-of-flight and energy in determining the mass of ions from He to Fe. The entrance aperture is cone-shaped and leads directly to the time-of-flight chamber resulting in a simple geometric factor. This sensor consists of two time-of-flight telescopes with polar acceptance angles +17.5° to +34.5° and -17.5° to -34.5° out of the eclpitic and with an azimuthal acceptance angle of 44° each. The energy range of STEP is from ~80 keV to ~60 MeV (von Rosenvinge et al., 1995).

During each selected time period, WIND was over 200 R_e upstream of the Earth within a passing CIR. The three different time periods are as follows:

Table A.18. Time periods for STEP and STICS comparisons.

Number	Time Period
1	4/07/95 12:00 - 22:00
2	5/02/95 20:00 - 5/03/95 04:00
3	5/30/95 12:00 - 24:00

Figure A.22 show the STICS and STEP He omni-directional spectra for the first time period. At the lower energies, the spectra from telescope 2 (T 2) diverges from the other two because it also contains solar wind ions. The spectra from all three STICS telescopes converge at the higher energies and match-up to the STEP data within a factor of about 2.

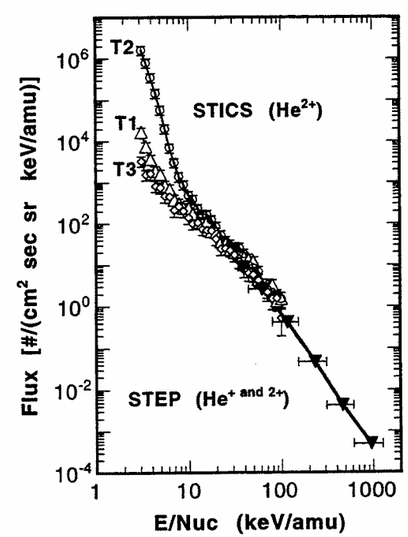

Figure A.22. STICS and STEP Helium spectra from 12:00 - 22:00 April 7, 1995 (time period 1) within a corotating interaction region (CIR).

A.4.2 MASS Comparison

The MASS sensor uses a new application of the time-of-flight technique to determine the mass of solar wind ions with a high degree of accuracy (Hamilton et al., 1990; Gloeckler, 1990). The sensor consists of a spherical segment, electrostatic deflection system followed by a time-of-flight high mass resolution spectrometer. The energy range is from 0.5 to 11.6 keV/e which is covered in 64 steps.

By comparing the STICS He^{+2} spectra to the MASS He data (courtesy Mike Collier), we can check the lower end of the STICS energy range. The spectra from both sensors were calculated assuming that the incident particles were in the form of a parallel beam, and the velocity bins were normalized to the solar wind speed. The following nine time periods were examined during high-speed solar wind streams:

Table A.19. Time periods for STICS and MASS comparisons.

	Time Period	V_{SW} Range (km/s)
1	1/30/95 18:00 - 1/31/95 15:00	650 - 689
2	2/01/95 00:00 - 2/02/95 24:00	615 - 650
3	2/13/95 12:00 - 2/14/95 24:00	615 - 650
4	3/01/95 12:00 - 3/02/95 17:00	615 - 650
5	3/12/95 08:00 - 3/14/95 16:00	650 - 689
6	3/12/95 08:00 - 3/14/95 16:00	689 - 730
7	4/09/95 00:00 - 4/10/95 24:00	615 - 650
8	6/20/95 00:00 - 6/21/95 12:00	650 - 689
9	7/17/95 10:00 - 7/18/95 10:00	615 -650

The STICS and MASS data for each time period (see Figure A.23) matched-up to within a factor of 2.

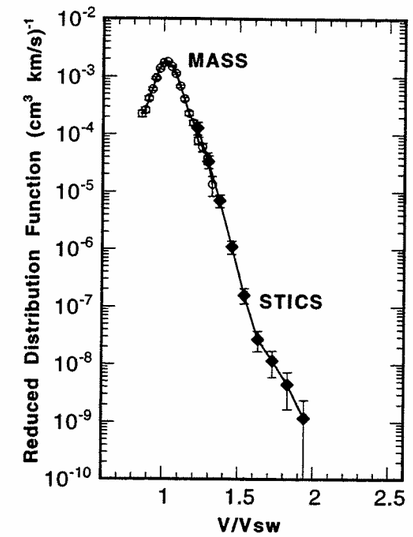

Figure A.23. STICS and MASS helium spectra for 2/1/95 00:00 - 2/2/95 24:00 during a high-speed stream. The data are selected for solar wind speeds between 615-650 km/s.

A.4.3 Correction to Geometric Factor

Looking at Figures A.21-A.22, we can see that the slopes of the overlapping data all match-up well. This suggests that the STICS TOF telescope efficiencies are correct. However, the STICS spectra do not line-up exactly with the STEP nor the MASS spectra suggesting that a further correction must be made to the STICS geometric factor. To calculate this "shift factor (∂)", a Kappa fitting FORTRAN program developed by Mike Collier was used. In this program, one data set is held constant while the other is multiplied by a constant factor to shift it closer to the first data set until the best Kappa fit is obtained. Only the overlapping data were used, and in all cases the STICS data were shifted. Table A.20 shows the different shift factors obtained from the fits.

Table A.20. Factor by which STICS data was multiplied to match-up with STEP and MASS data for the different time periods.

	Time Period	Shift Factor	Average
STEP	1	0.4827	
	3	0.4785	0.48 ± 0.01
MASS	1	0.6412	
	2	0.8505	
	3	1.0660	
	4	0.6229	
	5	0.6161	
	6	0.7387	
	7	0.6034	
	8	0.8594	
	9	0.4756	0.72 ± 0.18

The average STEP shift factor was used to correct the isotropic geometric factor (g_i) for each telescope (eqn A.10), and the average MASS shift factor was applied to the parallel beam geometric factor (G_i) for each telescope (equation A.9). Table A.21 shows the revised geometric factors. The revised total isotropic geometric factor, g, is therefore 0.089 ± 0.010 cm^2 sr.

Table A.21. Revised geometric factors after comparisons with STEP and MASS flight data.

Telescope	Revised Parallel Beam Geometric Factor, G_i, (cm^2)	Revised Isotropic Geometric Factor, g_i, (cm^2 sr)
1	0.72 ± 0.18	0.031 ± 0.002
2	0.68 ± 0.18	0.029 ± 0.002
3	0.74 ± 0.18	0.029 ± 0.002

A.4 Summary of Calibration Results

STICS was calibrated at the NASA Goddard Space Flight Center (GSFC) and at the Physikalisches Institut, Universität Bern, Bern, Switzerland. From this calibration we determined important correction factors required to calculate the flux for different ions. The energy-per-charge passband Δ(E/Q) was found to be 1.9% FWHM, which is about 2.5 times less than the design goal of 5%. TOF Start and Stop efficiencies were obtained for H, He, C, N, O, Ne, Ar, and Kr. Efficiencies for all other elements can be determined by interpolating between these curves.

Table A.22. Summary of calibration results.

	Results
Accumulation Deadtime:	Correction Factor
Sector 0	2.143
Sector 1,...,15	1.068
Entire Spin	1.103
Channel Number Conversion	
Time	Time (ns) = $(T_{chn} - 44)/2.3725306895$
Energy	Energy (keV) = $(E_{chn} + 6)/0.37654587$
Energy-per-chage (E/Q)	$E/Q=6.190722*(1.1225857)^{DVS=0-31}$
Δ(E/Q) [FWHM]	(0.019 ± 0.001)E/Q
Geometrical Factor:	
Isotropic: $g_{1,2,3}$	0.031, 0.029, 0.029 ± 0.002 cm^2 sr
Parallel Beam, G_2	0.68 ± 0.18 cm^2
Time-of-flight Efficiencies:	See Tables A.2-7
Uncertainties: Start, η_1	H, He: ±5%; All Others: ±10%
Stop, η_2	H, He: 15%; All Others: ±20%
Sphere Efficiency	~60%

The STICS He^{2+} spectra were compared at the lower end of its energy range with MASS He spectra and at the higher end with STEP He spectra. From these comparisons we found that the STICS TOF efficiencies were good, and that we needed to increase our geometric factor. The parallel beam geometric factor was divided by 0.72 ± 0.18, and the isotropic geometric factor was divided by 0.48 ± 0.01.

REFERENCES

Acuña, M. H., K. W. Ogilvie, D. N. Baker, S.A. Curtis, D.H. Fairfield, W.H. Mish, The Global Geospace Science Program and its Investigations, *Space Sci. Rev,* 71, 5, 1995.

Anders, E., and N. Grevesse, Abundances of elements: Meteoritic and solar, *Geochim. Cosmochim. Acta, 53,* 197, 1989.

Axford, W.I., The interaction of the solar wind with the interstellar medium, *Solar Wind, NASA Spec. Publ., 308,* 609, 1972.

Axford, W.I., E. Leer, and G. Skadron, The acceleration of cosmic rays by shock waves, *Proc. Int. Conf. Cosmic Rays 15th, 11,* 132, 1977.

Anagnostopoulos, G. C., Dominant acceleration processes of energetic protons at the Earth's bow shock, *Physica Scripta, T52,* 152, 1994.

Bame, S.J., J.R. Asbridge, W.C. Feldman, M.D. Montgomery, Solar Wind Heavy Ion Abundances, *Solar Phys., 43,* 463, 1975.

Bame, S.J., J.R. Asbridge, W.C. Feldman, J.T. Gosling, Evidence for a structure-free state at high solar wind speeds, *J. Geophys. Res., 82,* 1487, 1977.

Barnes, C.W., J.A. Simpson, Evidence for Interplanetary Acceleration of Nucleons in Corotating Interaction Regions, *Astrophys. J. Lett, 210,* L91, 1976.

Beeck, J., G. Mason, D.C. Hamilton, G. Wibberenz, H. Kunow, D. Hovestadt, B. Klecker, A multi-spacecraft study of the injection and transport of solar energetic particles, *Astrophys. J., 322,* 1052, 1987.

Belcher, J.W., L. Davis, Large amplitude Alfvén waves in the interplanetary medium, 2, *J. Geophys. Res., 76,* 3534, 1971.

Bevington, P.R., and D. K. Robinson, Least-Squares Fit to an Arbitrary Function, Data Reduction and Error Analysis for the Physical Sciences, 2nd ed., McGraw Hill, 1992, pp. 141-167.

Blandford, R.D., and J.P. Ostriker, Particle Acceleration by Astrophysical Shocks, *Astrophys. J. Lett., 221,* L29, 1978.

Bryant, D.A., T.L. Cline, U. Desai, F.B. McDonald, Continual acceleration of solar protons in the MeV range, *Phys. Rev. Lett., 14,* 481, 1965.

Burlaga, L.F., Interplanetary Stream Interfaces, *J. Geophys. Res., 79,* 3717, 1974.

Cane, H. V., D. V. Reames, T. T. von Rosenvinge, Solar particle abundances at energies of greater than 1 MeV per nucleon and the role of interplanetary shocks, *Astrophys. J., 373,* 675, 1991.

Chen, G., and T.P. Armstrong, Acceleration of charged particles in oblique MHD shocks, *Proc. Int. Conf. Cosmic Rays 14h, 5,* 1814, 1975.

Chotoo, K., M. R. Collier, A. B. Galvin, D. C. Hamilton, G. Gloeckler, Extended Solar Wind Distribution Functions in High-Speed Streams, *J. Geophys. Res., 103,* 17441, 1998.

Christon, S.P., and J.A. Simpson, Separation of Corotating Nucleon Fluxes from Flare Fluxes by Radial Gradients and Nuclear Composition, *Astrophys.J. Lett., 227,* L49, 1979.

Christon, S.P., On the Origin of the MeV Energy Nucleon Flux Associated with CIRs, *J. Geophys. Res., 86,* 8852, 1981.

Compton, A. H., and I. A. Getting, An apparent effect of galactic rotation on the intensity of cosmic rays, *Phys. Rev., 47,* 818, 1935.

Decker, R. B., The modulation of low-energy proton distributions by propagating inter-planetary shock waves: A numerical simulation, *J. Geophys. Res., 86,* 4537, 1981.

Desai, M.I., R.G. Marsden, T.R. Sanderson, A. Balogh, R.J. Forsyth, J.T. Gosling, Particle acceleration at corotating reverse shocks in the southern hemisphere: Ulysses results, *Geophys. Res. Lett., 24,* 1155, 1997.

Dietrich, W.F., and J.A. Simpson, Elemental abundance differences between nuclei accelerated in CIR shocks and solar flares, *Proc. Int. Conf. Cosmic Ray 19th, 4,* 277, 1985.

Dwyer, J. R., G. M. Mason, and J. E. Mazur, Acceleration of solar flare ^{3}He at the Earth's bow shock, *Geophys. Res. Lett., 24,* 1997.

Dwyer, J.R., G. M. Mason, J. E. Mazur, T. T. von Rosenvinge, R. P. Lepping, Reacceleration of Corotating Interaction Region Associated Protons at 1 AU, *Trans. Am. Geophys. Union, 79,* S294, 1998.

Dwyer, J.R., G.M. Mason, J.E. Mazur, J.R. Jokipii, T. T. von Rosenvinge, R. P. Lepping, Perpendicular Transport of Low-Energy Corotating Interaction Region-Associated Nuclei, *Astrophys. J. Lett., 490,* L115, 1997.

Ellison, D. C., Shock Acceleration of Diffuse Ions at the Earth's Bow Shock: Acceleration Efficiency and A/Z Enhancement, *J. Geophys. Res., 90,* 29, 1985.

Fan, C. Y., G. Gloeckler, J. A. Simpson, Protons and helium nuclei within interplanetary magnetic region which co-rotates with the sun, *Proc. Ninth Intern. Conf. on Cosmic Rays, 1,* 109, 1965.

Feldman, W.C., J.R. Asbridge, S.J. Bame, J.T. Gosling, Plasma and Magnetic Fields from the Sun, in: The Solar Output and Its Variation, ed. O. R. White, Colorado Associated University Press, Boulder, 1977, p. 351.

Feldman, W.C., J.R. Asbridge, S.J. Bame, E.E. Fenimore, J.T. Gosling, The Solar Origins of Solar Wind Interstream Flows: Near-Equatorial Coronal Streamers, *J. Geophys. Res., 86,* 5408, 1981.

Fermi, E., On the Origin of the Cosmic Radiation, *Phys. Rev, 75,* 1169, 1949.

Fisk, L.A., B. Kozlovsky, R. Ramaty, An interpretation of the observed oxygen and nitrogen enhancements in low-energy cosmic rays, *Astrophys. J., 190,* L35, 1974.

Fisk, L.A., The Acceleration of Energetic Particles in the Interplanetary Medium by Transit Time Damping, *J. Geophys. Res., 81,* 1976.

Fisk, L.A., and M. Lee, Shock acceleration of energetic particles in corotating interaction regions in the solar wind, *Astrophys. J., 237,* 620, 1980.

Forman, M. A., The Compton-Getting Effect for Cosmic-Ray Particles and Photons and the Lorentz-Invariance of Distribution Functions, *Planet. Space Sci., 18,* 25, 1970.

Fränz, M., E. Keppler, N. Krupp, M. K. Reuss, The Elemental Composition in Energetic Particle Events at High Heliographic Latitudes, *Space Sci. Rev., 72,* 339, 1995.

Galvin, A.B., SMS STICS Data Definition Document for the WIND Spacecraft, 1991.

Gerlach, B., and W. Wiewesiek, WIND SMS Commands and Data Formats for the SMS Instrument, Revision 3.0, 1994.

Ghielmetti, A.G., H. Balsiger, R. Banninger, P. Eberhardt, J. Geiss, D. T. Young, Calibration System for Satellite and Rocket-borne Ion Mass Spectrometers in the Energy Range from 5 eV/charge to 100 keV/charge, *Rev. Sci. Instr., 54(4),* 425, 1983.

Giacalone, J. and J. R. Jokipii, Perpendicular transport in shock acceleration, *J. Geophys. Res., 101,* 11095, 1996.

Gleeson, L. J., and W. I. Axford, Cosmic rays in the interplanetary medium, *Astrophys. J., 149,* L115, 1967.

Gleeson, L.J., and W.I. Axford, The Compton-Getting Effect, *Astrophys. Space Sci., 2,* 431, 1968.

Gloeckler, G., The Measurements of Non-Relativistic Charged Particles of Extra-Terrestrial Origin, Introduction to Experimental Techniques of High-Energy Astrophysics, NASA, Washington, D.C., 1970, p1.

Gloeckler, G., D. Hovestadt, L.A. Fisk, Observed distribution functions of H, He, C, O, and Fe in corotating energetic particle streams: Implications for interplanetary acceleration and propogation, *Astrophys. J. Lett., 230,* L191, 1979.

Gloeckler, G., J. Geiss, H. Balsiger, L.A. Fisk, A.B. Galvin, F.M. Ipavich, K.W. Ogilvie, R. von Steiger, B. Wilken, Detection of interstellar pickup hydrogen in the solar system, *Science, 261,* 70, 1993.

Gloeckler, G., J. Geiss, E.C. Roelof, L.A. Fisk, F.M. Ipavich, K.W. Ogilvie, L.J. Lanzerotti, R. von Steiger, B. Wilken, Acceleration of interstellar pickup ions in the disturbed solar wind observed on Ulysses, *J. Geophys. Res., 99,* 17637, 1994.

Gloeckler, G., H. Balsiger, A. Bürgi, P. Bochsler, L.A. Fisk, A.B. Galvin, J. Geiss, F. Gliem, D.C. Hamilton, T.E. Holzer, D. Hovestadt, F.M. Ipavich, E. Kirsch, R. A. Lundgren, K.W. Ogilvie, R.B. Sheldon, B.Wilken, The Solar Wind and Suprathermal Ion Composition Investigation on the WIND Spacecraft, *Space Sci. Rev.*, *71*, 79, 1995.

Gosling, J.T., J.R. Asbridge, S.J. Bame, W.C. Feldman, Solar Wind Stream Interfaces, *J. Geophys. Res.*, *83*, 1401, 1978.

Gosling, J.T., S.J. Bame, D.J. McComas, J.L. Phillips, V.J. Pizzo, B.E. Goldstein, M. Neugebauer, Latitudinal Variation of Solar Wind Corotating Stream Interaction Regions: Ulysses, *Geophys. Res. Lett.*, *20*, 2789, 1993.

Gosling, J.T., W.C. Feldman, D.J. McComas, J.L. Phillips, V.J. Pizzo, R.J.Forsyth, Ulysses observations of opposed tilts of solar wind corotating interactions in the northern and southern hemispheres, *Geophys. Res. Lett.*, *22*, 3333, 1995.

Hamilton, D.C., G. Gloeckler, T.P. Armstrong, W.I. Axford, C.O. Bostrom, C.Y. Fan, S.M. Krimigis, L. J. Lanzerotti, Recurrent Energetic Particle Events Associated with Forward/Reverse Shock Pairs Near 4 AU in 1978, *Proc. Int. Conf. Cosmic Rays 16th*, *5*, 363, 1979.

Hamilton, D.C., G. Gloeckler, F.M. Ipavich, R. A. Lundgren, R. B. Sheldon, D. Hovestadt, New high resolution electrostatic ion mass analyzer using time of flight, *Rev. Sci. Instr.*, *61 (10)*, 3104-3106, 1990.

Harten, R., K. Clark, The Design Features of the GGS WIND and POLAR Spacecraft, *Space Sci. Rev.*, 71, 23, 1995.

Hovestadt, D., O. Vollmer, G. Gloeckler, C. Y. Fan, Differential energy spectra of low-energy (<85 MeV per nucleon) heavy cosmic rays during solar quiet times,*Phys. Rev. Lett.*, *31*, 650, 1973.

Hu, Y. Q., Evolution of corotating stream structures in the heliospheric equatorial plane, *J. Geophys. Res.*, *98*, 13210, 1993.

Hundhausen, A. J., and J. T. Gosling, Solar wind structure at large heliocentric distances: An interpretation of Pioneer 10 observations, *J. Geophys. Res.*, *81*, 1436, 1976.

Hundhausen, A.J., The Solar Wind, Introduction To Space Physics, eds. M. G. Kivelson and C.T. Russell, Cambridge University Press, p 117, 1995.

Intriligator, D.S., and Siscoe, G.L., Stream interfaces and energetic ions closer than expected: Analyses of Pioneers 10 and 11 observations, *Geophys. Res. Lett.*, *21*, 1117, 1994.

Intriligator, D.S, G.L. Siscoe, G. Wibberenz, H. Kunow, J.T. Gosling, Stream interfaces and energetic ions II: Ulysses test of Pioneer results, *Geophys. Res. Lett.*, *22*, 1173, 1995.

Intriligator, D. S, and Siscoe, G. L., Cross-field diffusion in corotating interaction regions, *J. Geophys. Res.*, *100*, 21605, 1995.

Ipavich, F.M., The Compton-Getting Effect for Low Energy Particles, *Geophys. Res. Lett.*, *1*, 149, 1974.

Ipavich, F. M., J. T. Gosling, M. Scholer, Correlation Between the He/H Ratios in Upstream Particle Events and in the Solar Wind, *J. Geophys. Res.*, *89*, 1501, 1984.

Jokipii, J. R., Propagation of cosmic rays in the solar wind, *Space Sci. Rev.*, *9*, 27, 1971.

Jokipii, J.R., Particle acceleration at a termination shock, *J. Geophys. Res.*, *91*, 2929, 1986.

Krieger, A.S., A.F. Timothy, E.C. Roelof, A Coronal Hole and Its Identification as the Source of a High Velocity Solar Wind Stream, *Solar Phys.*, *29*, 505, 1973.

Krimigis, S.M., D. Venkatesan, J.C. Barichello, E.T. Sarris, Simultaneous measurements of energetic protons and electrons in the distant magnetosheath, magnetotail, and upstream in the solar wind, *Geophys. Res. Lett.*, *5*, 961, 1978.

Kunow, H., G. Wibberenz, G. Green, R. Müller-Mellin, M. Witte, H. Hempe, R. A. Mewaldt, E. C. Stone, R. E. Vogt, Simultaneous Observations of Cosmic Ray Particles in a Corotating Interplanetary Structure at Different Solar Distances Between 0.3 and 1 AU from Helios 1 and 2 and Imp 7 and 8, *Proc. Int. Conf. Cosmic Rays 15th*, *3*, 227, 1977.

Lanzerotti, L.J., Measures of Energetic Particles from the Sun, in: The Solar Output and Its Variation, ed. O.R. White, Colorado Associated University Press, Boulder, 1977, p. 383.

Lee, M. A., and L. A. Fisk, Shock Acceleration of Energetic Particles in the Heliosphere, *Space Sci. Rev.*, *32*, 205, 1982.

Lee, M., A Simple Model for the Formation of "Reflected," "Intermediate," and "Diffuse" Ion Distributions Upstream of Earth's Bow Shock, *J. Geophys. Res.*, *90*, 39, 1985.

Lepping, R. P., M. H. Acuña, L. F. Burlaga, W. M. Farrell, J. A. Slavin, K. H. Schatten, F. Mariani, N.F. Ness, F.M. Neubauer, Y.C. Whang, J.B. Byrnes, R.S. Kennon, P.V. Panetta, J. Scheifele, and E. M. Worley, The WIND Magnetic Field Investigation, *Space Sci. Rev.*, *71*, 207, 1995.

Maclennan, C. G., and L. J. Lanzerotti, Elemental Abundances in Corotating Interaction Regions at High Latitudes, *Space Sci. Rev.*, *72*, 297, 1995.

Marsch, E., K.-H. Mühlhäuser, H. Rosenbauer, R. Schwenn, F.M. Neubauer, Solar Wind Helium Ions: Observations of the Helios Solar Probes Between 0.3 and 1 AU, *J. Geophys. Res.*, *87*, 35, 1982a.

Marshall, F., and E.C. Stone, Characteristics of sunward flowing protons and alpha particle fluxes of moderate intensity, *J. Geophys. Res.*, *83*, 3289, 1978.

Mason, G.M., C.K. Ng, B. Klecker, G. Green, Impulsive acceleration and scatter-free transport of ~1 MeV per nucleon ions in ^{3}He-rich solar particle events, *Astrophys. J., 339,* 529, 1989.

Mason, G. M., Energetic heavy ions observed upstream of the Earth's bow shock by the STEP/EPACT instrument on WIND, *Geophys. Res. Lett., 23,* 1231, 1996.

Mason, G.M., J.E. Mazur, J.R. Dwyer, D.V. Reames, T.T. von Rosenvinge, New Spectral and Abundance Features of Interplanetary Heavy Ions in Corotating Interaction Regions, *Astrophys. J. Lett., 486,* L149, 1997.

Mazur, J. E., G. M. Mason, T. T. von Rosenvinge, Fe-rich solar energetic particle events during solar minimum, *Geophys. Res. Lett., 23,* 1219, 1996.

McDonald, F. B., and U. Desai, Recurrent solar cosmic ray events and solar M regions, *J. Geophys. Res., 76,* 808, 1971.

McDonald, F.B., B.J. Teegarden, J.H. Trainor, W.R. Webber, The anomalous abundance of cosmic-ray nitrogen and oxygen nuclei at low energies, *Astrophys. J. Lett., 187,* L105, 1974.

McDonald, F. B., B. J. Teegarden, J. H. Trainor, T.T. von Rosenvinge, and W.R. Webber, The interplanetary acceleration of energetic nucleons, *Astrophys. J. Lett., 203,* L149, 1976.

McGuire, R.E., T.T. von Rosenvinge, F.B. McDonald, Spectra and Composition 2 - 40 MeV/Nucleon of Ions Z = 2 - 28 in Solar Cosmic Ray Events, *Proc. Int. Conf. Cosmic Rays, 5,* 54, 1977.

Meyer, J.-P., The Baseline Composition of Solar Energetic Particles, *Astrophys. J. Suppl., 57,* 151, 1985a.

Meyer, J.-P., Solar-Stellar Outer Atmospheres and Energetic Particles, and Galactic Cosmic Rays, *Astrophys.J. Suppl., 57,* 173, 1985b.

McGuire, F. E., T. T. von Rosenvinge, F. B. McDonald, The Composition of Corotating Energetic Particle Streams, *Astrophys. J., 224,* L87, 1978.

Möbius, E., D. Hovestadt, B. Kleckler, M. Scholer, G. Gloeckler, F.M. Ipavich, Direct observation of He^+ pickup ions of insterstellar origin in the solar wind, *Nature, 318,* 426, 1985.

Neugebauer, M., Observations of Solar-Wind Helium, *Fundamentals of Cosmic Physics, 7,* 131, 1981.

Nolte, J.T., A.S. Krieger, A.F. Timothy, R.E. Gold, E.C. Roelof, G. Vaiana, A.J. Lazarus, J.D. Sullivan, P.S. McIntosh, Coronal Holes as Sources of Solar Wind, *Solar Phys., 46,* 303, 1976.

Ogilvie, K.W., D.J. Chornay, R.J. Fritzenreiter, F. Hunsaker, J. Keller, J. Lobell, G. Miller, J. D. Scudder, E. C. Sittler Jr., R. B. Torbert, D. Bodet, G. Needell, A. J. Lazarus, J.T. Steinberg, J.H. Tappan, A. Mavretic, and E. Gergin, SWE, A comprehensive plasma instrument for the Wind spacecraft, *Space Sci. Rev., 71,* 55, 1995.

Palmer, I.D., and J.T. Gosling, Shock-associated energetic proton events at large heliocentric distances, *J. Geophys. Res., 83,* 2037, 1978.

Parker, E. N., Cosmic ray modulation by the solar wind, *Phys. Rev., 110,* 1445, 1958.

Pesses, M.E., J.A. Van Allen, and C.K. Goertz, Energetic Protons Associated with Interplanetary Active Regions 1-5 AU from the Sun, *J. Geophys. Res., 83,* 553, 1978.

Pesses, M.E., B.T. Tsurutani, J.A. Van Allen, E.J. Smith, Acceleration of Energetic Protons by Interplanetary Shocks, *J. Geophys. Res., 84,* 7297, 1979.

Pesses, M.E., R.B. Decker, and T.P. Armstrong, The Acceleration of Charged Particles in Interplanetary Shock Waves, *Space Sci. Rev., 32,* 185, 1982.

Pizzo, V.J., The evolution of corotating stream fronts near the ecliptic plane in the inner solar system: 1. Two-dimensional fronts, *J. Geophys. Res., 94,* 8673, 1989.

Pizzo, V.J., The evolution of corotating stream fronts near the ecliptic plane in the inner solar system 2. Three-dimensional tilted-dipole fronts, *J. Geophys. Res., 96,* 5405, 1991.

Pizzo, V.J., Global, quasi-steady dynamics of the distant solar wind. 1. Origin of north-south flows in the outer heliosphere, *J. Geophys. Res., 99,* 4173, 1994.

Reames, D.V., I. G. Richardson, L. M. Barbier, On the differences in elemental abundances on energetic ions from corotating events and from large solar events, *Astrophys. J., 382,* L43, 1991.

Reames, D.V., Coronal element abundances derived from solar enegetic particles, *Adv. Space Res., 14,* 177, 1994.

Reames, D.V., L. M. Barbier, T.T. von Rosenvinge, G.M. Mason, J.E. Mazur, J. R. Dwyer, Energy Spectra of Ions Accelerated in Impulsive and Gradual Solar Events, *Astrphys. J., 483,* 515, 1997a.

Reames, D.V., C.K. Ng, G. M. Mason, J.R. Dwyer, J.E. Mazur, T.T. von Rosenvinge, Late-phase acceleration of energetic ions in corotating interaction regions, *Geophys. Res. Lett., 24,* 2917, 1997b.

Richardson, I. G, and R. D. Zwickl, Low Energy Ions in Corotating Interaction Regions at 1 AU: Observations, *Planet Space Sci., 32,* 1179, 1984.

Richardson, I. G., Anisotropy of > 35 keV Ions in Corotating Particle Events at 1 AU, *Planet. Space Sci., 33,* 147, 1985.

Richardson, I.G., Low energy ions in co-rotating interaction regions at 1 AU: Evidence for statistical ion acceleration, *Planet. Space Sci., 33,* 557, 1985.

Richardson, I.G., L.M. Barbier, D.V. Reames, T.T. von Rosenvinge, Corotating MeV/amu Ion Enhancements at ≤1 AU From 1978 to 1986, *J. Geophys. Res., 98,* 13, 1993.

Sanderson, T.R., R.G. Marsden, K.P. Wenzel, A. Balogh, R.J. Forsyth, B.E. Goldstein, Ulysses high-latitude observations of ions accelerated by corotating interaction regions, *Geophys. Res. Lett., 21,* 1113, 1994.

Sarris, E.T., S.M. Krimigis, and T.P. Armstrong, Observations of magnetoshperic bursts of high-energy protons and electrons at ~35 R_E with IMP 7, *J. Geophys. Res., 81,* 2341, 1976.

Savopulos, M., J.J. Quenby, A.R. Bell, Interplanetary Diffusive Shock Acceleration: Exponential or Power-Law Spectra, *Solar Phys., 157,* 349, 1995.

Scholer, M., D. Hovestadt, B. Klecker, G. Gloeckler, The Composition of Energetic Particles in Corotating Events, *Astrophys. J., 227,* 323, 1979a.

Scholer, M., G. Gloeckler, F.M. Ipavich, D. Hovestadt, B. Klecker, Pitch angle distributions of energetic protons near the Earth's bow shock, *Geophys. Res. Lett., 6,* 707, 1979b.

Scholer, M., G. Morfill, M.A.I. Van Hollebeke, On the Origin of Corotating Energetic Particle Events, *J. Geophys. Res., 85,* 1743, 1980.

Scholer, M., F.M. Ipavich, G. Gloeckler, Beams of Protons and Alpha Particles ≥ 30 keV/Charge From the Earth's Bow Shock, *J. Geophys. Res., 86,* 4374, 1981.

Scholer, M., F. M. Ipavich, G. Gloeckler, D. Hovestadt, Acceleration of Low-Energy Protons and Alpha Particles at Interplanetary Shock Waves, *J. Geophys. Res., 88,* 1977, 1983.

Schwadron, N.A., L.A. Fisk, G.Gloeckler, Statistical acceleration of interstellar pick-up ions in co-rotating interaction regions, *Geophys. Res. Lett., 23,* 2871, 1996.

Simnett, G.M., K. Sayle, E.C. Roelof, S.J. Tappin, Corotating particle enhancements out of the ecliptic plane, *Geophys. Res. Lett., 21,* 1561, 1994.

Simnett, G.M., K. Sayle, E.C. Roelof, Differences between the 0.35 - 1.0 MeV/nucleon H/He ratio in solar and co-rotating events at high heliolatitude, *Geophys. Res. Lett., 22,* 3365, 1995.

Smith, C. W, J. W. Bieber, W. H. Matthaeus, Cosmic-Ray Pitch Angle Scattering in Isotropic Turbulence. II. Sensitive Dependence on the Dissipation Range Spectrum, *Astrophys. J., 363,* 283, 1990.

Smith, E.J, and J.H. Wolfe, Observations of Interaction Regions and Corotating Shocks Between One and Five AU: Pioneers 10 and 11, *Geophys. Res. Lett., 3,* 137, 1976.

Smith, E.J., and J.H. Wolfe, Pioneer 10, 11 Observations of Evolving Solar Wind Streams and Shocks Beyond 1 AU, in Study of Travelling Interplanetary Phenomenon, eds. M.A. Shea, D.F. Smart, and S.W. Wu, 1977, D. Reidel, Hingham, Mass., pp 227-257.

Solar Geophysical Data, U.S. Department of Commerce, NOAA, Space Environment Services Center, Boulder, Colorado, SESC PRF 1022-28, 1995.

Sonnerup, B.U.O., Acceleration of particles reflected at a shock front, *J. Geophys. Res., 74,* 1301, 1969.

Steinacher, M., F. Jost, U. Schwab, A modern and fully automated calibration system for space ion mass spectrometers, *Rev. Sci. Instrum., 66,* 4180, 1995.

Steinberg, J.T., A.J. Lazurus, K.W. Ogilvie, R.P. Lepping, J. Byrnes, Differential Flow Between Solar Wind Protons and Alpha Particles: First WIND observations, *Geophys. Res. Lett., 23,* 1183, 1996.

Terasawa, T., M. Scholer, F.M. Ipavich, Anisotropy Observation of Diffuse Ions (>30 keV/e) Upstream of the Earth's Bow Shock, *J. Geophys. Res., 90,* 249, 1985.

Tsurutani, B.T., E.J. Smith, K.R. Pyle, J.A. Simpson, Energetic Protons Accelerated at Corotating Shocks: Pioneer 10 and 11 Observations From 1 to 6 AU, *J. Geophys. Res., 87,* 7389, 1982.

Van Hollebeke, M.A.I., F.B. McDonald, J.H. Trainor, T.T. von Rosenvinge, The Radial Variation of Corotating Energetic Particle Streams in the Inner and Outer Solar System,*J. Geophys. Res., 83,* 4723, 1978.

Van Hollebeke, M. A. I., F. B. McDonald, J. H. Trainor, T. T. von Rosenvinge, Corotating Energetic Particle and Fast Plasma Streams in the Inner and Outer Solar System - Radial Dependence and Energy Spectra, in Solar Wind Four, ed. H. Rosenbauer, 1979, Max-Planck Institut für Extraterrestrische Physik, Garching, Germany, pp 497 - 502.

Vasyliunas, V.M., and G.L. Siscoe, On the Flux and the Energy Spectrum of Interstellar Ions in the Solar System, *J. Geophys. Res., 81,* 1247, 1976.

Vauclair, S., and J.-P. Meyer, Diffusion in the Chromosphere, and the Composition of the Solar Corona and Energetic Particles, *Proc. 19th Internat. Cosmic Ray Conf. (La Jolla), 4,* 233, 1985.

von Rosenvinge, T.T., and R.E. McGuire, Elemental abundances in corotating events, *Proc. 19th Internat. Cosmic Ray Conf., 9,* 547, 1985.

von Rosenvinge, T.T., L.M. Barbier, J. Karsch, R. Liberman, M.P. Madden, T. Nolan, D.V. Reames, L. Ryan, S. Singh, H. Trexel, G. Winkert, G. M. Mason, D.C. Hamilton, P. Walpole, The Energetic Particles: Acceleration, Composition, And Transport (EPACT) Investigation on the WIND spacecraft,*Sp. Sci. Rev., 71,* 155 - 206, 1995.

von Steiger, R., and J. Geiss, Supply of Fractionated Gases to the Corona, *Astron. Astrophys., 225,* 222, 1989.

von Steiger, R., J. Geiss, and G. Gloeckler, Composition of the Solar Wind, Cosmic Winds and the Heliosphere, eds. J.R. Jokipii, C.P. Sonnet, and M.S. Giampapa, Univ. of Arizona Press, Tuscon, 1997, p. 581.

Whipple, E., H. Lancaster, International Coordination of Solar Terrestrial Science, *Space Sci. Rev.*, 71, 41, 1995.

Zwickl, R.D., and W.R. Webber, Limitations of the COS Approximation as Applied to the Cosmic-Ray Anisotropy, *Nucl. Instrum. Methods, 138,* 191, 1976.

Zwickl, R.D., and W.R. Webber, Solar particle propagation from 1 to 5 AU, *Solar Phys., 54,* 457, 1977.

Zwickl, R.D., and E.C. Roelof, Interplanetary Propagation of < 1-MeV Protons in Non-impulsive Energetic Particle Events, *J. Geophys. Res., 86,* 5449, 1981.